UC Berkeley
UC Berkeley Electronic Theses and Dissertations

Title

The Seasonal Migration of the East Asian Rainband and the Associated Atmospheric Circulation

Permalink

https://escholarship.org/uc/item/32p5525n

Author

Liu, Jiabin

Publication Date

2020

Peer reviewed|Thesis/dissertation

eScholarship.org Powered by the California Digital Library
University of California

The Seasonal Migration of the East Asian Rainband and the Associated Atmospheric Circulation

by

Jiabin Liu

A dissertation submitted in partial satisfaction of the

requirements for the degree of

Doctor of Philosophy

in

Earth and Planetary Science

and the Designated Emphasis

in

Computational and Data Science and Engineering

in the

Graduate Division

of the

University of California, Berkeley

Committee in charge:

Professor Inez Y. Fung, Chair
Professor John C. H. Chiang
Associate Professor William R. Boos

Spring 2020

The Seasonal Migration of the East Asian Rainband and the Associated Atmospheric Circulation

Copyright 2020
by
Jiabin Liu

Abstract

The Seasonal Migration of the East Asian Rainband and the Associated Atmospheric Circulation

by

Jiabin Liu

in Earth and Planetary Science

and the Designated Emphasis in

Computational and Data Science and Engineering

University of California, Berkeley

Professor Inez Y. Fung, Chair

Spring and summer rainfall over East Asia is characterized by unique organized bands of precipitation, stretching from China to Korea and Japan in climatology, on top of the typical local convective systems. This banded precipitation has moderate to high intensity and can persist for several days to a few weeks. It undergoes a northward migration from May to August, starting from south China in Guangdong and Guangxi provinces to the Yangtze River Basin and eventually to north China and the Korean Peninsula. The persistent precipitation during this period is referred to as Meiyu in China, Baiu or Tsuyu in Japan, and Changma in Korea; these names capture the timing and the long-lasting nature of this precipitation. Meiyu and Baiu mean "plum rain", denoting the season when the plum ripens; Changma means "long period of rain". This rainy season is sometimes referred to as the East Asian summer monsoon, denoting the seasonally reversing flow that carries warm moist air from the Pacific and the Indian Ocean into continental East Asia.

Previously studies of banded precipitation in East Asia, or the East Asian rainbands, have focused on the total precipitation within specific regions, and have yielded little to no information on individual events or the exact position, shape, and size of the individual rainbands. In this work, I have developed a novel method to identify individual East Asian rainbands in the 6-hourly precipitation from ERA-interim reanalysis product from 1979-2018, by using criteria on precipitation threshold and longitudinal connectedness. This method employs a combination of image processing techniques, manual labelling, and deep neural networks to identify and catalog the long and narrow bands of precipitation. We find that the northward migration of the East Asian rainbands is continuous, and not step-wise, as suggested by previous studies that relied on rainfall data averaged over pentads or longer periods of time.

With our individually identified rainbands, we examine the atmospheric circulation associated with the rainbands to understand their dynamics and seasonal migration. We find that the mid-tropospheric northerly flow north of the East Asian rainbands to be the most important circulation feature that determines the latitudinal position of the rainbands. The seasonal climatology shows that rainbands are located at the convergence of northerly and southerly flows at the latitude of the greatest meridional gradient in moist static energy. On the days with rainbands identified, however, the northerly is much stronger than the seasonal mean while the southerly remains the same. We hypothesize that the southerly flow continually supplies warm moist air for the front, while the sporadic strong northerly triggers the frontogenesis. We have found no strong direct correlation between the latitude or strength of the zonal wind and jet stream to the latitudes of the identified East Asian rainbands. Our finding does not contradict previous studies that have associated the seasonal migrations of the rainbands with those of the jet stream, as they do happen simultaneously.

Using a simple one-layer barotropic quasi-geostrophic model of potential vorticity to guide our analysis of the ERA-interim data, we show that northerly winds crucial for the formation of the rainbands are part of the orographic Rossby wave excited by the Tibetan Plateau. The location and the speed

of this northerly wind are determined by the mid-tropospheric westerlies upstream(west) of the Tibetan Plateau. In early spring, strong westerlies impinging on the Tibetan Plateau are likely to generate Rossby waves with long wavelengths and strong northerlies in East Asia, thus limiting the northward migration of the rainbands. In late spring and summer, the impinging westerlies weaken, the Rossby wavelengths shorten, and the northerlies over East Asia also weaken, permitting rainband migration northwards. On the interannual scale, the East Asian rainbands could covary with the northerly wind and also with the upstream zonal wind in some years. In other years, the correlation cannot be established, as other factors such as the subtropical high over North Pacific and the southerly moisture supply might play a role.

The westerly wind interacting with the Tibetan Plateau is part of the jet streams over East Asia, and we present a detailed characterization of the jet streams over this region. We have developed a method to identify in the 6-hourly reanalysis data the jet streams both on a 2-D surface and in the 3-D domain and to capture the subtropical jet and the eddy-driven jet. This method uses a threshold of 20 m/s for the wind speed and the connected-component algorithm. It can also distinguish the subtropical jet from the eddy-driven jet. Most importantly, the subtropical jet over Asia has a core at 200 hPa, and stays around 25°N in winter until April, when it starts to move northward smoothly to around 45°N in mid-summer. The eddy-driven jet has its core between 200 and 300 hPa. Its latitudinal position has great variability even within a month; it can be between 45°N and 60°N in winter, and between 50°N and 70°N in summer. Both the East Asian rainbands and subtropical jet migrate northward from spring to summer, but they are not perfectly collocated in latitude. The role of jet streams in the season of the rainbands is more on interacting with the Tibetan Plateau to generate Rossby waves downstream than on directly controlling the frontogenesis.

Contents

Contents i

List of Figures iii

1 Introduction 1
Meiyu 1

2 The East Asian Rainbands: Identification and the Associated Atmospheric Circulation 6
2.1 Introduction 6
2.2 Methods for the Detection of the Rainband 9
2.3 Results of the Detection of the Rainband 13
2.4 Atmospheric Circulation Associated with the East Asian Rainbands 15
2.4.1 The Meridional Flow over East Asia 16
2.4.2 The Jet Stream over East Asia 20
2.5 Conclusion 24

3 Orographic Stationary Rossby Waves: from Model and Reanalysis 55
3.1 Introduction 55
3.2 A Simple One-Layer Barotropic Quasi-Geostrophic Model . . . 56
3.2.1 A Steady-State solution for a 1-D Gaussian Mountain . 58
3.2.2 Gaussian Mountain in 2D: Finite-Difference Method . . 60
3.2.3 Realistic Wind Profile and Topography 61
3.2.4 Conclusion 62

3.3 The Connection Between the Westerly Jet West of the Tibetan Plateau and the Northerly Wind over East China 63
3.3.1 Climatology of the Northerly Wind 64
3.3.2 The Wavelength of the Rossby Waves and the Jet Stream 67
3.3.3 Interannual Variations 68
3.3.4 Conclusion 69

4 A Characterization of the Jet Streams in East Asia 88
4.1 Introduction 88
4.2 An introduction to the Jet Streams 89
4.3 Data and Method 92
4.3.1 Data 92
4.3.2 Method to Track the Jet Stream 92
4.3.2.1 The Distribution of the Wind Speeds on 200-hPa Surface 92
4.3.2.2 Tracking the Jet Stream on the 2-D Plane . . 94
4.3.2.3 Tracking the Jet Stream in 3-D 95
4.4 Results 96
4.4.1 The Latitude and the Speed of the Jet Streams at 200 hPa 96
4.4.2 The Jet Streams in 3D 98
4.4.3 The Dynamics of the Subtropical Jet and the Eddy-Driven Jet 100
4.4.4 The Number of Maxima in the Jet Streams 102
4.4.5 The Northerly Component in the Jet Stream 104
4.5 Summary and Discussion 106
4.5.1 Future Work 109

Bibliography 126

List of Figures

2.1 The flow chart of the method to identify individual East Asian rainband. The full dataset of the 6-hourly total precipitation over East Asia from 1979 to 2018 is used. The potential rainband candidates are selected based on the initial thresholds of 10 mm/day. A small subset(approximately 20%) of the potential rainband candidates are manually reviewed to create the 100% accurate rainband results. Then we train a convolutional neural network to identify the rainbands in the remainder of the dataset. 25

2.2 An example of the true positive(a) of a rainband and a false positive(b). The red contour shows the total precipitation of 10 mm/day; the green shows the total precipitation of 15 mm/day. (a) has a true rainband over East China and Western Pacific, while (b) has precipitation patterns that stretch more than 10 ^{o} in longitude, but the precipitation is unorganized and does not form a long and narrow band, so it will not be identified as a rainband. . 26

2.3 The steps to identify connected components from the precipitation data. (a) the raw data of total precipitation; (b) all grid points with total precipitation $>$ 10 mm/day; (c) all connected components detected for (b); (d) all connected components $<$ 50 grid points removed, so only the features big enough are left. . . 27

2.4 The climatology of the latitude and the length of the East Asian rainbands over 1979 to 2018. The dark blue line is the smoothed plot of the central latitude of the rainbands; the scatter plots show the latitude of the rainbands(y-axis) and the length of each rainband(color). May to August is the peak season for long rainbands over East Asia, and the rainbands migrate north from May to August. 28

2.5 The averaged daily total precipitation for the days with rainbands detected for each month from May to August. All 40 years(1979-2018) are considered, and 503 rainbands are detected in May, 1047 rainbands in June, 473 rainbands in July, and 166 rainbands in August. 29
2.6 The averaged daily total precipitation for the days with rainbands detected minus the averaged daily precipitation for each month from May to August. All 40 years(1979-2018) are included, similar to Figure 2.5. The red contour shows 5 mm/day as the difference between the rainband days composite and the monthly average. . 30
2.7 (a) the latitude(y-axis) and the size(color) of the detected rainbands; (b) the latitude(y-axis) and the speed(color) of the maximum northerly wind over East China. The peak rainband season is from May to August; the maximum northerly is weak and further south in June to August, compared to other months. The northward movement of the rainband starts in June when the maximum northerly starts to move south. 31
2.8 The wind at 500 hPa from May to August. The left column has the composite for the days with the rainband detected; the right column has the monthly averaged wind. A strong northerly component in the wind over East China is seen in all four months. The monthly averaged wind also has a prominent northerly component in May and June, but not in July and August. 32
2.9 The anomaly of the wind at 500 hPa on the days with rainband detected, same as the difference between the left column and the right column in 2.3.5. A northerly wind is prominent in all four months over East China. June has the weakest anomalous flow among the four months because the monthly-averaged wind in June already shows a strong cyclonic signature over East China(northerly) and Japan(southerly). 33

2.10 The meridional wind(arrows) averaged over 110°E and 120°E and the meridional gradient of moist static energy, the signature of a precipitation front. Both quantities are averaged for the entire season from May to August(1979-2018). The meridional wind converges around 30°N where the meridional gradient of moist static energy is also the strongest. 34
2.11 The meridional wind(arrows) averaged over 110°E and 120°E and the meridional gradient of moist static energy, the signature of a precipitation front. Both quantities are averaged for all days with rainband detected and the seasonal average is subtracted. The northerly wind north of 30°N is prominent in this difference between the rainband days and the seasonal average; so is the sharp gradient of the moist static energy. The southerly wind to the south of the front largely disappears, as do other features in the gradient of the moist static energy. 35
2.12 Climatology of meridional wind over 110°E and 120°E(color) and the latitude of the rainband. The latitude of the rainband agrees with the latitude where the meridional wind approaches 0 and changes sign, suggesting the front occurs where there is convergence for the meridional winds. The northerly wind north of the front persists from May to July but is weak or further north in August. 36
2.13 The composite of the meridional wind for all the days when rainbands are detected. The meridional wind is averaged between 110°E and 120°E. (a) shows the meridional wind over the days with rainband events; (b) shows (a) minus the climatological meridional wind. The northerly wind is more prominent in August on rainband days than in the monthly average of August, suggesting that northerly wind is essential for the rainband even in August when northerlies start to weaken. 37
2.14 The column-integrated moisture transport from May to August(1979-2018). The moisture over East Asia comes from the westerly transport from the Bay of Bengal and the Western Pacific. The moisture transport from the Bay of Bengal weakens in August. . 38

2.15 The column-integrated moisture transport from May to August(1979-2018) for the rainband-days anomaly(rainband-days minus the monthly average). The anomalous moisture transport for the East Asian rainbands mostly comes from the Western Pacific. 39
2.16 The climatology(1979-2018) of the meridional moisture gradient for May to August. A strong negative moisture gradient can signify a precipitation front. The strongest front in May occurs around 25°N in May and moves north to 30°N and beyond in August. 40
2.17 The Climatology of the meridional gradient in the moist static energy. A strong negative gradient(red) indicates a precipitation front. The strongest front in May occurs around 25°N in May, stays at the approximately same latitude in June. The strongest front moves north past 30°N in July and August. 41
2.18 The climatology of the meridional gradient of the moist static energy in Meiyu season(June 16th to July 15th) and the mid-summer season(July 16th to August 15th). A sharp front(red) occurs at 28°N for the Meiyu season; another front is at 35°N. In mid-summer, the sharp front at 28°N disappears, but the front at 35°N persists. The overall structure of the front shifts north from Meiyu to mid-summer as well. 42
2.19 The rainband-day composite of the meridional gradient of the moist static energy. A sharp front(red) occurs at approximately 28°N; two secondary fronts are from 35°N to 42°N. The meridional gradient of the moist static energy for rainband days resembles that in June(in Figure 2.17) and in the Meiyu season(in Figure 2.18). 43
2.20 The climatology of the meridional temperature gradient averaged over 110°E and 120°E for May to August. A strong negative temperature gradient(red) is a signature of a precipitation front. From May to August, a weak signature of a front appears at approximately 28°N; a strong signature appears around 40°N. The weak signature around 28°N suggests that the signature of the precipitation front and the strong gradient of moist static energy are not dominated by the gradient of temperature. 44

2.21 The climatology of the wind at 500 hPa(arrows and color shading) and the East Asian rainband anomaly as in Figure 2.6(red contour with the levels at 2 and 5 mm/day) from May to August. The gray contour shows the 4000 m topography(the Tibetan Plateau). The jet entrance(dark blue shading) is strong in all four months; the East Asian rainband closely follow the jet entrance. 45
2.22 The pressure-latitude cross-section of the vertical velocity ω(color shading) and the zonal wind U(black contour, unit is m/s). The green line at the bottom of each subplot shows the latitudinal range of the East Asian rainband in each month. The longitudinal range is 110°E to 120°E. The ageostrophic flow is the most prominent in May, but not obvious in July and August. 46
2.23 The temperature advection(in red and blue contour) and the detected rainband(in color) for the standard Meiyu season(June 16$^{\text{th}}$ to July 15$^{\text{th}}$). Red contours indicate positive advection of heat. The long strip of the positive heat advection near 30°N and from 110°E to 140°E collocates with the detected rainband well. . . . 47
2.24 The temperature advection(in red and blue contour) and the vertical motion ω(in color) for the standard Meiyu season(June 16$^{\text{th}}$ to July 15$^{\text{th}}$). Red contours indicate positive advection of heat; dark colors indicate strong ascending motion(negative ω). The long strip of the positive heat advection near 30°N and from 110°E to 140°E collocates with the strong ascending motion. 48
2.25 The climatology of the temperature and the wind at 500 hPa. The temperature is the warmest on top of the Tibetan Plateau; the westerly wind carries the heat from the top of the plateau eastward; the strong westerly wind from the eastern edge of the Tibetan Plateau and further east contributes to the heat advection shown in Figure 2.24. 49

2.26 The temperature advection anomaly(rainband days minus seasonal average) in green contour, the detected rainfall anomaly(rainband days minus seasonal average) in red contour, and the zonal wind in blue for the standard Meiyu season(June 16^{th} to July 15^{th}). The latitude of the positive temperature advection is slightly south of the latitude of the detected rainband; the maximum zonal wind is slightly north of the detected rainband. 50
2.27 The vorticity advection term in Equation 2.1(left column) and the temperature advection term(right column) in color. The rainband-day composite total precipitation(top row) and non-rainband-day composite total precipitation(bottom row) in green contour(in 5 mm/day and 10 mm/day). The vorticity advection for rainband days is approximate twice the magnitude of the temperature advection for rainband days; both advection for non-rainband days are weak. The advection in all four panels follows the position of the detected rainband. 51
2.28 The vorticity advection term in Equation 2.1 for rainband days in the four months from May to August(color) and the anomalous precipitation on rainband days(green contour; 3 mm/day and 5 mm/day). The vorticity advection closely follows the position of the detected rainband in all four months. 52
2.29 The temperature(heat) advection term in Equation 2.1 for rainband days in the four months from May to August(color) and the anomalous precipitation on rainband days(green contour; 3 mm/day and 5 mm/day). The heat advection also follows the position of the rainband but not as well as the vorticity advection does. The magnitude of the heat advection is also smaller than that of the vorticity advection in all four months. 53
2.30 The difference between the QG forcing terms in Equation 2.1 at 300 hPa and 850 hPa in June(color shading). The green contour shows the anomalous rainband in June(contours are 3 mm/day and 5 mm/day). The vorticity forcing term shows a positive agreement the detected rainband; the heat forcing term does not show an agreement with the rainband. 54

3.1 The latitude of the maximum northerly wind(blue), the detected rainband(orange), and the jet stream upstream(west) of the Tibetan Plateau(green). The maximum northerly wind stays around 42.5°N in winter and moves south in June, while both the rainband and the upstream jet stream moves north. The rainband starts to move north in June, and the upstream jet stream starts to move north in March. Both the latitude of the rainband and the upstream jet peaks in late July. The jet stream travels a broader range of latitude than both the northerly wind and the rainband do. 71
3.2 The 1-D steady-state solution for a Rossby wave excited by a mountain of 4000 m for different impinging zonal wind. The bottom panel shows the 1-D topography with a peak of 4000 m; the middle panel shows the streamfunction for an impinging wind of different speeds ranging from 10 m/s to 100 m/s. The top panel shows the corresponding meridional wind for the different impinging wind. The faster impinging wind generates a Rossby wave with longer wavelength; the impinging wind of 40 m/s generates the fastest meridional velocity associated with the wave. 72
3.3 The 1-D steady-state solution for a Rossby wave excited by mountains of various heights and an impinging wind of 40 m/s. The mountains have peaks from 500 m to 6500 m(lower panel). The excited Rossby waves have the same wavelength but different magnitude: the higher mountains generate faster meridional winds downstream. The meridional wind first appears as a northerly wind(negative) to the right side of the mountain. 73
3.4 The 2-D solution to the one-layer quasi-geostrophic model of potential vorticity. The mountain is circular and has a peak of 6000 m(black contour). The colored contour shows the streamfunction of the excited Rossby wave(1×10^7). The northerly part of the Rossby wave appears immediately to the right of the mountain; the flow south of the mountain is largely zonal. 74

3.5 The 2-D solution to the one-layer quasi-geostrophic model of potential vorticity. The three rows show circular mountains with peaks of 1 km, 4 km, and 6 km. The three columns represent uniform impinging wind of 10 m/s, 40 m/s, and 80 m/s respectively. The colored contour shows the streamfunction of the excited Rossby wave(1×10^7). A slow impinging wind of 10 m/s and a short mountain of 1 km excite minimal wave; the wave grows bigger when a fast zonal wind(40 m/s or 80 m/s) impinges on a tall mountain of 4 km or 6 km. 75
3.6 Streamfuncions for the Rossby waves by zonal winds with different wind profiles impinging on a circular mountain. The mountain has a peak of 4500 m, similar to the Tibetan Plateau. The zonal wind profiles have a maximum of 40 m/s with Gaussian profiles. (a)The peaks of the zonal wind profiles are south of the mountain, and the excited Rossby wave is minimal. (b)The peak zonal wind is aligned with the mountain, the Rossby wave is maximal with a northerly component immediately to the right of the mountain. (c)The peak wind is north of the mountain. The wind profiles mimic the zonal jet stream that moves northward from spring to summer. 76
3.7 Streamfuncions for the Rossby waves by zonal wind with different wind profiles impinging on a circular mountain. The mountain has a peak of 4500 m, similar to the average height of the Tibetan Plateau. The zonal wind profiles have a maximum of 50 m/s and have Gaussian profiles narrower than the ones in Figure 3.6. When the maximum of the wind aligns with the latitude of the mountain, the Rossby wave is maximal(top panel), with a northerly component immediately to the right of the mountain. . 77

3.8 Streamfunctions for the Rossby waves excited by the true zonal wind profiles and the real topography of the Tibetan Plateau from May to August. The left panel of each subplot shows the climatology(1979-2018) of the averaged zonal wind averaged from 60°E to 70° on the 200-hPa surface. The right panel of each subplot shows the topography of the Tibetan Plateau(black contour) and the streamfunction(colored contour). The most prominent Rossby wave happens in May with the impinging zonal wind aligned with the latitude of the Tibetan Plateau. In June, the latitude of the peak zonal wind and the topography still align, but the zonal wind is weak and has a less sharp peak than in May. In July and August, the peak of the zonal wind is north of the plateau, and the excited Rossby wave is minimal. 78

3.9 Fig. 13.2 from Vallis, 2017. Solutions of the Charney-Eliassen model. The solid lines are the steady solution using the Earth's topography at 45°N with two values of friction(R1 $\approx$ 6 days, R2 $\approx$ 3 days) and two values of resonant zonal wavenumber(2.5 for k1, 3.5 for k2), corresponding to zonal winds of approximately 17 and 13 ms^{-1}. The solutions are given in terms of height, η', where $\eta' = f_0\psi'/g$, with the scale on the left of each panel. The dashed line in each panel is the observed average height field at 500 mb at 45°N in January. The dotted line is the topography used in the calculations, with the scale on the right of each panel. 79

3.10 The climatology of the speed of the maximum northerly wind over East China at 500 hPa. East China is defined as 110°E to 120°E and 20°N to 50°N. The maximum northerly in this domain is sampled every 6 hours from 1979 to 2018. The northerly wind is the strongest in winter, reaching -22 m/s(negative indicates the northerly direction). The wind speed slowly decreases in spring and starts to drastically decrease in May, until it reaches its minimum around -10 m/s in August. In the fall, the northerly wind strengthens again. 80

3.11 The climatology of the latitude and the speed of the maximum northerly wind over East China at 500 hPa. East China is defined as 110°E to 120°E and 20°N to 50°N. The maximum northerly in this domain is sampled every 6 hours from 1979 to 2018. The northerly wind is the strongest and north at 45°N in winter. The wind speed slowly decreases and moves south in spring. The northerly starts to drastically move south and weaken in May until it reaches its minimum around -10 m/s at 36 ° in August. In the fall, the northerly wind strengthens and moves north again. 81

3.12 The climatology of the longitude and the speed of the maximum northerly wind over East China at 500 hPa. East China is defined as 110°E to 120°E and 20°N to 50°N. The maximum northerly shows a seasonal cycle of a small amplitude of 2° in longitude. The northerly wind is more to the east in winter at 116° than in the summer at 114°. 82

3.13 The climatology of the meridional wind(V) averaged over 36°N to 46°N. The three black dashed lines mark the first, the second, and the third northerly, respectively from left to right. The white dashed lines mark the western and eastern boundaries of the Tibetan Plateau at 75°E and 105°E, respectively. The solid white line marks the longitude of the east coast of China at 120E. Over East China, the northerly wind dominates from winter to spring and only becomes weak in the summer. Downstream(east) of the Tibetan Plateau, the meridional wind switches sign(from red to blue and the opposite) after a longer distance in the winter than it does in the summer. The secondary and the third northerly winds do not appear in winter. 83

3.14 The scatter plot of the upstream zonal wind at 500 hPa averaged between 60°E to 75°E and 36°N to 46°N and the downstream wavelength calculated by the switching of the meridional wind directions. Each dot represents a 6-hour snapshot of the data in the period of 1979 to 2018. The red dots are in summer(June, July, and August); the green dots are in spring(March, April, and May); the orange dots are in fall(September, October, and November); the blue dots are in winter(December, January, and February). In general, longer upstream zonal wind corresponds to a longer wavelength downstream. The U and wavelength are the strongest in winter and the weakest in summer. 84
3.15 The climatology of the upstream zonal wind(U) and downstream meridional wind(V) of the Tibetan Plateau. The left two panels describe the zonal wind at 500 hPa averaged between 60°E to 75°E. The first panel is the maximum speed of this zonal wind; the second panel is the latitude where this maximum speed occurs. The right two panels describe the meridional wind downstream of the Tibetan Plateau averaged between 36°N to 46°N. The third panel is the downstream wavelength to the east of the Tibetan Plateau; the fourth panel is the meridional wind. The upstream zonal wind and the downstream meridional wind go through a similar seasonal cycle. The U is the strongest and at the lowest latitude in winter, and the wavelength is the longest in winter. . . 85
3.16 Comparison of the upstream zonal wind speed averaged over 60°E to 75°E in dashed contour and downstream wavelengths in the colored contour. Both the upstream zonal wind and downstream wavelengths are monthly from 1979 to 2018. Some exceptionally low years in the downstream wavelength correspond to the weak upstream zonal wind, for example in 2001 and 2005. 86
3.17 Comparison of the number of occurrences of the East Asian rainbands in dashed contour and downstream wavelength in the colored contour. Both the rainband and downstream wavelengths are monthly from 1979 to 2018. The high-occurrence year of the rainband usually corresponds to long wavelengths in spring and summer, for example, in 1995, 1998, and 2011. 87

4.1 Climatology(1979-2005) of the distribution of the wind speed in each month on the 200-hPa pressure level. The x-axis shows the wind speed($\sqrt{U^2+V^2}$) and the y-axis shows the number of occurrences in each month. In winter, fast winds above 100 m/s are observed, while in summer the winds are capped below 60 m/s. . 110
4.2 Cumulative Distribution Function of the wind speed over East Asia on the 200-hPa level, climatology for 1979-2018. The wind speed is defined as $\sqrt{U^2+V^2}$. The warmer colors represent warm months, and cold colors are cold months. The wind is the slowest in July and the fastest in January. 111
4.3 The steps to identify the jet stream in the 200-hPa wind field. (a) shows the original wind field(the color is wind speed) on January 1st 00:00, 1979 over Asia. (b) shows the wind field where the wind has a westerly zonal component($U > 0$). The field is largely westerly at this timestamp, but notice some areas over the bottom right corner are removed. (c) shows the wind field where the wind speed($\sqrt{U^2+V^2}$) $\geq$ 20 m/s.(d) shows the filter in (b) and (c) combined, so the remaining wind has both $U > 0$ and $\sqrt{U^2+V^2} \geq$ 20 m/s. 112
4.4 An illustration of the detection of connected components. (a): the wind field that meets the requirement of $U > 0$ and $\sqrt{U^2+V^2} \geq$ 20 m/s. (b): the 4-connectivity in which only the grids that share a side are considered connected. (c): the two detected connected components(in yellow and purple, respectively). 113
4.5 The cross-section of the zonal wind at 75°E(west of the Tibetan Plateau), 95°E(over the Tibetan Plateau), 110°E(East China), and 140°E(Japan). The climatological wind is calculated for January, April, July, and October for 1979-2018. The shading is zonal wind U in m/s, and the contours are 30 m/s(pink) and 10 m/s(red). The grey shading is topography. 114

4.6 Tracking the jet stream by locating the maxima of the wind speed in the latitude-pressure plane. The wind speed(in color) is defined as $(U^2 + V^2)^{1/2}$. The example here shows the cross-section of the wind speed at 95°E(from 0°N to 90°N, and from 1000 hPa to 100 hPa). The local maxima of the wind speed are detected first(red dots) in(a); only the two most prominent maxima(strongest wind speed) are kept for the final result of detection in (b). This way the two strongest signatures of the jet streams are detected and the smaller features and branches are neglected. 115
4.7 The climatology of the latitudinal position of the jet stream (a)west of the Tibetan Plateau, (b) over the Tibetan Plateau, (c) east of the Tibetan Plateau, (d) over east Pacific. 116
4.8 The climatology of the subtropical jet(blue) and the eddy-driven jet(red) at 95°E, 1979-2018. The height of the subtropical jet is stable at around 200 hPa throughout the year, while the eddy-driven jet fluctuates between 100 hPa and 325 hPa. The eddy-driven jet is lower in summer and higher in winter. Both the subtropical jet and the eddy-driven jet migrate north from winter to summer; the subtropical jet moves from 25°N to 45°N, while the eddy-driven jet moves from 45°N to 75°N. Both jets are fast in winter and slower in summer. The subtropical jet is much faster than the eddy-driven jet in winter, but their speeds become similar in spring and summer. 117
4.9 The integrated meridional wind at 500 hPa(purple) and the maximum zonal wind at 850 hPa(green) between 110°E and 120°E. The integrated meridional wind serves as a proxy for the Hadley cell; where it crosses 0 for the first time north of 23°E is the northern edge of the Hadley cell. Maximum U at 850 hPa is a proxy for the eddy-driven jet; its peak shows where the eddy-driven jet is the strongest. 118
4.10 The zonally averaged divergence of eddy momentum flux in January and July. The darkest blue shading is where the most eddy momentum flux is deposited. In January, there are two maxima at 38°N and 50°N. In July, the divergence is weak with a single maximum at 50°N. 119

4.11 The climatology of the number of maxima in jet streams(y-axis) and the corresponding speed of the jet stream(color), 1979-2018. The jet is fast and has a maxima branches of 1.6 in winter. The number of maxima increases in spring and reaches its peak in May before it decreases again. This increase is associated with the subtropical jet moving in the latitudinal range of the Tibetan Plateau in this season; the topography forces the flow to split to move around it. A smaller peak of the number of maxima in jet happens in November. 120
4.12 The climatology of the number of maxima in jet streams(y-axis) in 20-50°N and 90-100°E. The blue shows the number of maxima in the vertical difference of U between 200 hPa and 850 hPa; this serves as a proxy for the baroclinic subtropical jet. The red shows the number of maxima in the vertically averaged U between 200 hPa and 850 hPa; this serves as a proxy for the barotropic eddy-driven jet. In spring, the subtropical jet splits around the Tibetan Plateau to form two branches and has an increase in the number of maxima. The eddy-driven jet remains approximately 1 maximum until it is sometimes too weak or too far north to be detected in summer, therefore the drop in the number of maxima starting in June. 121
4.13 The climatology of the maximum northerly wind at 200 hPa over East China. The northerly wind on 200 hPa is slow in winter and grows strong to reach its peak in May. This peak happens at the same time as the peak in the jet split index; the increase in the northerly wind is most likely due to the interaction between the jet stream and the Tibetan Plateau. A secondary peak happens in September when the jet stream retreats south. 122
4.14 The climatology of the integrated strength of the northerly wind over East China, 1979-2018. The integrated strength is defined as the sum of all northerly wind over the region of East China. The integrated strength is strong from January to April. Starting from mid-May, it takes a plunge to reach its minimum in July and August before it rises again in fall. 123

4.15 The climatology of the latitudinal position(first panel) and the longitudinal position(second panel) and the speed(color) of the northerlies over Eastern China(1979-2018). The strongest northerly wind has a seasonal cycle in both the latitudinal and the longitudinal position: it is at its northmost and eastmost in April and southmost and westmost in August. The east-west movement(about 10 degrees) is smaller than that of the north-south movement(about 15 degrees). 124
4.16 The climatology of the northerly wind on the 500-hPa surface: the latitude(y-axis) and the wind speed -V(color) of the maximum northerly. The maximum northerly wind is at 45°N and strong in winter until May, when it starts to move south and weakens. In August, the northerly is the weakest at 12 m/s and 35°N before it strengthens and moves north again. 125

Acknowledgments

I am most grateful for the support of my advisor, Professor Inez Fung, throughout my Ph.D. career. She has selflessly devoted her time and energy to mentoring me on my academic research and personal growth. She is the most genuine scientist that I look up to. Her wisdom, curiosity, and compassion amaze me and inspire me every day. I remember at the BASC symposium 2019, also in honor of her birthday, Inez did not mention any of her great achievements in the past but gave a talk about her very new and ongoing work. On the brochure of the symposium, her introduction, instead of her countless titles, was "Inez Fung is a student of the Earth, who manages to outfox her at every turn". She has inspired me to always learn from others, to not be afraid to ask questions, and to believe in the new work that I do when others do not. She has also supported me to explore my career options, to always follow my heart, and to be my best self. I will be forever grateful.

I also thank Professor John Chiang for his mentorship during my years at Berkeley. John is the key enabler; his expertise in climate dynamics and in East Asian Summer Monsoon, in particular, is what makes my thesis work possible. I cannot remember how many times I went up to his office on the fifth floor with confusion and frustration about my ongoing research and came back with all the answers I needed and reassurances. John's kindness and patience have almost had a civilizing influence on me. Conversations with John not only always re-ignite passions in me to do better science but spark so much joy.

I thank Professor Bill Boos for the valuable discussion on my research and the thoughtful comments on my work. I am very grateful that Bill only moved to Berkeley in the middle of my Ph.D. career but agreed to serve on my dissertation committee and helped me a lot. His expertise in Asian monsoons and atmospheric dynamics in general is very enlightening to me. I thank Professor Bill Collins for chairing my qualification exam committee and Professor David Shuster for also serving on that committee. I thank Professor Roland Bürgmann for being an extraordinarily kind and supportive graduate advisor of the EPS Department.

I thank the other members of my research group: Stephanie Wuerth, Eren Bilir, Jesse Day, Michail Vrettas, Xiaojuan Liu, and Alex Turner for being

wonderful colleagues, officemates, and friends. Special thanks to David Elvins for always supporting me as a group member with all kinds of things. I also thank the group members of Professor John Chiang and Professor Bill Boos: Wenwen Kong, Michael Herman, Sol Kim, Michael Diaz, and Marysa Laguë for their friendship, support, and scientific discussion. Fellow EPS graduate students Hannah Bourne, Chelsea Willett, Elizabeth Niespolo, Jesse Hahm, Kathryn Materna, Ben Fildier, Jake Seeley, Jake Edman, and Robert Martin-Short have been great friends and colleagues, and I am very proud to have shared a few years of laughter and struggles with all of them.

I am also grateful to the scientists and engineers at the Lawrence Berkeley National Lab. Burlen Loring has taught me the critical idea of the connected components algorithm. Prabhat and Michael Werner introduced me to their work on the analysis of extreme weather events.

My parents have been very supportive of my academic journey and life as a graduate student. I never doubted that I would get a Ph.D. degree since I was a little kid, because my dad had one and has always encouraged me to do it, too. I only realized much later that this was not very common. I thank them for their love, patience, and generosity. Also, I thank all my friends and family; this work would not have been possible without them. I have been extremely lucky to have all of them in my life.

Chapter 1

Introduction

Meiyu

On the road from the southern capital
the fourth month ripens the yellow plums.
The Yangtze goes off surging,
and fine rain comes.
Thatch roofs are soaked,
clouds and fog thick and persistent.
All-day long the dragons delight,
whirlpooling along the bank.

East Asia has been one of the earliest cradles for ancient civilizations and is one of the most densely populated regions in the world, at least partially because of its climate. The region experiences warm wet summers and cold dry winters. Over East China, the Korean peninsula, and Japan, a period of persistent rainfall - called Meiyu, Changma, and Baiu in each country respectively - appears in spring and summer and is crucial for agricultural activities during this period. When this rainfall lasts too long or too short, flood and drought occur; when it does not start or end at the right times, it will not irrigate crops at the right time. This rainfall is unique as it is organized in an elongated band in the west-east direction and migrates northward from spring to summer. Interannual variations of the migration of

this banded precipitation not only concern local farmers but also fascinated generations of climate dynamicists.

The greatest Chinese poet was not the only one who documented this special period of rain. The earliest description of Meiyu in China in literature dates back to the Southern Dynasty(the 6th century), and geographers have reconstructed historical records of Meiyu using local chronicles and meteorological documentation to make interannual comparisons of Meiyu(e.g. Ge et al., 2008). Modern meteorologists study Meiyu using data from weather stations and rain gauges. While banded precipitation occurs around the world(e.g. Houze et al., 1976; Hobbs, 1987; Fairman et al., 2016), the Meiyu-Baiu-Changma rainbands are distinct from frontal precipitation elsewhere because of their persistent and regular nature. China and Japan each announce the dates when the long-lasting rainfall would start and end in each city affected. In 2014 the China Meteorological Administration published a new set of criteria for Meiyu taking into consideration data from more than 100 weather stations(Chen and Li, 2016).

Banded or frontal precipitation results from updrafts associated with low-level convergence of moisture and is distinct from convective precipitation driven by local buoyancy, topography, or typhoons. Using 57 years of daily rain gauge data, Day et al. (2018) identified frontal precipitation and analyzed their attributes. Non-frontal precipitation is estimated as the residual from total precipitation. Their results show that decadal changes in frontal and non-frontal precipitation over East China have different trends and by different causes, with frontal precipitation changes dominating the changes in total precipitation.

Hypotheses about the formation of the rainband and its characteristics can involve the Pacific Ocean, the topography in East Asia, and the large-scale circulation. The intensity of the Meiyu precipitation is shown to be associated with ENSO; El Niño-like conditions preceded enhanced Meiyu rainfall during 1951-1996(Wang and Li, 2004). ENSO is hypothesized to impact precipitation by an anomalous anticyclone in the western North Pacific, which is maintained through positive air-sea feedback. This anticyclone helps draw moisture from the ocean southeast to fuel the precipitation northwest. A similar theory attributes the Meiyu onset to the intensification and northward movement of the western Pacific subtropical high, which helps transport

moisture northwest from ocean to land(Xu et al., 2001). The intensification and movement of the western Pacific subtropical high are in turn related to anomalous convection in the ITCZ and the Bay of Bengal. From spring to early summer, increasingly humid air is transported from the Pacific to land; in June, the moisture from the South Asian monsoon can also be transported to fuel the East Asian rainband(Zhou et al., 2004; Day et al., 2015). The intensity of rainfall in the Meiyu-Baiu-Changma rainbands is also typically tied to variations in sea surface temperatures of the adjacent seas as well as to aerosols and other aspects of climate change(e.g. Lau et al., 2006; Liang and He, 2008; Chen et al., 2013).

The jet stream and the Tibetan Plateau also play critical roles in the formation, movement, and termination of East Asian banded precipitation. The jet stream is at its maximum speed in the jet entrance region over the west Pacific, where the East Asian rainbands are also located. The meridional temperature gradient increases here, so the jet stream accelerates to maintain thermal wind balance. This acceleration is achieved by a transverse circulation, similar to the Hadley cell, maintaining the angular momentum conservation. This transverse circulation has an ascending branch south of the jet stream and can therefore lead to precipitation(Liang and Wang, 1998). The jet entrance region, in turn, results primarily from extratropical heating(e.g. Held et al., 2002; Chang, 2009). The zonally asymmetric extratropical heating can be produced by the jet stream interacting with the Tibetan Plateau and does not need to rely on land-sea contrast(Molnar et al., 2010). The Tibetan Plateau also acts simply as an obstacle for the westerly flow to create convergence downstream. The termination of the East Asian rainband happens when the jet stream moves north of the latitudinal range of the Tibetan Plateau in summer and stops interacting with the topography(Kong and Chiang, 2020). In the energetic perspective, the Tibetan Plateau influences the meridional velocity of stationary eddies which advect enthalpy to contribute to the formation of the front(Chen and Bordoni, 2014). Another theory suggests that the jet stream carries a zonal advection of heat from the top of the Tibetan Plateau; this heat induces an upward motion adiabatically and leads to convection for the Meiyu-Baiu rainband over East Asia(Sampe and Xie, 2010). The heat advection and convection naturally follow the northward movement of the jet stream.

This work focuses on the banded and migrating nature of this organized precipitation, so we will use the term East Asian banded precipitation or East Asian rainbands throughout the work. The term Meiyu(or Baiu, Changma), or East Asian summer monsoon(EASM) as used by some aforementioned studies, often refers to the timing of the local precipitation and does not always capture the larger-scale banded structures and seasonal migration. The term Meiyu primarily refers to the rainfall in the Yangtze River Basin, and the official Meiyu season is only from mid-June to mid-July(e.g. Ding, 1992; Chen, 2004). The banded precipitation, however, can span April to September and move from south China to northeast China during that period of time. The East Asian summer monsoon, on the other hand, is a much broader term that stresses the monsoonal(seasonally-reversing) flow that brings moisture from the ocean to the land; the source of moisture and the strength of the inflow are the focus and not the dynamics of precipitation. In time, location, and the underlying dynamics, these two terms(Meiyu and EASM) do not reflect our focus.

In this work, we focus on the spring and summer seasons when land-sea contrast results in a steady supply of warm moist air from the nearby ocean and seas. We hypothesize that the East Asian banded precipitation form when a strong northerly wind over East China and Japan creates convergence with the warm moist southerly flow. The latitude of this convergence, determined mainly by the northerly winds, is the centroid location of the rainband. We further hypothesize that this northerly wind is in turn determined by the zonal flow west of the Tibetan Plateau, as the northerly is part of a stationary Rossby wave triggered by the zonal flow interacting with the Tibetan Plateau. The strength of this northerly wind and how far south it can penetrate over East China is determined by the strength and latitude of the peak zonal wind upstream. Our work utilizes the wind and precipitation data from 40 years of 6-hourly atmospheric circulation statistics from the ERA-interim reanalysis products(Dee et al., 2011), chosen here because the characteristics of East Asian rainbands are reasonably represented. We also use image processing techniques and deep neural networks to facilitate our identification of the East Asian rainbands, as we emphasize its banded visual shape.

Changes in East Asian precipitation in paleoclimate or under future warm-

ing are beyond the scope of this study. Previous studies have provided interesting perspectives on how changing precipitation over East Asian can be related to changing atmospheric circulation, more often than not to a jet stream changing its latitude(e.g. Chiang et al., 2015a; Ninomiya, 2009; Chiang et al., 2019). We hope that our hypothesis can provide a theoretical basis for the linkage between the banded precipitation and the atmospheric flow, not necessarily only the jet stream. We also note that a change in the banded precipitation could be different from a change in Meiyu or in the East Asian summer monsoon, which can be influenced by the sea surface temperature more(e.g. Cai et al., 2017; Li and Ting, 2017).

The dissertation is organized as follows: Chapter 2 provides a close examination of the East Asian rainbands. We introduce a method using deep neural networks to detect the rainbands and provide a detailed description of them. We also analyze the atmospheric flow associated with these rainbands and scrutinize potential candidates for their formation. Chapter 3 presents a simple one-layer quasi-geostrophic model to simulate a stationary Rossby wave over topography. We use this model to demonstrate that the zonal flow west of the Tibetan Plateau interacts with the plateau to create the crucial northerly flow downstream. We also compare the results from the simple model to realistic wind data for qualitative agreement. Chapter 4 provides an overview of the jet stream. We again introduce novel methods to detect the jet stream using image processing techniques and examine the characteristics of the jet stream in 2-D and 3-D space. We provide a characterization of both the subtropical jet and eddy-driven jet and find that the subtropical jet stream is responsible for the interaction with the Tibetan Plateau, which in turn contributes to the formation of the East Asian rainbands.

Chapter 2

The East Asian Rainbands: Identification and the Associated Atmospheric Circulation

2.1 Introduction

One of the most interesting phenomena in the East Asian climate is the East Asian rainband, sometimes referred to as the Meiyu or Baiu rainfall, or the East Asian Summer Monsoon. The East Asian rainband is a semi-stationary precipitation front occurring in spring and summer and stretches east-west from East China to Korea and Japan. This precipitation front usually appears from May to August and can stay for multiple days on each occurrence. East China receives about 60% of its precipitation via the East Asian Summer Monsoon during this period(Day et al., 2018). This rainband also undergoes a northward transition from spring to summer(Ding and Chan, 2005).

Banded precipitation occurs in many places around the world; these rainbands range from tens to thousands of kilometers in length and can have different dynamic origins. Some are mesoscale structures embedded in extratropical cyclones(Houze et al., 1976); some are snow bands downwind of large water bodies due to the lake-effect(Niziol et al., 1995); some others are orographic precipitation anchored over mountain ranges, such as those found in Japan(Yoshizaki et al., 2000), the Southern German Alps(Hagen, 1992), and east of the Rockies in the United States(Fairman et al., 2016). The orographic

bands are specifically interesting because their quasi-stationary nature leads to the accumulation of large amounts of rainfall in a more predictable pattern than other convective systems. The duration of these rainbands also varies due to different mechanisms of formation and conditions.

Most orographic precipitation has its maximum either at the peak(for small mountains) or on the windward slope(for large mountains), as the most prominent mechanism of the precipitation here is the stable lofting of air parcels up the slope(Roe, 2005); the lee side is usually dry and in the rain "shadow". Precipitation fronts can also form downwind, however, if the mountains are large enough. Two processes contribute to the formation of these fronts: the convergence downstream after the flow goes around the obstacle and the uplifting created by the advection of heat from the top of the mountain(Barrett et al., 2015).

The East Asian rainbands occur in the downwind of the Tibetan Plateau, the highest topographic feature on earth. While the plateau is crucial to the formation of the rainband as previously shown in simulations(Chen and Bordoni, 2014; Kong and Chiang, 2020), the rainbands are variable in terms of their occurrence, intensity, and duration; the atmospheric conditions for the variability are far from completely understood. It is therefore important to study the winds and moisture transport on a daily to sub-daily timescale so that the exact conditions that favor the rainbands can be found.

A unique feature of the East Asian rainband is its northward movement from May to August. This seasonal march is well-documented and believed to be step-wise with three stages. The rainband experiences abrupt transitions from the South China Sea to the Yangtze River Basin, then to North China, the Korean Peninsula, and Japan(Ding and Chan, 2005). This behavior is often seen as a result of the jet stream moving north at the same time. Precipitation should follow the jet entrance region in Western Pacific because the jet here is accelerated by a Hadley-like transverse circulation that leads to ascending motion to the south of the jet(Liang and Wang, 1998). The existence of this jet entrance is in turn attributed to the jet interacting with the Tibetan Plateau to create zonally asymmetric extratropical heating(Chang, 2009;Molnar et al., 2010). The Tibetan Plateau also serves as a physical obstacle and can influence stationary eddies downstream by strengthening both the southerly moist flow and the northerly flow to its north to create

the Meiyu front(Chen and Bordoni, 2014). Another theory also states that the jet brings mid-tropospheric zonal advection of heat from the top of the Tibetan Plateau to East China and creates uplift and hence precipitation there(Sampe and Xie, 2010).

Moisture sources are also important to the formation of the rainband. Climatologically, the southerly low-level winds transport water vapor to the extra-tropics and the mid-latitude. There is almost always water vapor coming from the west Pacific: the subtropical high in the western Pacific guides the warm moist flow in the northwest direction, and its variability contributes to the intensity of the rainband(Xu et al., 2001). During the peak season of the East Asian rainbands, the Bay of Bengal also supplies moisture to East Asia(Zhou et al., 2004). Although some of this moisture deposits in southwest China, the remainder will continue to move eastward to fuel the East Asian rainband. This continued moisture supply is seen as a part of the coupling of the South Asian and East Asian precipitation in July and August(Day et al., 2015). While the orographic lifting anchors the position of the rainbands, the supply of moisture can determine the intensity of the rainband to a large degree.

In this chapter, we focus on a precise characterization of the East Asian rainbands, and analysis of the associated atmospheric circulation. Instead of representing the East Asian rainbands with the daily total precipitation in a certain area, we design novel methods using image processing techniques and deep neural networks to identify individual rainbands in the 6-hourly precipitation data from ERA-interim. We study the 40-year period from 1979 and 2018 and present the climatology as well as interannual variations of the East Asian rainbands. The behavior of northward migration from spring to summer and a slight shift from west to east are captured. Because of the inhomogeneity of data streams assimilated into the reanalysis, we resist estimating or interpreting a trend for the 40 years. With the rainbands precisely identified, we examine the atmospheric circulation accompanying the occurrence of the rainbands and compare it with the climatology; this way we extract important characteristics of the circulation for the formation of the rainbands. The meridional winds at both 500 hPa and 850 hPa, the moisture transport, the meridional gradient of moisture and equivalent potential temperature, and the westerly temperature advection are studied. We draw the

conclusion that the meridional circulation, especially the northerly wind to the north of the East Asian rainbands, is the most crucial factor for the formation and seasonal progression of the rainbands. We will further investigate the dynamic origin of this northerly wind in the chapter to follow.

2.2 Methods for the Detection of the Rainband

The East Asian rainband is a prominent feature of precipitation in spring and summer and is characterized by exceptionally long west-east extent, a northward migration through the season, and its special location downstream of the Tibetan Plateau(Ding and Chan, 2005; Chiang et al., 2015a). Early studies of the rainbands, sometimes referred to as Meiyu or the East Asian Summer Monsoon, have analyzed precipitation records from a handful of large cities or the average precipitation in regions of interest, and have provided the climatological precipitation pattern and its seasonal evolution(e.g. Krishnan and Sugi, 2001; Chen, 2004; Zhu et al., 2008).

In this paper, we take advantage of the 6-hourly gridded data of precipitation and atmospheric circulation from the ERA-Interim Reanalysis 1979-2018(Dee et al., 2011) to understand the dynamics of the East Asian rainbands. The ERA-interim data has a horizontal resolution of 0.75° in both the longitudinal and latitudinal direction, and has 37 pressure levels in the vertical, extending from the surface to 1 hPa. We use the precipitation in ERA-interim so that we can take advantage of the complete atmospheric field(wind, moisture, etc.) and analyze the accompanying atmospheric circulation with the rainband. The quality of precipitation data over East Asia in ERA-interim is comparable to gauge-only daily precipitation data(Asian Precipitation—Highly-Resolved Observational Data Integration Towards Evaluation (APHRODITE)). We find that precipitation fields from other reanalysis products and climate model simulations are less successful in capturing the seasonal migration of the rainband in this region. We apply a novel procedure to identify, on a 6-hourly time scale, the latitudinal and longitudinal extents of the west-east extending rainbands in East Asia. This procedure uses a combination of image processing techniques, manual labeling, and deep neu-

ral networks. We further apply similar procedures to identify the jet stream and other relevant atmospheric circulation features on the same time scale.

The analysis is focused on the domain of the East Asian rainbands, from 20°N to 45°N and 110°E to 145°E, encompassing the Middle and Lower Yangtze Plain to the west and the east coast of Japan to the east, the southern border of mainland China to the south, and the Chinese-Russian border to the north. We have also experimented with other slightly different domains, including the domain of the East Asian Summer Monsoon defined by Wang (2002)(20°N to 45°N and 110°E to 140°E), but the results(not shown) are qualitatively similar and do not change our conclusion.

We start from the 6-hourly total precipitation in ERA-interim from January 1979 to December 2018 and apply the rainband detection methods(that we will discuss below) to all months in the year. In later sections, we focus on May to August, the rainy season in East Asia and when banded precipitation is most likely to occur.

The machine learning procedure involves an initial step to select for potential candidates of rainbands and an intermediate step to manually identify rainbands and eliminate false positives in a randomly selected subset of days with potential candidates. With a manually labeled dataset, we then train a deep neural network model to identify the rainbands in each ERA-interim 6-hourly snapshot in the dataset spanning 40 years from 1979 to 2018. For each snapshot, we record the coordinates that a potential rainband reaches in all four directions; we also document the area of coverage of the precipitation and the total amount of precipitation within each rainband. In the end, the climatology of the rainband is generated for these 40 years. The technical details are as follows.

Our detection method here involves three steps: (1)an initial threshold to define connected patterns of 6-hourly precipitation greater than 10 mm/day and longer than 10 degrees in longitude; (2)a manual examination of every connected pattern in a subset of randomly-selected days each month to identify a distinct feature of a long and narrow banded precipitation band from large patches of disorganized precipitation; and (3)a convolutional neural network model trained on the outcome of the first two steps(see Figure 2.1) and applied to the remainder of the dataset. This way we not only articulate a clear requirement for the rainbands but also eliminate false positives that

meet the threshold requirements. As an example, a rainfall pattern around 28°N and extending eastward from 110°E in Figure 2.2(a)(red contour is 10 mm/day in total precipitation) would be identified as a positive rainband as the result of the three-step identification process. In contrast, a large cluster of unorganized rainfall over the South China Sea(see Figure 2.2(b)) might have been identified as a rainband by the thresholds in the first step, but visual inspection and the deep neural network is able to tell that this pattern is different from the narrow and linear thin and clean rainbands that this work seeks to identify. Below we elaborate on each step of the detection method.

The first step selects candidates for rainbands by finding continuous areas where the 6-hourly total precipitation is greater than 10 mm/day. Among these areas, we choose the one with the longest longitudinal extent. In this way, we convert the precipitation map into a binary representation: grid boxes with rainfall greater than 10 mm/day are labeled as 1(hereafter "1-grids"), and grid boxes with less or no rainfall are labeled as 0(hereafter "0-grids"). The results of detection are qualitatively not sensitive to the exact choice of the threshold.

On the binary image from the previous step, we then label all connected components with 4 connectivity, meaning we find all the areas where the grid shares at least one side with another grid. We assign each connected area with a unique group ID. Two grids that touch only at a vertex are not considered to be connected and therefore do not belong to the same group. The labeling of the connected components in digital images is one of the most fundamental operations in pattern recognition and computer vision; it has become efficient and easy to implement and proves to be useful in tracking objects in many types of analysis(He et al., 2009). The labeling serves as a foundation for automating the recognition of complex patterns in climate and many other fields.

The labeling of connected components is far from perfect for our purpose. Firstly, there is no guarantee that the longest connected area in the longitudinal direction has the structure of an elongated narrow band. It could be wide in the north-south direction as well or has a twisted shape, and would not represent a real rainband. We could limit the north-south extent of this connected area or simply limit its size, but this limiting approach would eliminate some true positives without increasing the accuracy much.

Secondly, the labeling of connected components is not robust to small gaps; a long rainband with a one-pixel gap in the middle may not be recognized as a band, leading to false negatives in rainband recognition. While the approach to find connected components gives an approximate account of the rainbands, further steps are needed to make sure the rainbands are correctly detected, so that the analysis on circulations associated with the rainbands can be meaningful.

Manual labeling of the rainband could have been a solution to the aforementioned problems, but labeling 58,400(4x365x40) maps of precipitation for the 40 years of data is not only labor-intensive but would also be subject to inconsistencies when there is a change in personnel engaged in labeling or when an updated or extended record is available. Convolutional neural networks are powerful tools for image classification and require images of the positive class(rainfall maps with manually identified rainbands) and images of the negative class(rainfall maps without any rainband identified). Here, we train a convolutional neural network to identify rainbands in the remainder of the rainfall maps with a relatively small number of labeled images(approximately 500 for each class).

To make sure that the training data, or the approximately 1000 labeled rainfall maps, are representative, we carry out stratified random sampling of the labeled groups of connected components from the first step above. The manual labeling seeks thin, straight, and long(in the west-east direction) strips of continuous precipitation isolated from other patches of rainfall. The negative class is sampled for all 12 months of each year, and the positive class is sampled mostly in spring and summer when rainbands are prevalent. This way we make sure that the model can recognize a negative class of different patterns; a rainy day without rainbands in the summer, for example, looks different from a rainy day without rainbands in the winter; the former can see a lot of unorganized convective rainfall, while the latter may be light rains from stratiform clouds. The beauty of manual labeling after the first automated connected-component labeling lies in the significant savings in labor: we simply select the positive class as our training dataset.

Our convolutional neural network consists of two hidden layers, with a max-pooling of stride 2 and 16 nodes. The inputs are binary images found in step 1 where pixels with “1” represent total precipitation more than 10

mm/day, and pixels with "0" represent precipitation less than that or no precipitation at all. Each image is manually classified as "positive", namely with at least one rainband, or "negative", namely without a rainband. The images represent the area between 20°N to 45°N and 110°E to 145°E and are of size 40 x 46 in pixels. We choose one of the simplest neural networks possible without any hyperparameter tuning to avoid overfitting. A comprehensive strategy in choosing the parameters for neural networks is beyond the scope of this study, but it is a fairly simple task to recognize a horizontal narrow band in a picture. The model trained with 10 epochs reaches 95% accuracy in both training and testing.

With this model in hand, we then identify rainbands in the rest of the dataset. When the neural network identifies a rainband, we return to the result of connected-component labeling to find the exact location of the longest rainband: its extent in all four directions, the total amount of rainfall in the band, and the location of the centroid of the rainfall. This hierarchical approach to identify the rainband strikes a balance between accurate recognition and easy automation; it can be easily adapted to other datasets or to identify other patterns in climate easily.

2.3 Results of the Detection of the Rainband

With the ERA-interim 6-hourly total precipitation fields from 1979 to 2018, we find, in the domain of 20°N to 40°N, 110°E to 145°E, 503 snapshots with rainbands in May, 1047 in June, 473 in July, and 166 in August. June is the peak season of Meiyu rainbands, and May and July see similar numbers of bands, about half of that for June. In August the Meiyu rainbands weaken. A previous study by Day et al. (2018) found a similar peak of the occurrence of frontal precipitation in the Meiyu season(mid-June to mid-July), but with a higher rate of occurrence(60% for the Meiyu season) because of their choice of the dataset and the criteria for the frontal precipitation. Based on our results from the rainband tracking as shown in Figure 2.4, for the most part of the year, the rainfall pattern over East Asia(20°N to 40°N, 110°E to 145°E) is narrower than 10 degrees longitude. Starting from mid-May, the rainfall feature elongates, showing more than 10 to 12 degrees longitude west to east,

and this elongated rainfall pattern corresponding to what has been well-documented as the East Asian(Meiyu-Baiu) rainband.

In May, the East Asian rainbands are located around 25°N, corresponding to the southern Chinese province Guangxi and Guangdong, and also northern Taiwan; the rainband is already north of the South China Sea. In fact, the South China Sea sees much rainfall throughout early spring to the beginning of fall, but the pattern of the rainfall is sporadic and is not organized into elongated bands. Therefore the intense rainfall over the South China Sea is part of the Asian monsoon, but should not be seen as part of the evolution of the East Asian rainbands. This difference is an indication that this rainfall also comes from a different dynamic origin; we will discuss this later in this section.

The elongated banded rainfall moves northward from 25°N in mid-May to around 32°N in mid-July. Previous literature documents this northward movement as three stationary stages and two abrupt jumps in between(e.g. Ding and Chan, 2005; Wang, 2002). Our results from tracking individual rainbands every 6-hour show instead that the northward movement is steady and smooth, and the rainband does not linger in preferred locations as previously described in climatological views. Historically, the Yangtze River basin is thought to see the most traffic of the Meiyu rainband, partly because the river is seen to provide ample moisture to the precipitation. The Yangtze River basin mostly falls in the latitude range of 29°N to 32°N, and Figure 2.4 shows that the rainband travels this range without any prolonged lingering.

32°N is also about the northernmost reach of the rainband. While the rainband does sometimes penetrate past Beijing(approximately 40° N) and reaches northeast China and Korea, its strength diminishes and its length shrinks. As a result, the rainband no longer stands out as the longest intense rainfall feature over East Asia. Also, this northward penetration happens in mid to late summer, when the South Asian monsoon is at its peak and the South China Sea experiences intense rainstorms, so these southern components precipitation overpowers the dwindling Meiyu. Indeed, in Figure 2.4, the latitude of the rainband moves southward from mid-July to September and stays south around 25°N until the Meiyu season starts again next year.

The relative strength between the East Asian rainband and southern precipitation is further illustrated in Figure 2.5. Here we composite the maps

of precipitation over this broader region of East Asia(110°E to 145°E, 20°N to 45°N) at times when an East Asian rainband is identified over the search domain.

The patterns of the rainbands in each month are more prominent with the subtraction of the monthly mean total precipitation from the monthly precipitation composites at times when rainbands are identified(Figure 2.6). From May to July, the rainbands stand out as the only feature in the entire domain of Asia; in August, the signal of the rainband is weak(less than 5 mm/day), but it still exists further north of the rainband's position to July and completes the progression. The centroid of the rainband shifts slightly north from May around 28°N to 30°N in June, and to 32°N in July.

Along with the well-known northward migration, our algorithm identifies two other behaviors that are less documented by previous studies: the rainband also moves east and shrinks in length. In May, the western tip of the rainband penetrates southwest China to the foothill of the Yunnan-Guizhou Plateau. In June, it retreats to the downstream of the Yangtze River basin in East China. This period is also what society recognizes as Meiyu because this part of China is densely populated. In July, the core of the rainband barely covers China, and southern Japan sees the most influence. In August, the heaviest rainband appears in the Korean Peninsula, with weaker patterns spanning east China, the sea of Japan, north China, and the southern bit of Russia. The shrinking and the eastward movement are as obvious as the northward migration, if not more so.

2.4 Atmospheric Circulation Associated with the East Asian Rainbands

The East Asian rainbands in spring and summer are frontal precipitation with origin in large-scale dynamics instead of local processes. Several aspects of the large-scale circulation should be considered when tracing the mechanism of the formation of the rainband. The convergence of the cold and dry northerly winds and the warm and moist southerly winds contributes to the formation of the fronts. The upper-tropospheric jet stream is also believed to be important for the rainband partly because its northward migration across

the latitudinal range of the Tibetan Plateau is a signature of the circulation in Asia in the spring. Previous studies(Sampe and Xie, 2010) also argue that the mid-tropospheric advection of heat from the top of the Tibetan Plateau creates uplift downstream of the plateau, thus creating the banded precipitation. We will examine these two major influences(the meridional flow and the jet stream) in detail. One advantage of our tracking of the rainbands is that we can look at individual events of rainband formation and examine the accompanying features of circulation; this way we avoid the risk to take a seasonal signature of the flow that happens at the same time to be the cause of the rainband.

2.4.1 The Meridional Flow over East Asia

The peak of the northerly flow happens at the same time as that of the rainband, making the former a plausible influence on the latter. The rainbands are suddenly longer in late May and ready to move north; the northerly winds are weaker and ready to move south at the same time, as seen in Figure 2.4. The period from June to August stands out for both the rainband and the northerly wind. Some previous studies suggest that once the northerly becomes weak enough, the strong convergence is lost, and the Meiyu front can no longer be formed. The timing of the two actions indeed agrees, but we shall look at the identified rainband events and see if this signature of the circulation is present.

The climatological view of the monthly mean fields in Figure 2.8(right column) indeed shows a weakening of the northerly winds over East China. This weakening happens because the westerly jet stream moves north from early spring, and in May it straddles the plateau with a strengthening northern branch. In June, the jet stream almost finishes crossing the Tibetan Plateau, and the jet stream is completely north of the plateau and starts to weaken, as a general tendency of the northern hemisphere jet stream towards summer. In July and August, the monthly-mean winds are almost entirely zonal.

If we composite all the snapshots of wind fields when there is a rainband detected at the same time(Figure 2.8, left column), we have a slightly different picture. While both the monthly mean fields and the rainband-positive composites show signatures of the subtropical jet stream, the winds over East

China always have a northerly component for the rainband-positive composites, but not so much for the monthly mean in June, and not at all for July and August.

The difference is the clearest between the composite and the monthly mean of the winds on the 500-hPa surface(Figure 2.9). In all four months, we have easterly and northerly over northern China and Russia, and westerly and southerly over the sea of Japan. This cyclone-shaped signature of circulation on days with the rainbands is strong in May, July, and August, but slightly weaker in June. In June, this cyclone-shaped flow, especially the northerly wind over East China, is already obvious in the monthly-mean field, so the days with the rainband do not differ from the monthly-mean by much.

The convergence and the front are more easily observed in the cross-section of the meridional circulation. Throughout the season when rainbands are prominent(from May 1st to Aug 31st), a pattern of convergence shows between 110°E and 120°E: northerly winds are dominant northward of 30°N, and southerly winds are dominant southward of 30°N(Figure 2.10). The northerlies are stronger in the mid to upper troposphere, whereas the southerlies concentrate in lower to mid-troposphere. The northerlies are part of the stationary Rossby wave excited by the upstream Tibetan Plateau, so they are strong where the upstream westerly winds are strong, at and above 500 hPa. The southerlies are part of the monsoonal circulation that brings in moisture from the ocean into East China.

While both the northerly and the southerly contribute to the formation of the fronts, the northerly wind is a more important signature of the circulation accompanying the rainbands. After subtracting the seasonal(May to August) average of the meridional winds from the composite of the days with detected rainbands, a strong difference in the northerly winds north of 30°N(Figure 2.11) is prominent, but not so in the southerly winds. This pattern suggests that the northerly is the critical triggering force that leads to the formation of a rainband, while the southerly wind serves as a seasonal background that constantly delivers warm and moist air inland.

The importance of the convergence is further shown as the rainbands progress northward from spring to summer. Figure 2.12 illustrates that the latitude of the rainband(black line) nicely corresponds to the latitude where the meridional winds change sign(color contour). The rainband forms where

the northerly and the southerly winds converge and this agreement works exceptionally well from May to July. In August, the climatological northerly winds are too far north or too small. However, on the days in August when rainbands do occur(see Figure 2.13(a)), the composite of all the days with rainbands), the northerly winds can still be strong and reach approximately 35°N. Figure 2.13(b) shows the difference between the days with rainbands and the climatology of the meridional winds over East China; indeed in July and August, stronger and more southward-reaching northerly winds accompany the rainbands compared to the monthly-mean. The strongest northerly winds happen in May and become weaker in June and July, agreeing with the fact that the upstream jet stream is weakening.

The southerly winds, on the other hand, provide warm and more importantly moist air from the ocean, fueling the intense precipitation of the East Asian rainbands. The climatological column-integrated moisture transport in Figure 2.14 suggests that most water vapor over East Asia comes from two sources: the Bay of Bengal to the west and the Pacific to the east. In May and June, moisture starts in the Bay of Bengal and travels eastward to pass Southeast Asia to arrive in China and Japan. The onset of this transport is an indicator of the beginning of the East Asian summer monsoon. In July, this westerly transport significantly weakens, and the moisture from the Pacific starts to dominate. The subtropical high over the Pacific steers the moisture from the South to the northwest first to reach the coast of China, and then to the northeast towards Japan. This high pressure moves north from May to August, resulting in the moisture penetrating north to between 40°N and beyond. Regardless of this switching of moisture sources, the region where we see rainbands always has ample moisture in these four months.

The moisture concentrates around the region of the rainbands if we composite the moisture transport of all rainband-positive periods and subtract the monthly mean from the composites. Much of the intense moisture transport into the rainbands comes from the Pacific; some northerly transport also shows up, because the stronger northerly wind carries a small amount of water vapor as well. The contribution from the Bay of Bengal is minimal, suggesting the rainband is not fueled by the moisture far west, but rather from the Pacific and potentially some local recycling. It is worth noting that the anomaly in the moisture transport collocates with the rainbands, sug-

gesting that the warm and moist southerly flow is a signature of the periods when rainbands form.

Once it is clear where the moisture supply comes from, a closer look at the meridional e cross-section of the climatological moisture gradient can help locate the front. Because the rainbands typically have a southwest to northeast tilt, we focus on the longitude range from 110°E to 120°E. The meridional gradient is calculated for each of the 13 longitudes within this range every 6 hours and then averaged for the 40 years. The moisture gradient in May takes an interesting shape with one peak near-surface around 20°N and two peaks between 30°N and 35°N; another peak is around 25°N and higher at 800 hPa. All three of these peaks persist into June, with the 20°N peak diminishing and the two peaks north of 30°N growing stronger. These two peaks beyond 30°N move slightly northward and become even stronger in July and reach their maxima in August. The peak at 800 hPa becomes weaker in July and August. The strong moisture gradient near 20°N should be associated with the unorganized precipitation in the South China Sea, while the two northern ones correspond to the East Asian rainbands. It is curious that the peaks of the moisture gradient are north to where the actual rainbands appear within 110°E to 120°E in Figure 2.7.

The meridional gradient of the equivalent potential temperature(θ_e) is a better indicator of the frontal systems than the gradient of moisture alone because θ_e captures both the transport of latent heat and sensible heat. Here we use an approximate equation for the equivalent potential temperature, defined as $\theta_e = \theta + L_v q/c_p$(Holton and Hakim, 2013), where L_v is the latent heat of vaporization and c_p is the specific heat for air. In monthly climatology, both May and June have their sharpest gradient in θ_e between 20°N and 30°N; the local maxima appear around 800 hPa, not at the surface. A small second local maximum appears around 35°N near the surface, and this maximum grows stronger and longer in the meridional direction in July and August but stays around the same position at 35°N. This peak at 35°N agrees with the strongest meridional gradient in moisture shown in Figure 2.16. The double-peak shape in the moisture gradient also shows up here in the θ_e gradient.

The signature of frontal systems, a sharp θ_e gradient, does not show a clear single peak at the same latitude as the rainbands in the monthly-mean fields(Figure 2.17) or in the Meiyu and mid-summer averages(Figure 2.18).

Here the Meiyu season is again defined as the core period of Meiyu rainband in mid-June to mid-July(e.g. Tao, 1987; Ding, 1992; Chen, 2004), and in this period the sharpest gradient in θ_e is around 35°N. Another gradient appears around 28°N but does not manifest itself much near the surface; this gradient stretches tall vertically reaching beyond 300 hPa and does not stand out in the following mid-summer period(Figure 2.18(b)), suggesting that this vertical "wall" of θ_e gradient is a signature of the Meiyu season.

The front at around 28°N is the most obvious in the composite of the θ_e gradient for all the days with rainbands identified. In Figure 2.19, a clear maximum meridional θ_e gradient appears around 28°N to 30°N, where the rainbands are found between 110°E and 120°E. The double peaks near the surface are more to the north, now sitting around 38°N and 40°N.

Apart from the moisture, the temperature is another component in equivalent potential temperature and frontogenesis in general. The sharpest gradient in temperature accompanies the subtropical jet stream high above 400 hPa, at 30°N in May and gradually moving north to 38°N in August as seen in Figure 2.20. This range of latitude collocates with the rainbands identified in these four months shown in Figure 2.4. The strongest temperature gradient near-surface is at 38°N to 40°N, to the north of the strongest gradient in equivalent potential temperature. Another peak in the temperature gradient is around 48°N, presumably associated with the polar jet. The temperature gradient has a different sign compared to the moisture gradient and θ_e gradient around 30°N where the rainbands should be; it is warmer in the north at this location.

2.4.2 The Jet Stream over East Asia

The classic theory of ageostrophic circulation states that a front will be generated at the jet entrance region(see Holton and Hakim, 2013); over Western Pacific where the East Asian rainbands are the most prominent, there is a jet entrance. In this region, the confluent flow intensifies the meridional temperature gradient, so the vertical shear of the zonal wind increases to maintain thermal wind balance. A transverse circulation in the height-latitude plane, similar to the Hadley cell, is then generated to provide acceleration to the upper-level zonal wind. This transverse circulation has an ascending branch

to the south of the jet stream and a descending branch to the north of the jet stream.

Figure 2.21 shows the collocation of the detected East Asian rainband with the jet entrance over East China and the Western Pacific. The jet entrance is the strongest in May and weakens in July and August. The ageostrophic circulation across the jet stream can be more easily seen in the cross-sections in Figure 2.22. In May, there is indeed an ascending motion(red shading) to the south of the jet core, and a descending motion(blue shading) to the north. This pattern is less prominent in June, and even weaker in July and August, even though the East Asian rainband is the most frequent in June and July. While the diagnostic relationship of the ageostrophic flow will hold to some extent here, it might not be enough to explain the peak rainband events in June and July. Also, the fundamental cause for the jet entrance and the intensified meridional temperature gradient to appear here might, in turn, be attributed to the meridional flow discussed in the previous section.

Sampe and Xie (2010) proposed another mechanism linking the jet stream to the Meiyu rainfall: the horizontal heat transport from the Tibetan Plateau induces upward motion in the mid-troposphere. The heat advection is carried by the westerlies from the eastern flank of the Tibetan Plateau into eastern China and further east to the Pacific. The mechanism is based on the collocation of this horizontal heat advection with the strongest upward motion at the 500-hPa level over this region in the core Meiyu season, defined to be from June 16th to July 15th. Indeed we see this signature of the heat advection collocating with the rainbands in June and July, albeit with small values. Figure 2.23 shows a composite of the rainbands(color) in the core Meiyu season with the heat advection(contour). The highest values of the heat advection overlap with the strongest Meiyu rainfall well. The western part of the Tibetan Plateau seems to be where the heat comes from, because of its relatively high altitude. The vertical motion at 500 hPa also roughly agrees with the heat advection in terms of the location of their maxima, as shown in Figure 2.23. It is no surprise as the rainband is a large-scale feature of precipitation and should be associated with uplift.

The temperature at the top of the Tibetan Plateau is the warmest in entire East Asia at 500 hPa, as shown by the temperature map in Figure 2.25. The aforementioned heat advection, however, does not seem to make the air at the

location of rainbands particularly warmer than its surroundings: the entire region in 10°N to 35°N and 110°E to 140°E experiences similar temperatures. The westerly wind itself is stronger over the rainband region, as it enters the jet maximum in the western Pacific. The relatively strong heat advection we see in this region may well be a result of the stronger winds rather than the heat.

Westerly heat advection is a seasonal signature that persists throughout June and July. The composite of the heat advection of the days when rainbands are identified helps to show the contribution of the heat advection to the formation of the rainband. Figure 2.26 shows a color map of the zonal wind at 500 hPa in blue, rainband composites in red contour, and anomalous heat advection at 500 hPa in green contours. The core of the rainband(red) is slightly north of the maximum of the heat advection(green), but their longitudes line up nicely. It is worth noting that the anomalous heat advection maximum is 0.4 K/day, exactly half of the maximum in the mean value 0.8 K/day shown in Figure 2.3.19, meaning the heat advection is significantly stronger on days with rainbands. Heat advection less than 1 K/day is nevertheless small and present regardless of the rainfall; it is more likely to provide a favorable background condition instead of to directly trigger the formation of the rainbands.

It is also curious that this favorable condition of heat appears slightly south of the actual rainbands with about a 5° offset in latitude, but the crucial supply of moisture comes from the south. So for some reason, the southerly warm and moist flow does not rain out as soon as it meets the uplift condition until it penetrates north a little more to reach the latitude of the jet core. The fact that the rainbands appear in between the heat advection and the jet core suggests that the two components might be working together to provide the best conditions for the rainbands to form.

The QG-omega equation can give some insights into the relative contribution from the advection of heat and the advection of absolute vorticity. Three terms contribute to the vertical motion ω, essential to precipitation: the advection of absolute vorticity, the advection of heat, and diabetic heating. The diabetic heating follows the existent precipitation, so the first two terms will help understand how the large-scale circulation contributes to creating an ascending motion. Following Holton and Hakim (2013):

$$(\frac{\sigma}{f_0^2}\nabla^2 + \frac{\partial^2}{\partial p^2})\omega = -\frac{1}{f_0}\frac{\partial}{\partial p}[-\mathbf{u_g}\cdot\nabla_h\zeta] - \frac{R}{pf_0^2}\nabla_h^2[-\mathbf{u_g}\cdot\nabla_h T] - \frac{R}{pf_0^2}\nabla_h^2 Q \quad (2.1)$$

where σ is the static stability, f_0 is the planetary vorticity at the center of the rainband events(33°N), ∇_h^2 is the Laplacian on the horizontal surface, u_g is the geostrophic wind, ζ is the absolute vorticity, R is the gas constant for air, T is the temperature, and Q is diabetic heating. Here we choose 500 hPa as the pressure level that we focus on; the forcing terms at 300 hPa are similar to those at 500 hPa but stronger; they are comparatively weak at 850 hPa. The difference between the high-level and low-level forcing terms will therefore be dominant by the signature at higher levels. Here the first term on the right-hand side represents the contribution from the advection of vorticity; the second term represents the advection of temperature(heat).

For all the days with rainband events that we detect, both the vorticity advection term and the temperature advection term contribute to the ascending motion at 30°N over East China and Japan(Figure 2.27). The vorticity advection is about twice the magnitude of the temperature advection term. On days without rainband events, the two terms are both weak. From May to August, the vorticity advection term stays strong and contributes to the ascending motion(Figure 2.28), and the position of the negative vorticity advection follows the detected rainband(green contour) closely. The advection of temperature(Figure 2.29), on the other hand, is the strongest in May, but weakens in the other three months, although the rainband events happen most frequently in June. The vertical shear of the QG forcing terms in Figure 2.30 confirms that the vorticity term will have a positive contribution to the formation of the rainband, while the heating term does not show contribution along the rainband.

The comparison between the vorticity advection and the temperature advection confirms the contribution of the temperature at 500 hPa is important for the ascending motion for the East Asian Summer Monsoon, as stated by Sampe and Xie (2010). The vorticity advection term contributes slightly more for the days with rainbands that we detect, and its dynamic origin needs to be understood. We will further explore this topic in Chapter 3.

2.5 Conclusion

In this chapter, we introduce a novel method to identify individual East Asian rainbands, present the statistics of these identified rainbands, and analyze the atmospheric circulation associated with these rainbands. By comparing the days with the East Asian rainbands with the seasonal and the monthly average, we show the northerly flow to the north of the East Asian rainbands to be the most crucial component of the atmospheric circulation that determines the location of the rainbands and their seasonal migration. The monsoonal southerly flow brings warm moist air from the ocean and persists throughout the monsoon season(May to August) on days with and without the rainbands. The sharp front of the East Asian rainband is detected when the northerly flow is stronger than climatology. Heat advection from the top of the Tibetan Plateau, on the other hand, does not perfectly match the location of the East Asian rainbands. The identified rainbands are south of the core of the jet stream and north of the maximum advection of heat. The advection of absolute vorticity contributes more to the ascending motion associated with the East Asian rainbands. We further explore the dynamic origin of the northerly wind over East China and the advection of absolute vorticity in Chapter 3.

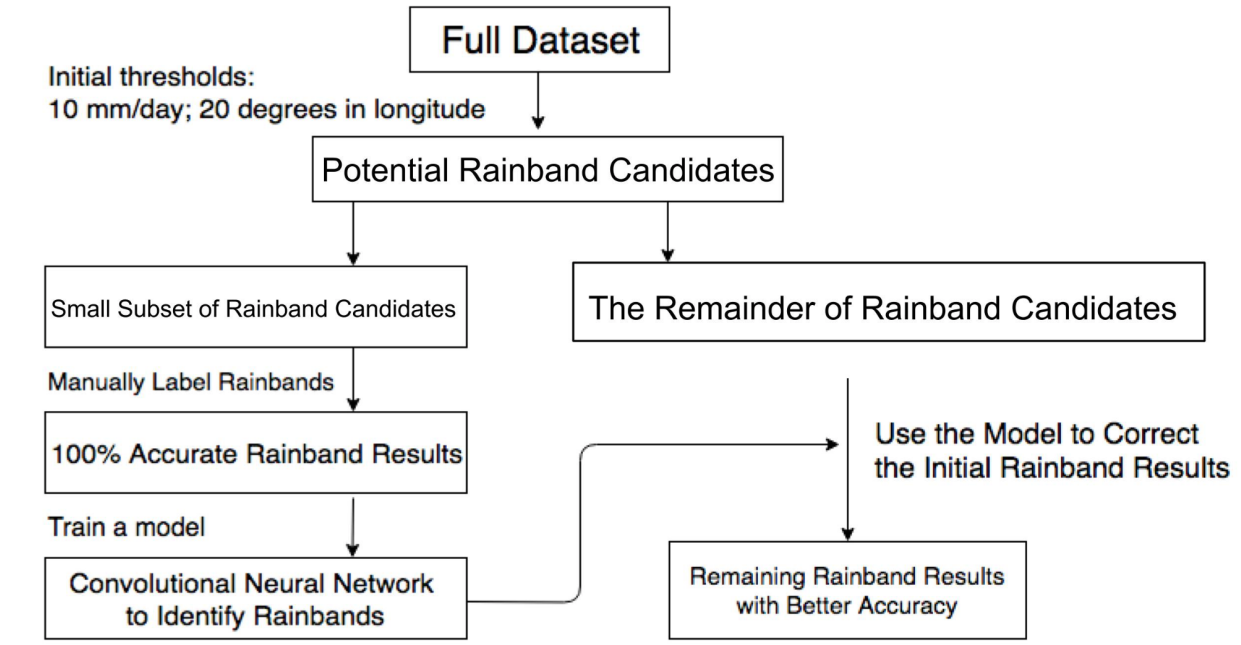


Figure 2.1: The flow chart of the method to identify individual East Asian rainband. The full dataset of the 6-hourly total precipitation over East Asia from 1979 to 2018 is used. The potential rainband candidates are selected based on the initial thresholds of 10 mm/day. A small subset(approximately 20%) of the potential rainband candidates are manually reviewed to create the 100% accurate rainband results. Then we train a convolutional neural network to identify the rainbands in the remainder of the dataset.

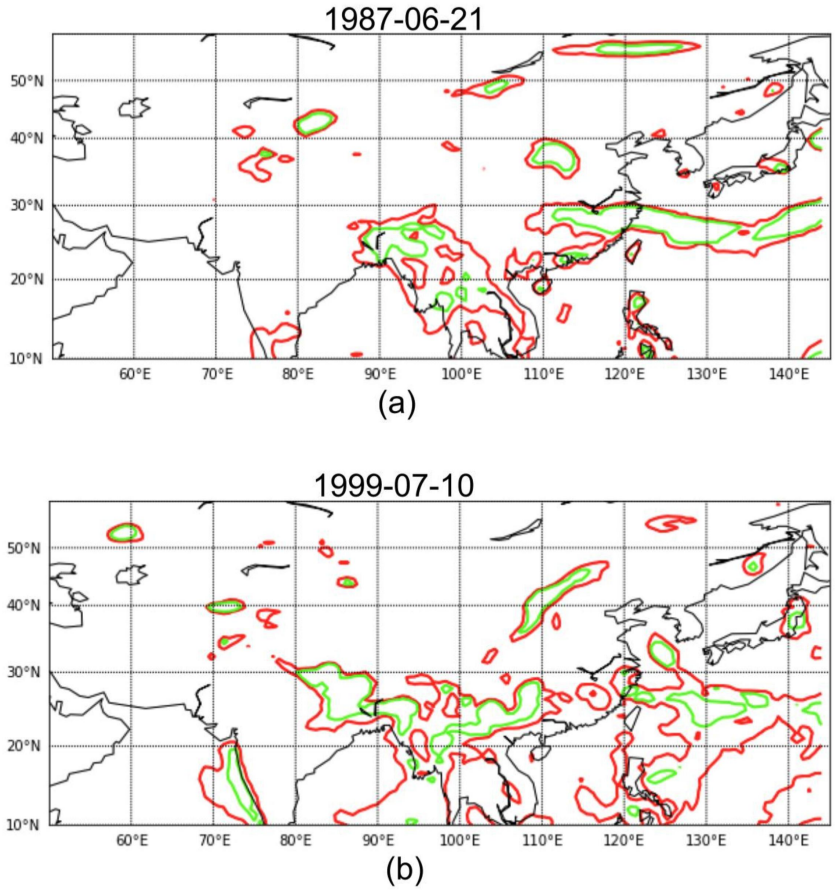


Figure 2.2: An example of the true positive(a) of a rainband and a false positive(b). The red contour shows the total precipitation of 10 mm/day; the green shows the total precipitation of 15 mm/day. (a) has a true rainband over East China and Western Pacific, while (b) has precipitation patterns that stretch more than 10 ^{o} in longitude, but the precipitation is unorganized and does not form a long and narrow band, so it will not be identified as a rainband.

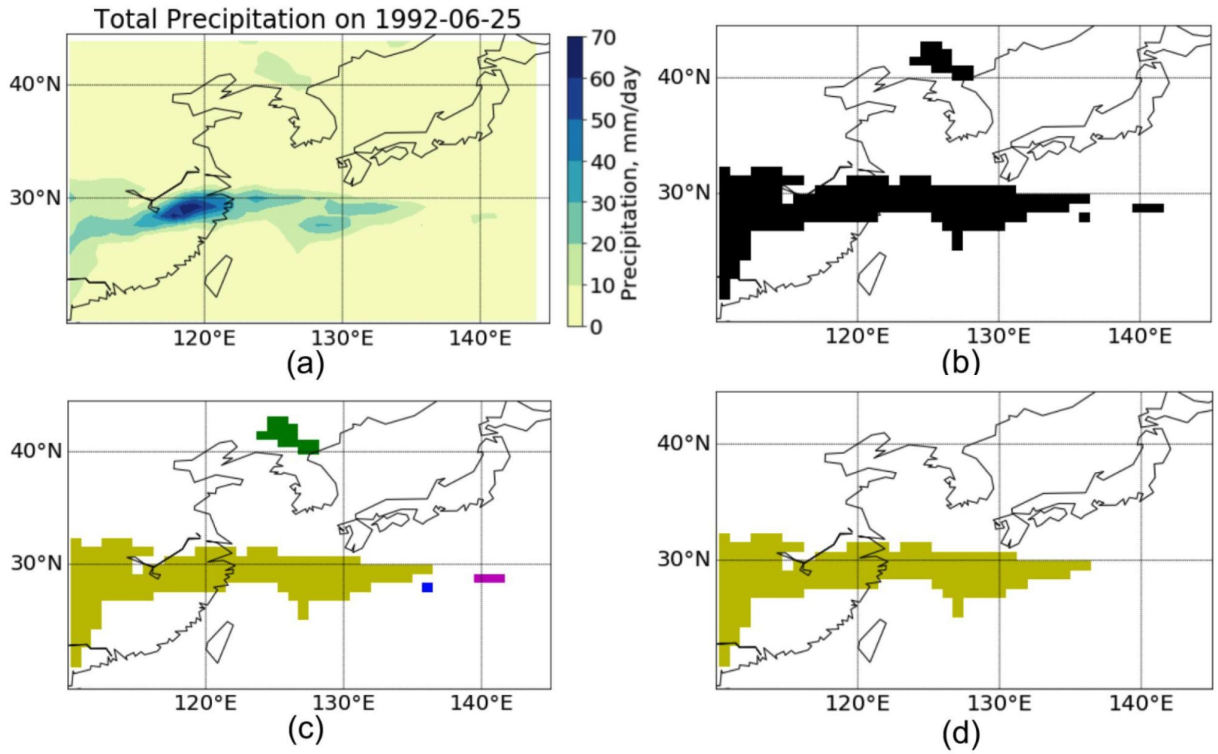


Figure 2.3: The steps to identify connected components from the precipitation data. (a) the raw data of total precipitation; (b) all grid points with total precipitation $>$ 10 mm/day; (c) all connected components detected for (b); (d) all connected components $<$ 50 grid points removed, so only the features big enough are left.

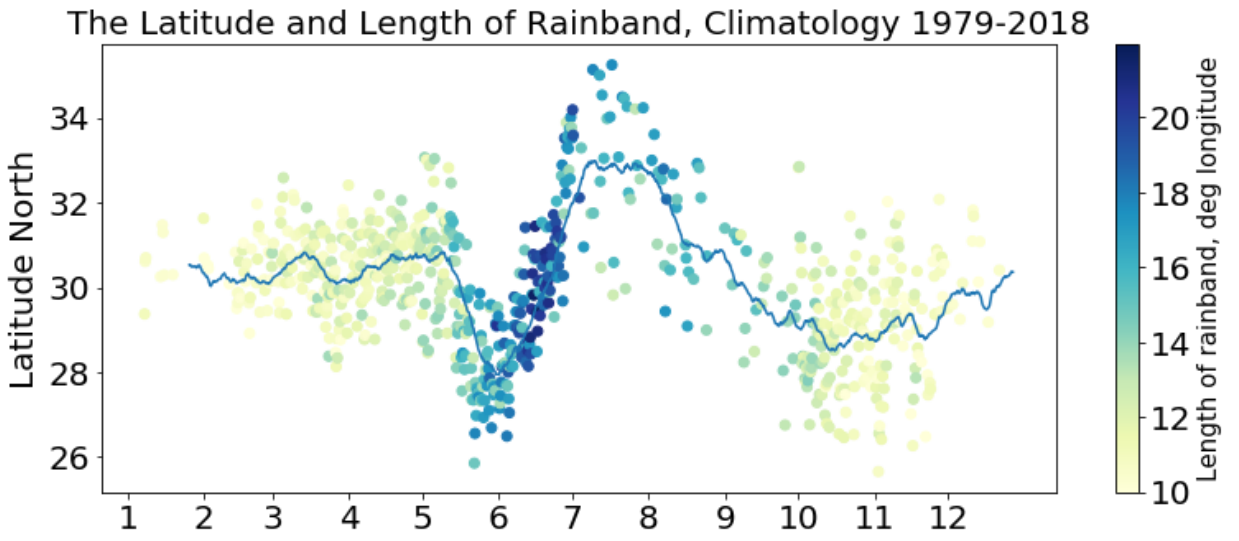


Figure 2.4: The climatology of the latitude and the length of the East Asian rainbands over 1979 to 2018. The dark blue line is the smoothed plot of the central latitude of the rainbands; the scatter plots show the latitude of the rainbands(y-axis) and the length of each rainband(color). May to August is the peak season for long rainbands over East Asia, and the rainbands migrate north from May to August.

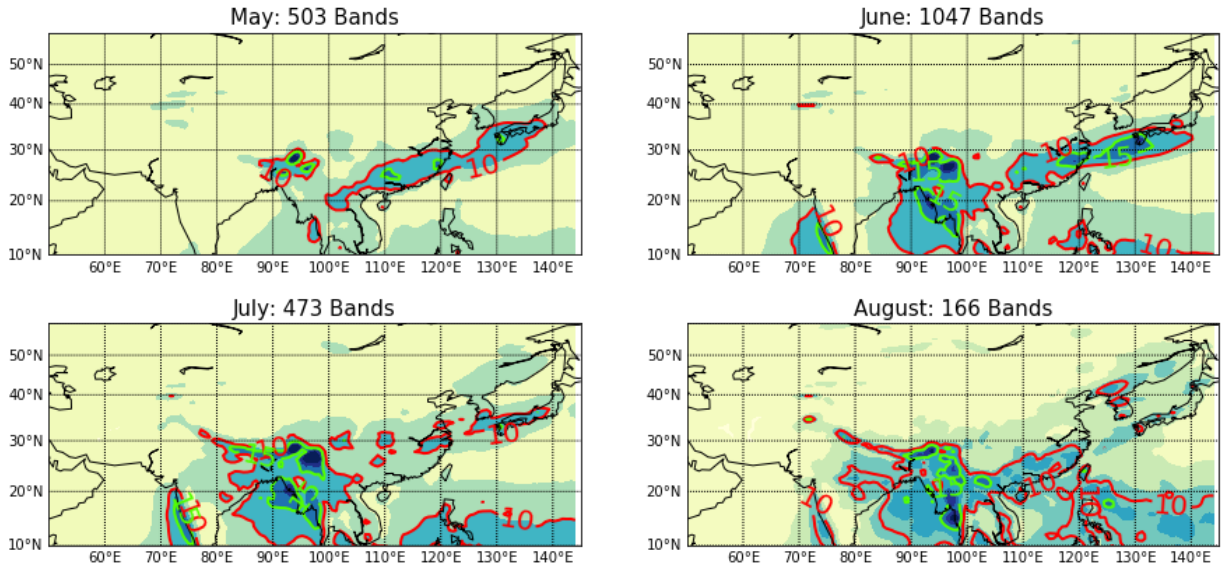


Figure 2.5: The averaged daily total precipitation for the days with rainbands detected for each month from May to August. All 40 years(1979-2018) are considered, and 503 rainbands are detected in May, 1047 rainbands in June, 473 rainbands in July, and 166 rainbands in August.

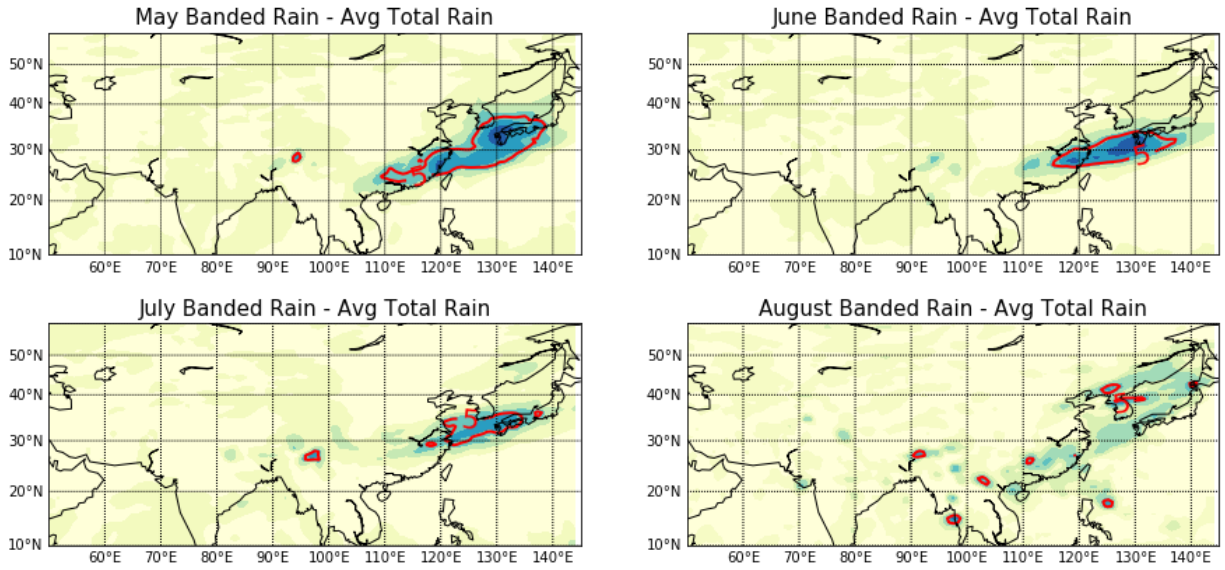


Figure 2.6: The averaged daily total precipitation for the days with rainbands detected minus the averaged daily precipitation for each month from May to August. All 40 years(1979-2018) are included, similar to Figure 2.5. The red contour shows 5 mm/day as the difference between the rainband days composite and the monthly average.

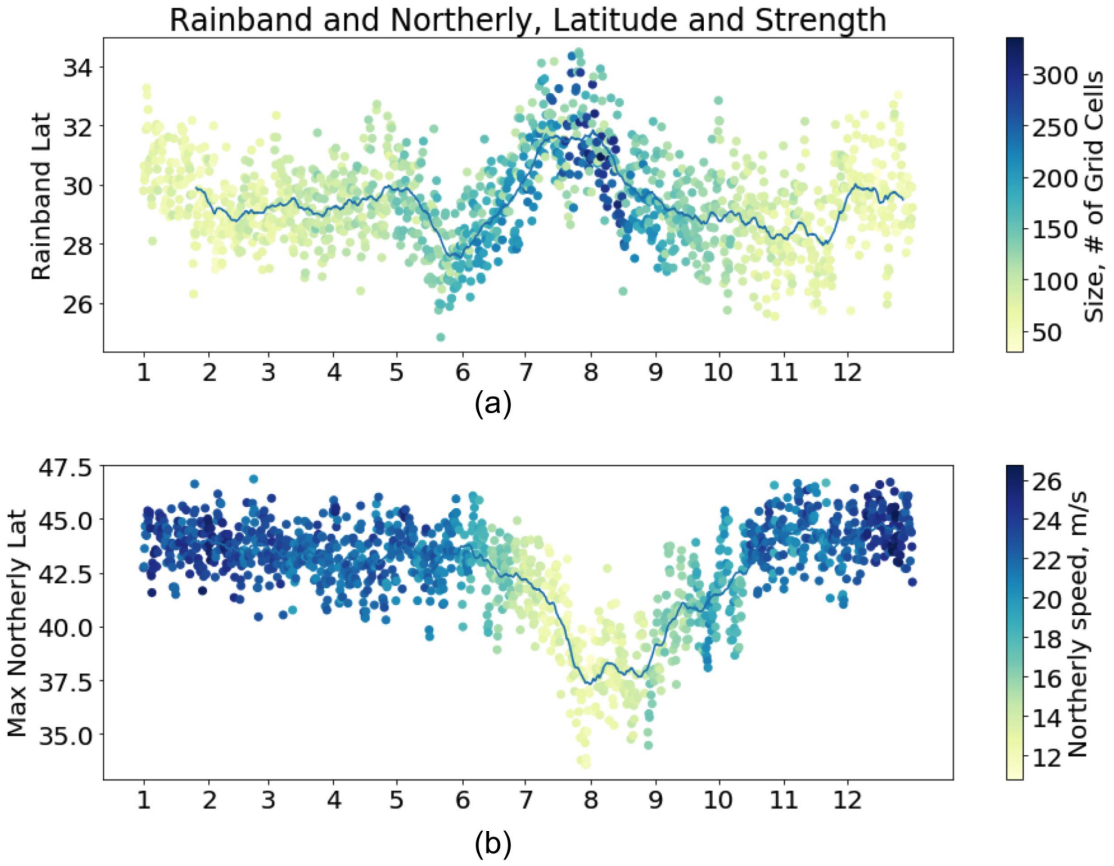


Figure 2.7: (a) the latitude(y-axis) and the size(color) of the detected rainbands; (b) the latitude(y-axis) and the speed(color) of the maximum northerly wind over East China. The peak rainband season is from May to August; the maximum northerly is weak and further south in June to August, compared to other months. The northward movement of the rainband starts in June when the maximum northerly starts to move south.

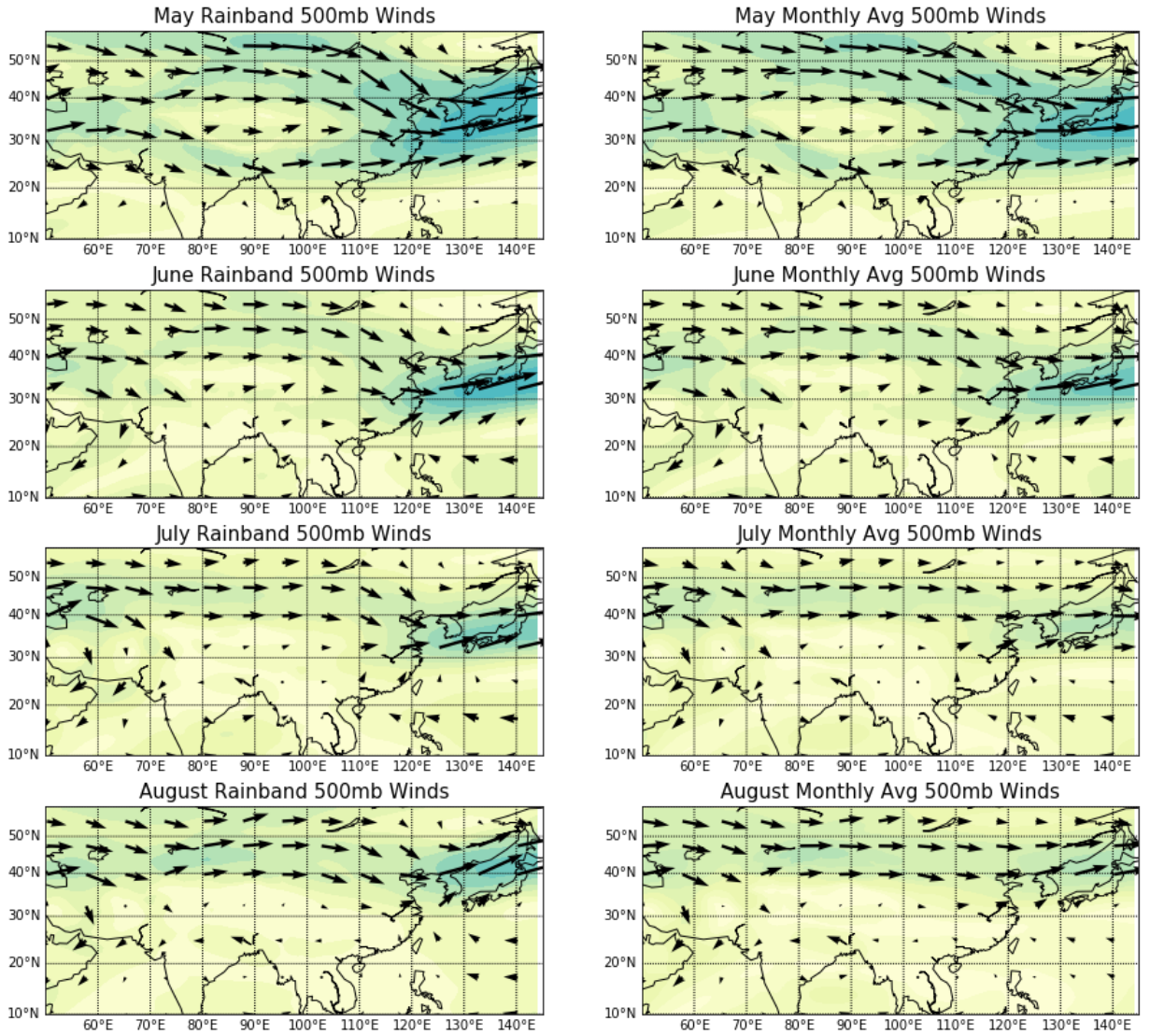


Figure 2.8: The wind at 500 hPa from May to August. The left column has the composite for the days with the rainband detected; the right column has the monthly averaged wind. A strong northerly component in the wind over East China is seen in all four months. The monthly averaged wind also has a prominent northerly component in May and June, but not in July and August.

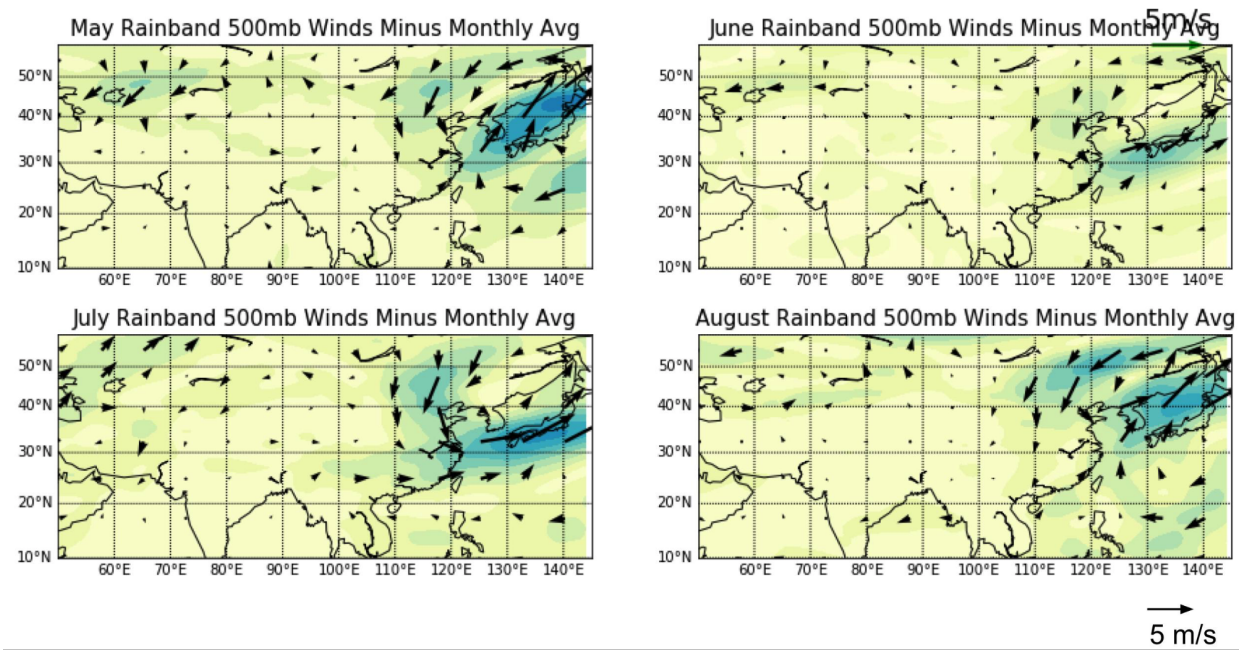


Figure 2.9: The anomaly of the wind at 500 hPa on the days with rainband detected, same as the difference between the left column and the right column in 2.3.5. A northerly wind is prominent in all four months over East China. June has the weakest anomalous flow among the four months because the monthly-averaged wind in June already shows a strong cyclonic signature over East China(northerly) and Japan(southerly).

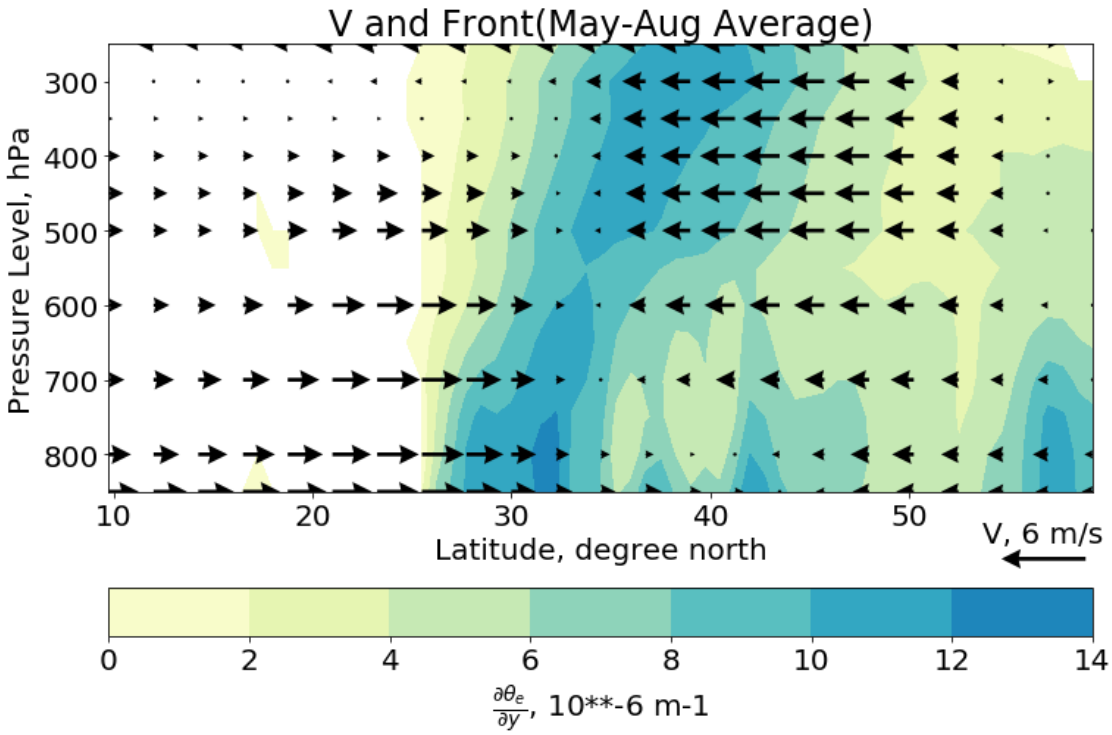


Figure 2.10: The meridional wind(arrows) averaged over 110°E and 120°E and the meridional gradient of moist static energy, the signature of a precipitation front. Both quantities are averaged for the entire season from May to August(1979-2018). The meridional wind converges around 30°N where the meridional gradient of moist static energy is also the strongest.

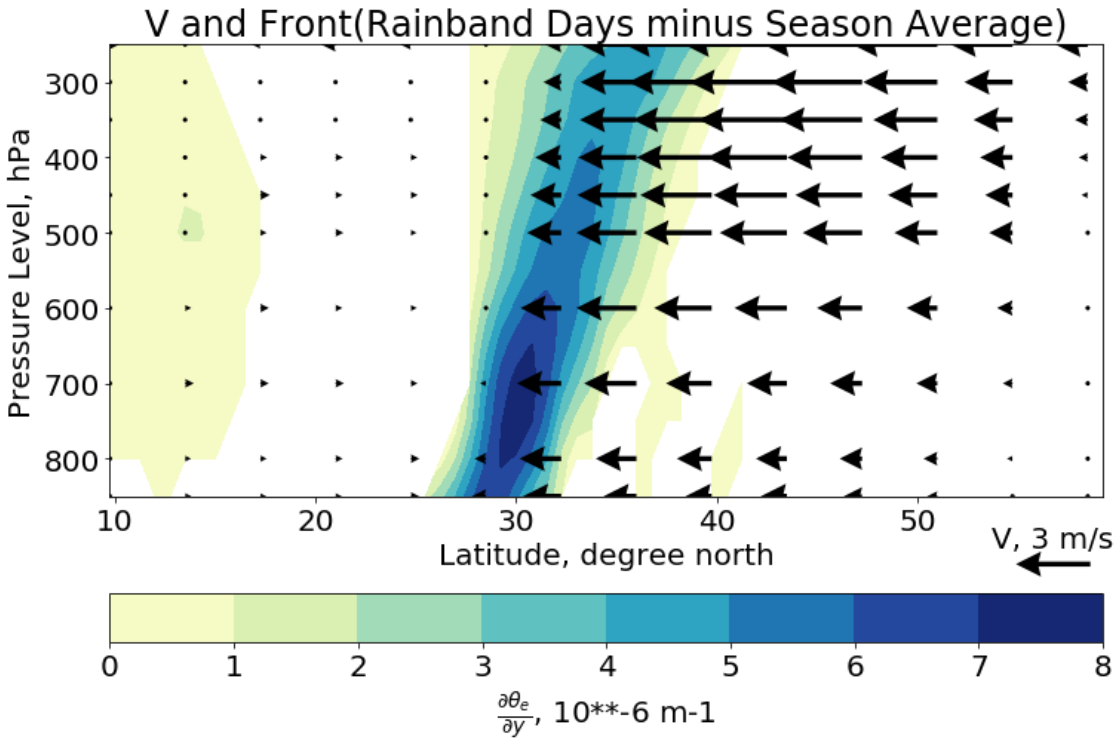


Figure 2.11: The meridional wind(arrows) averaged over 110°E and 120°E and the meridional gradient of moist static energy, the signature of a precipitation front. Both quantities are averaged for all days with rainband detected and the seasonal average is subtracted. The northerly wind north of 30°N is prominent in this difference between the rainband days and the seasonal average; so is the sharp gradient of the moist static energy. The southerly wind to the south of the front largely disappears, as do other features in the gradient of the moist static energy.

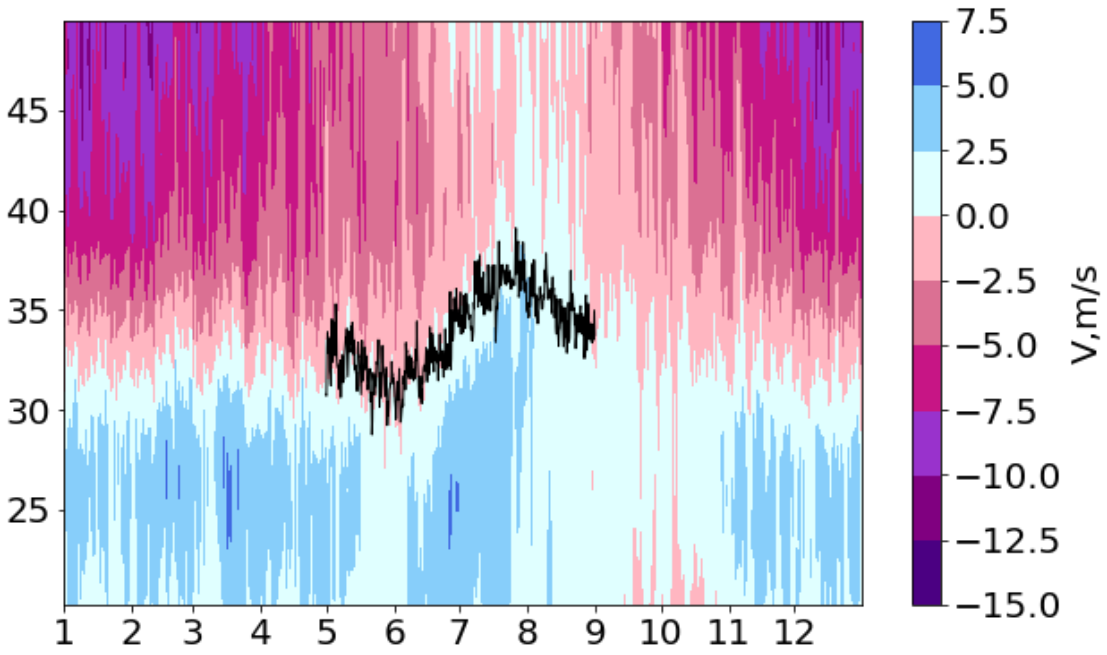


Figure 2.12: Climatology of meridional wind over 110°E and 120°E(color) and the latitude of the rainband. The latitude of the rainband agrees with the latitude where the meridional wind approaches 0 and changes sign, suggesting the front occurs where there is convergence for the meridional winds. The northerly wind north of the front persists from May to July but is weak or further north in August.

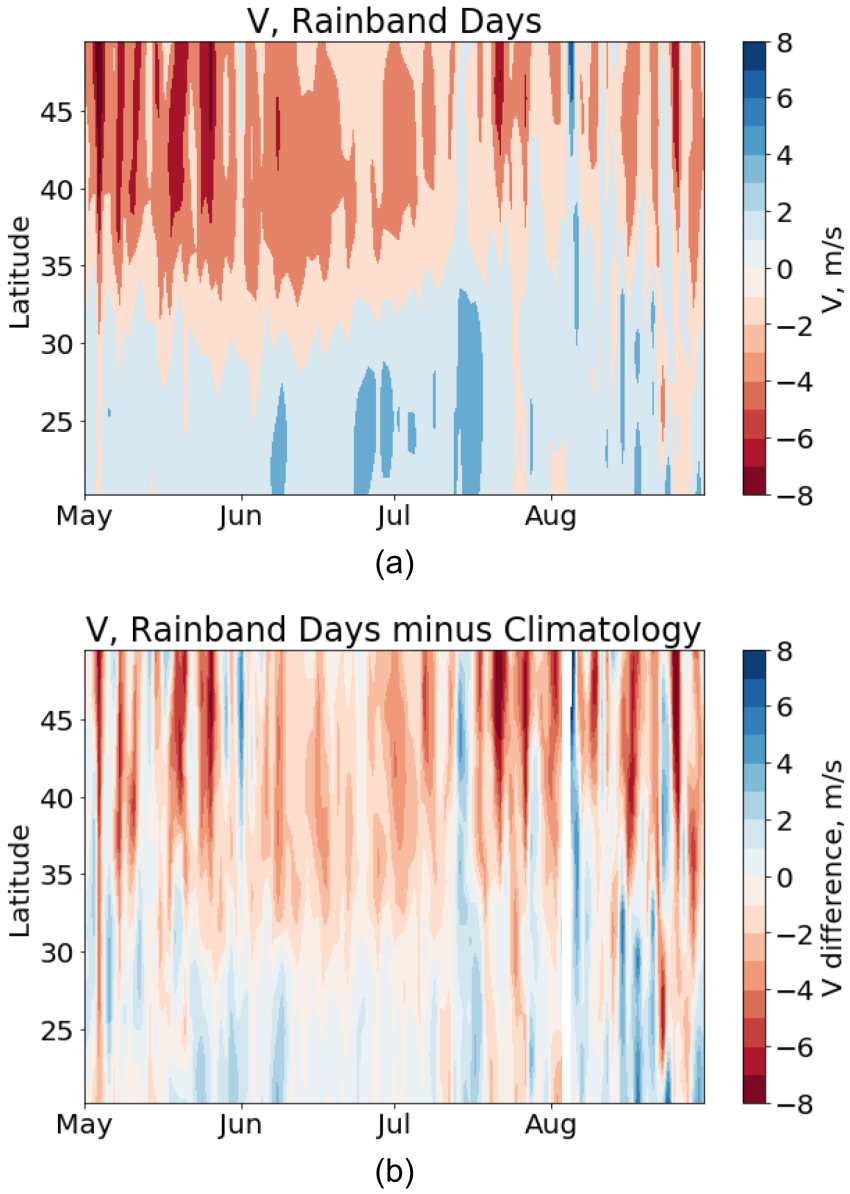


Figure 2.13: The composite of the meridional wind for all the days when rainbands are detected. The meridional wind is averaged between 110°E and 120°E. (a) shows the meridional wind over the days with rainband events; (b) shows (a) minus the climatological meridional wind. The northerly wind is more prominent in August on rainband days than in the monthly average of August, suggesting that northerly wind is essential for the rainband even in August when northerlies start to weaken.

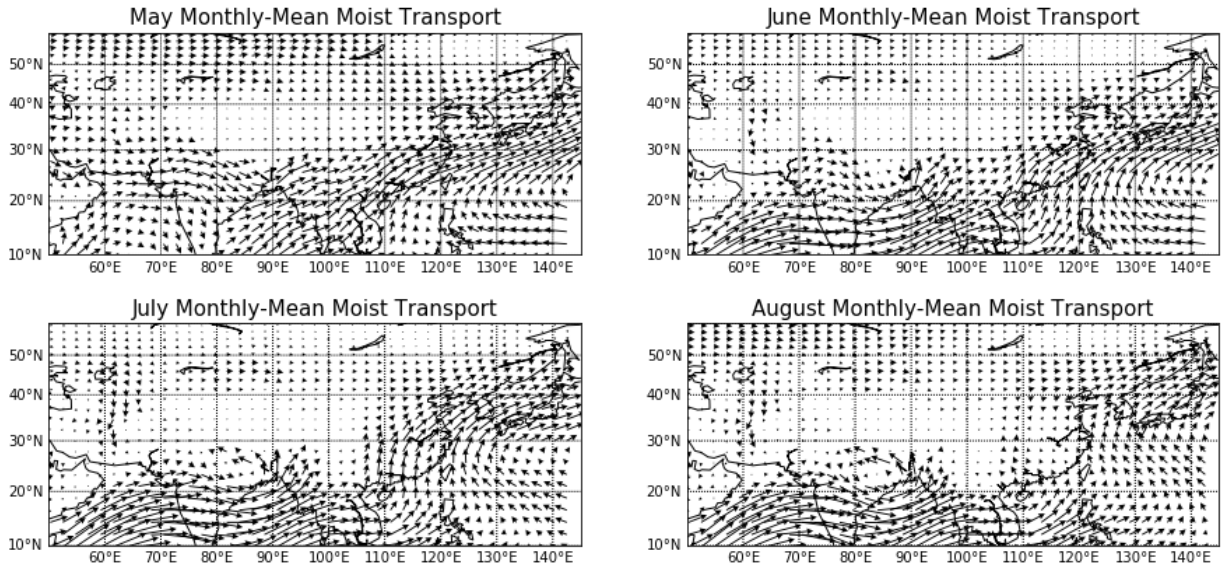


Figure 2.14: The column-integrated moisture transport from May to August(1979-2018). The moisture over East Asia comes from the westerly transport from the Bay of Bengal and the Western Pacific. The moisture transport from the Bay of Bengal weakens in August.

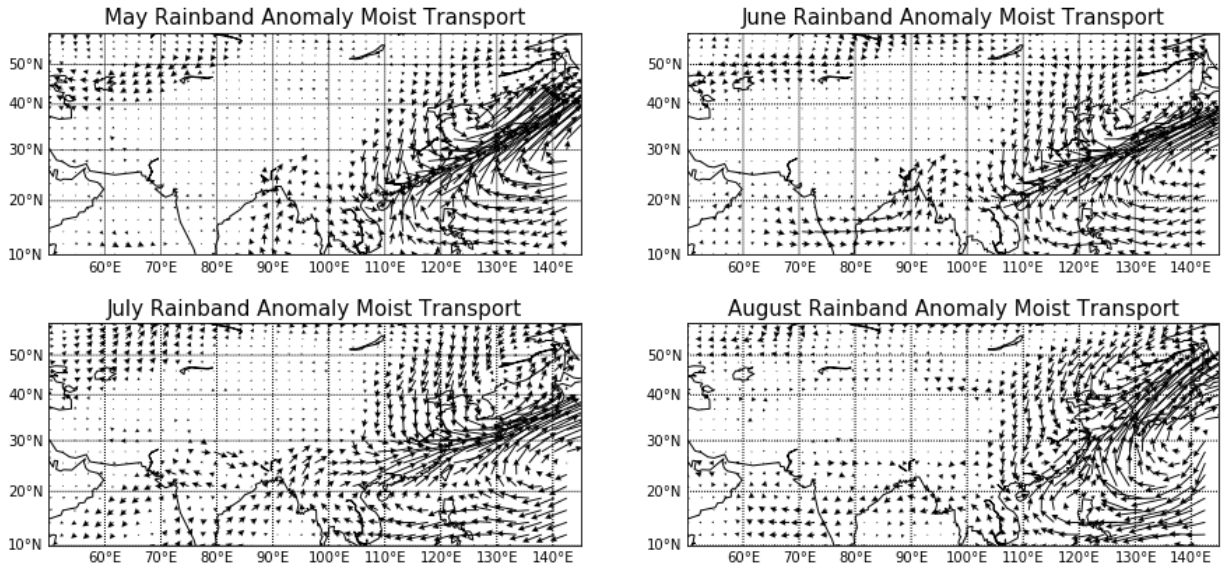


Figure 2.15: The column-integrated moisture transport from May to August(1979-2018) for the rainband-days anomaly(rainband-days minus the monthly average). The anomalous moisture transport for the East Asian rainbands mostly comes from the Western Pacific.

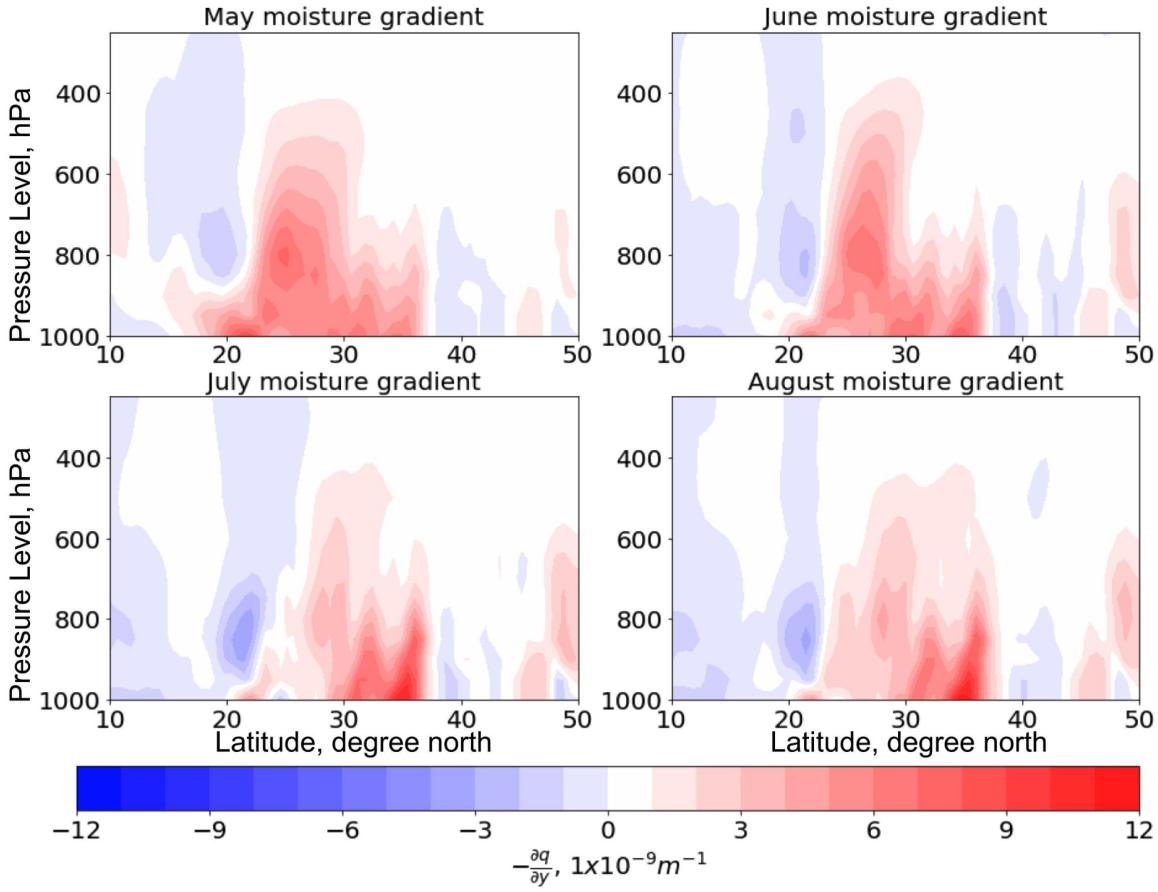


Figure 2.16: The climatology(1979-2018) of the meridional moisture gradient for May to August. A strong negative moisture gradient can signify a precipitation front. The strongest front in May occurs around 25°N in May and moves north to 30°N and beyond in August.

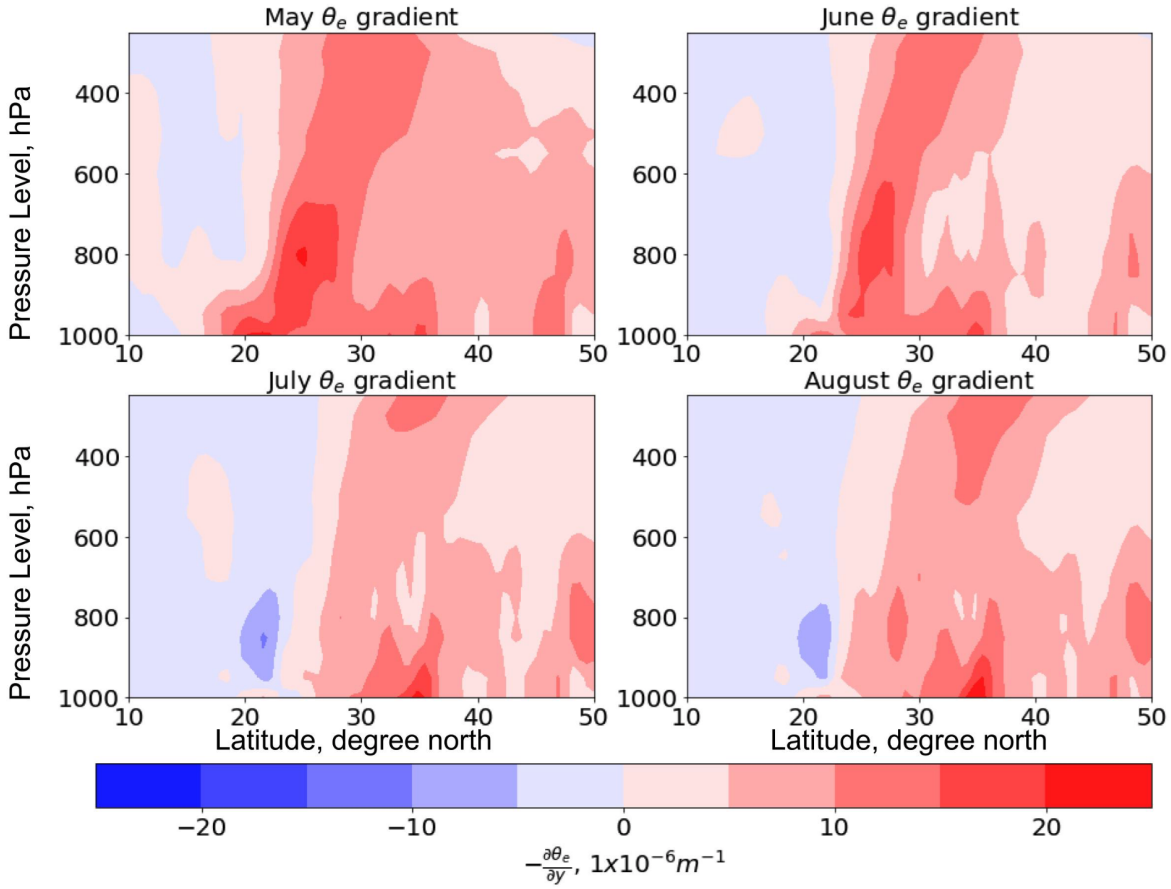


Figure 2.17: The Climatology of the meridional gradient in the moist static energy. A strong negative gradient(red) indicates a precipitation front. The strongest front in May occurs around 25°N in May, stays at the approximately same latitude in June. The strongest front moves north past 30°N in July and August.

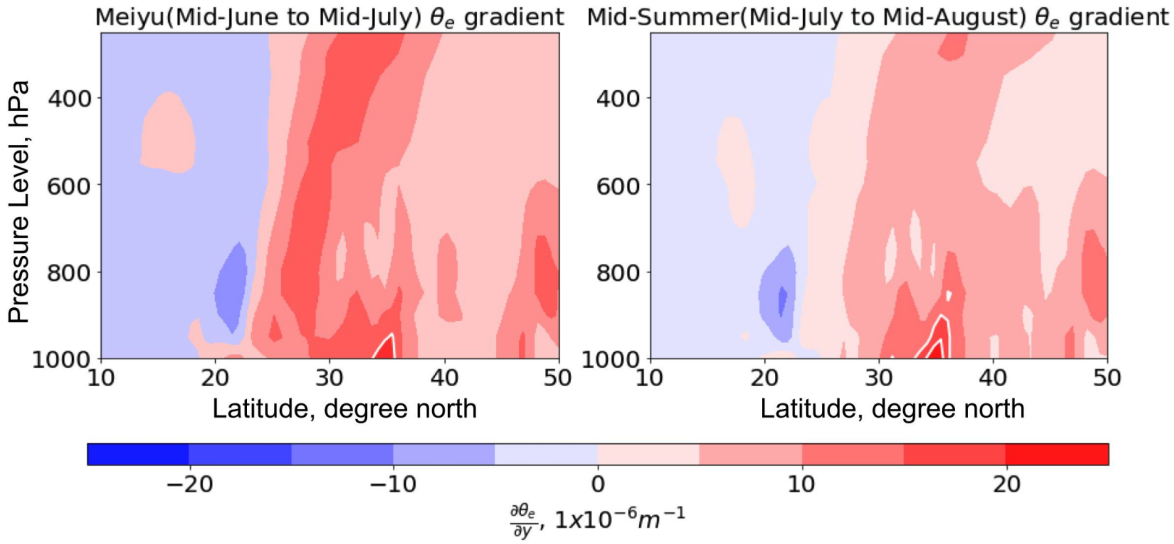


Figure 2.18: The climatology of the meridional gradient of the moist static energy in Meiyu season(June 16$^{\text{th}}$ to July 15$^{\text{th}}$) and the mid-summer season(July 16th to August 15th). A sharp front(red) occurs at 28°N for the Meiyu season; another front is at 35°N. In mid-summer, the sharp front at 28°N disappears, but the front at 35°N persists. The overall structure of the front shifts north from Meiyu to mid-summer as well.

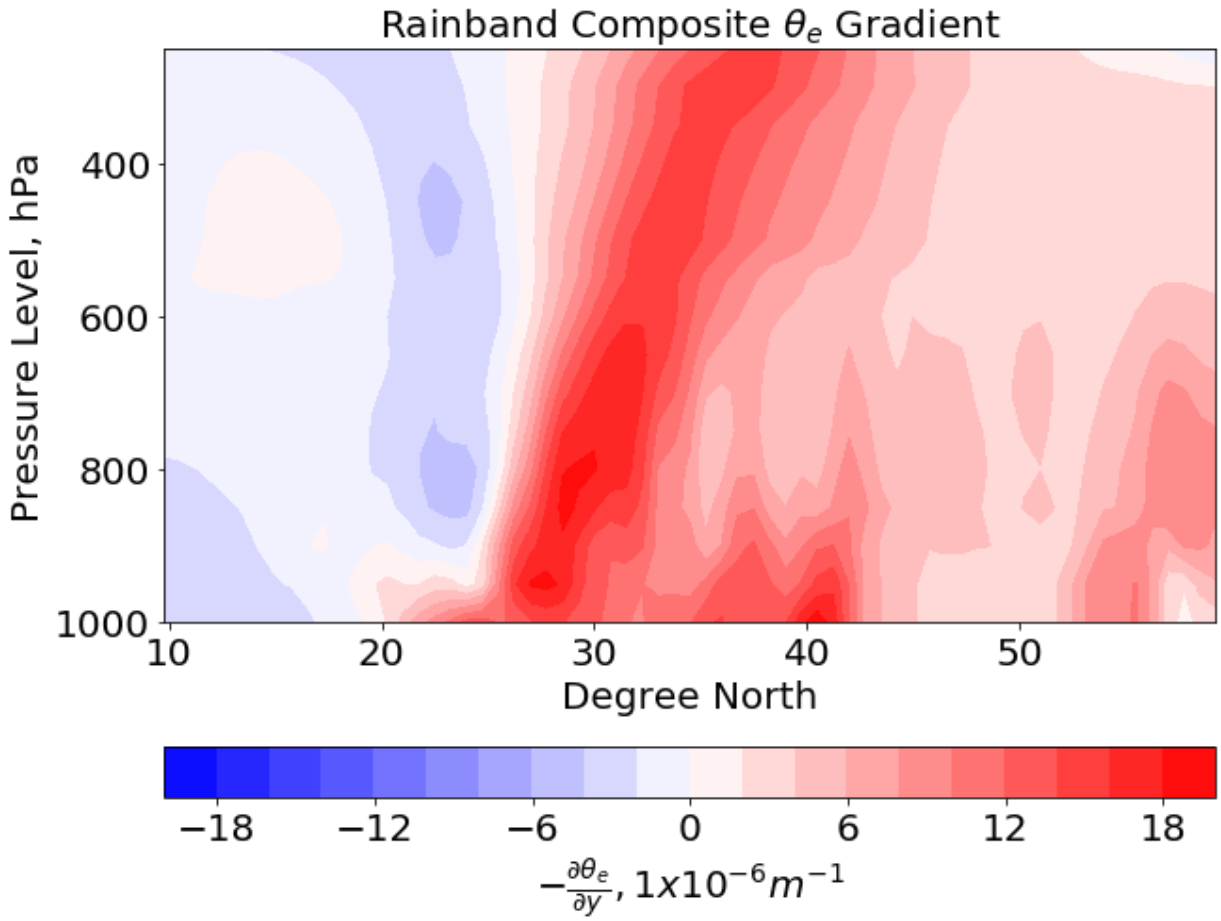


Figure 2.19: The rainband-day composite of the meridional gradient of the moist static energy. A sharp front(red) occurs at approximately 28°N; two secondary fronts are from 35°N to 42°N. The meridional gradient of the moist static energy for rainband days resembles that in June(in Figure 2.17) and in the Meiyu season(in Figure 2.18).

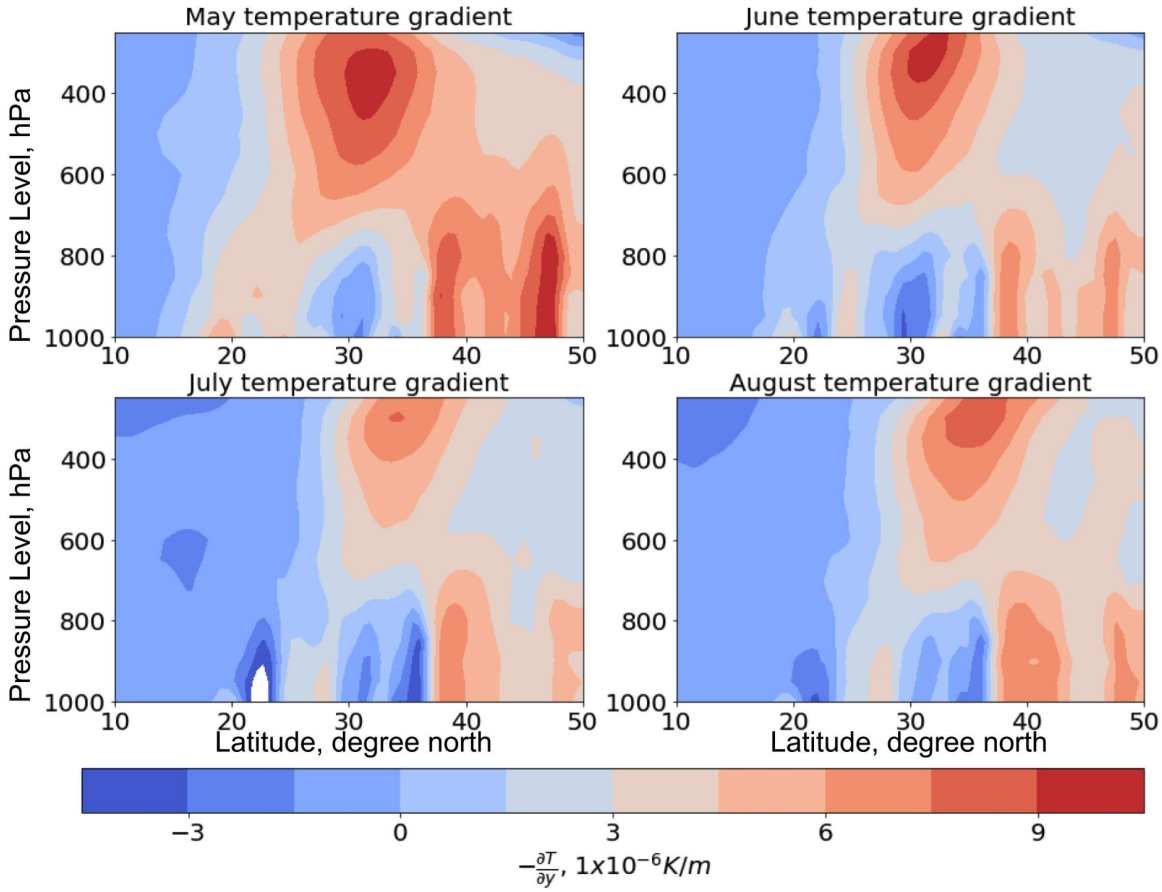


Figure 2.20: The climatology of the meridional temperature gradient averaged over 110°E and 120°E for May to August. A strong negative temperature gradient(red) is a signature of a precipitation front. From May to August, a weak signature of a front appears at approximately 28°N; a strong signature appears around 40°N. The weak signature around 28°N suggests that the signature of the precipitation front and the strong gradient of moist static energy are not dominated by the gradient of temperature.

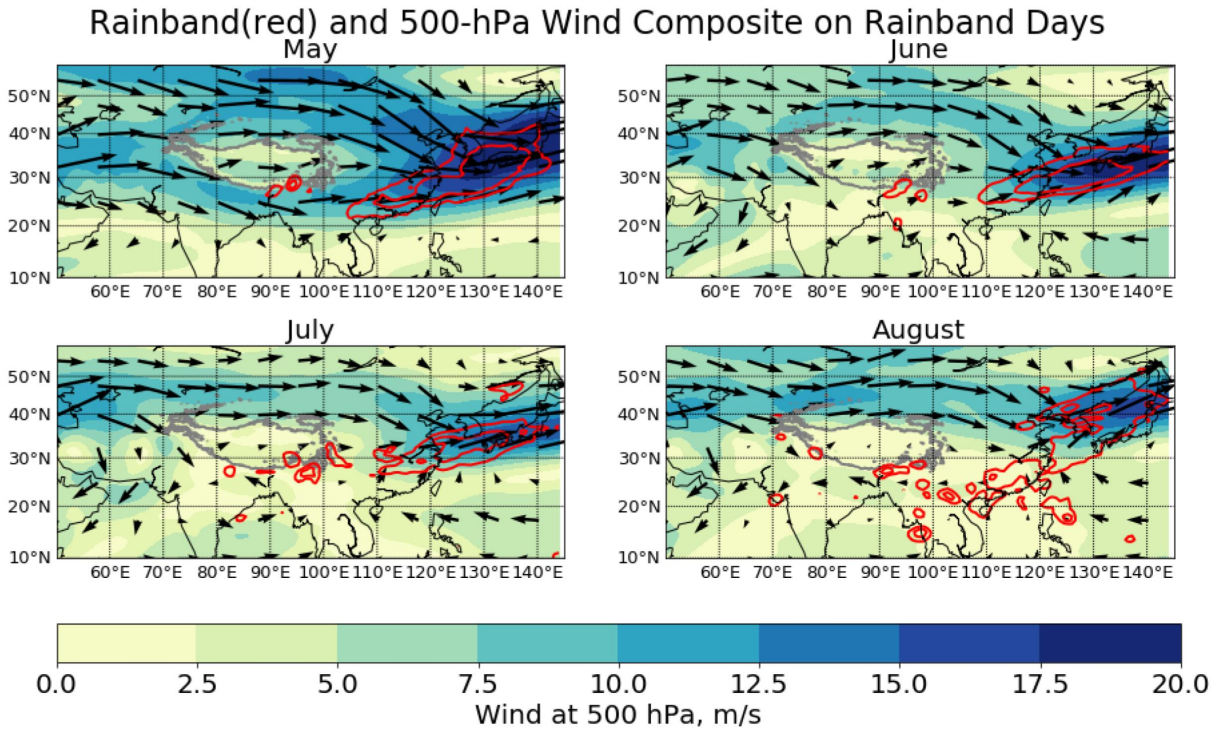


Figure 2.21: The climatology of the wind at 500 hPa(arrows and color shading) and the East Asian rainband anomaly as in Figure 2.6(red contour with the levels at 2 and 5 mm/day) from May to August. The gray contour shows the 4000 m topography(the Tibetan Plateau). The jet entrance(dark blue shading) is strong in all four months; the East Asian rainband closely follow the jet entrance.

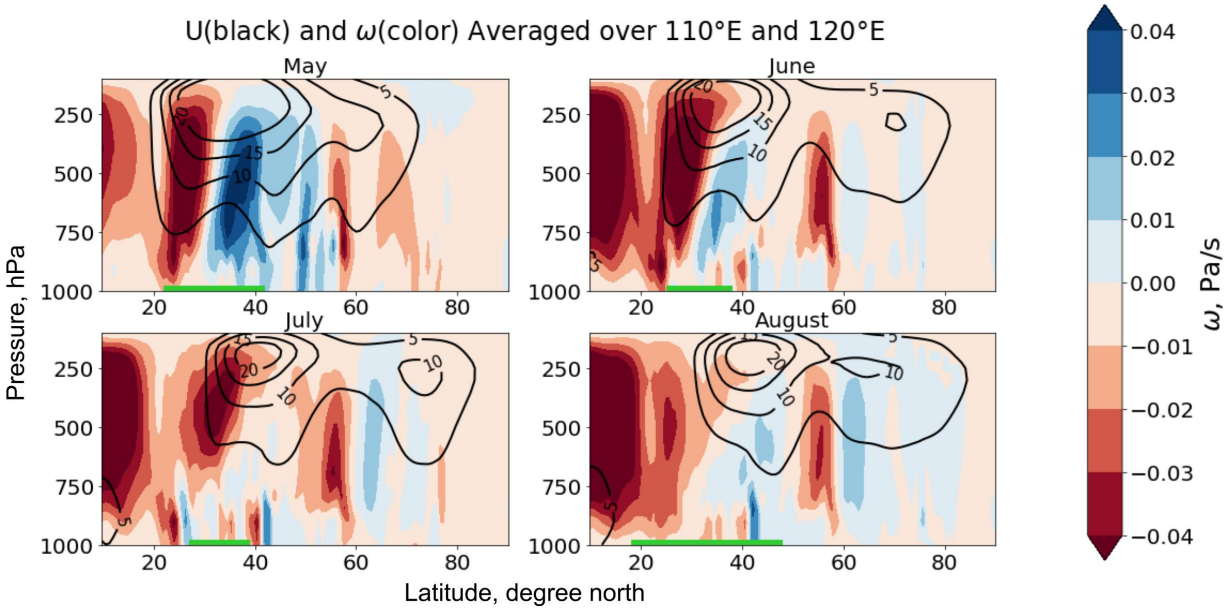


Figure 2.22: The pressure-latitude cross-section of the vertical velocity ω(color shading) and the zonal wind U(black contour, unit is m/s). The green line at the bottom of each subplot shows the latitudinal range of the East Asian rainband in each month. The longitudinal range is 110°E to 120°E. The ageostrophic flow is the most prominent in May, but not obvious in July and August.

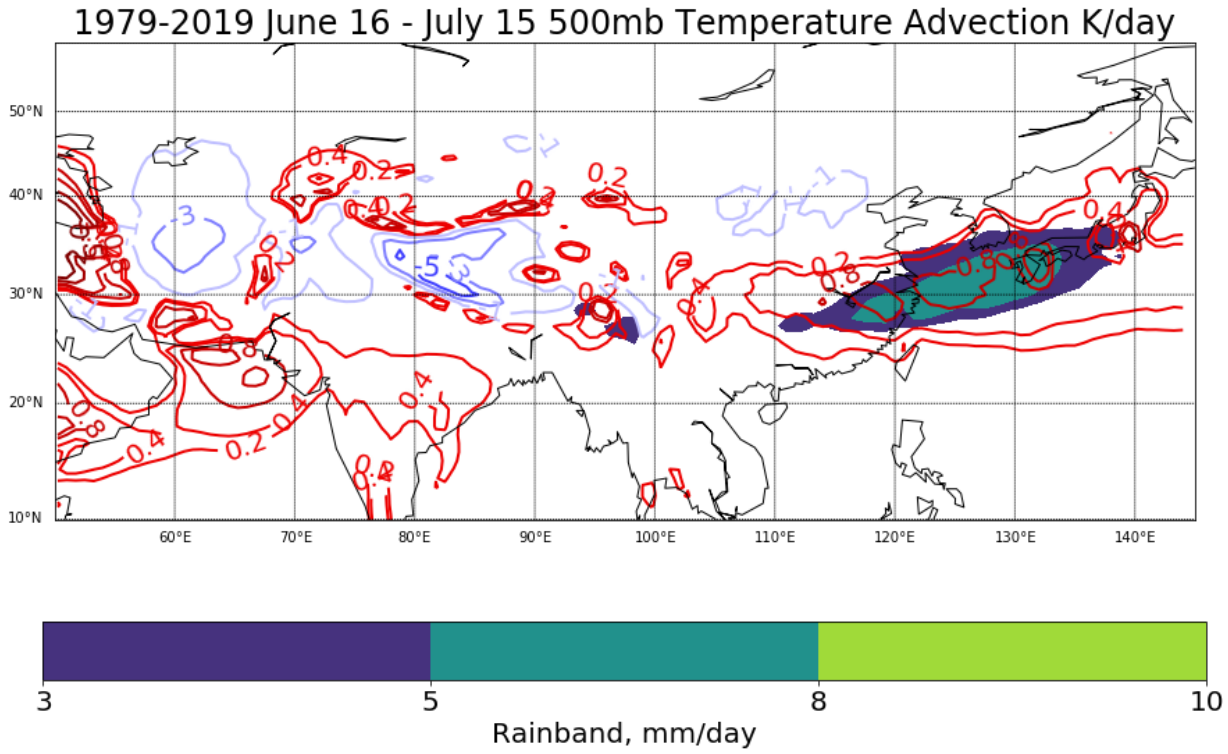


Figure 2.23: The temperature advection(in red and blue contour) and the detected rainband(in color) for the standard Meiyu season(June 16$^{\text{th}}$ to July 15$^{\text{th}}$). Red contours indicate positive advection of heat. The long strip of the positive heat advection near 30°N and from 110°E to 140°E collocates with the detected rainband well.

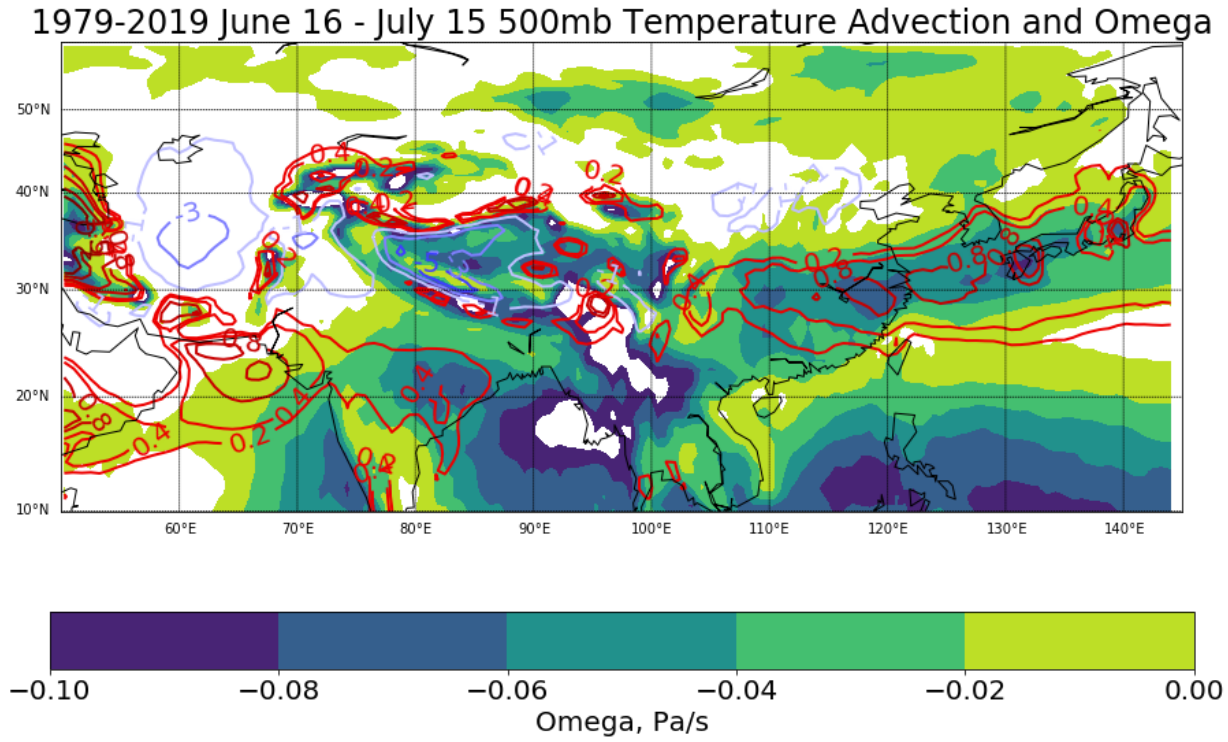


Figure 2.24: The temperature advection(in red and blue contour) and the vertical motion ω(in color) for the standard Meiyu season(June 16$^{\text{th}}$ to July 15$^{\text{th}}$). Red contours indicate positive advection of heat; dark colors indicate strong ascending motion(negative ω). The long strip of the positive heat advection near 30°N and from 110°E to 140°E collocates with the strong ascending motion.

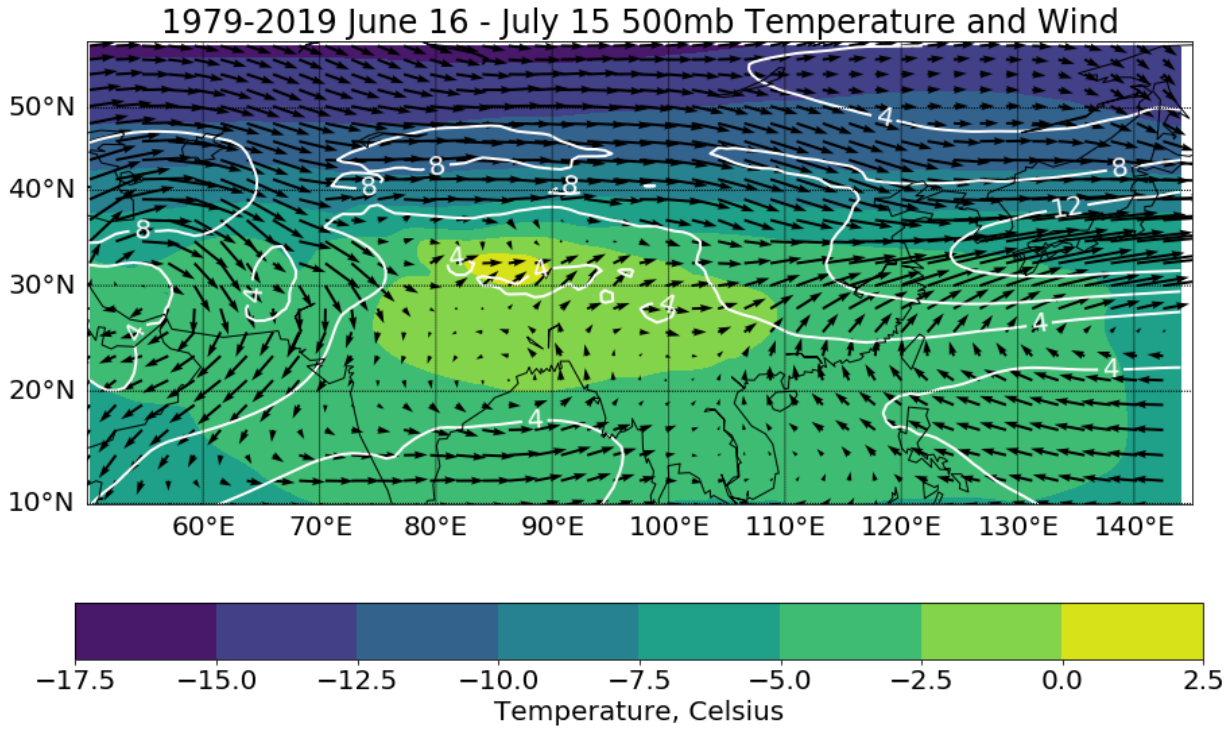


Figure 2.25: The climatology of the temperature and the wind at 500 hPa. The temperature is the warmest on top of the Tibetan Plateau; the westerly wind carries the heat from the top of the plateau eastward; the strong westerly wind from the eastern edge of the Tibetan Plateau and further east contributes to the heat advection shown in Figure 2.24.

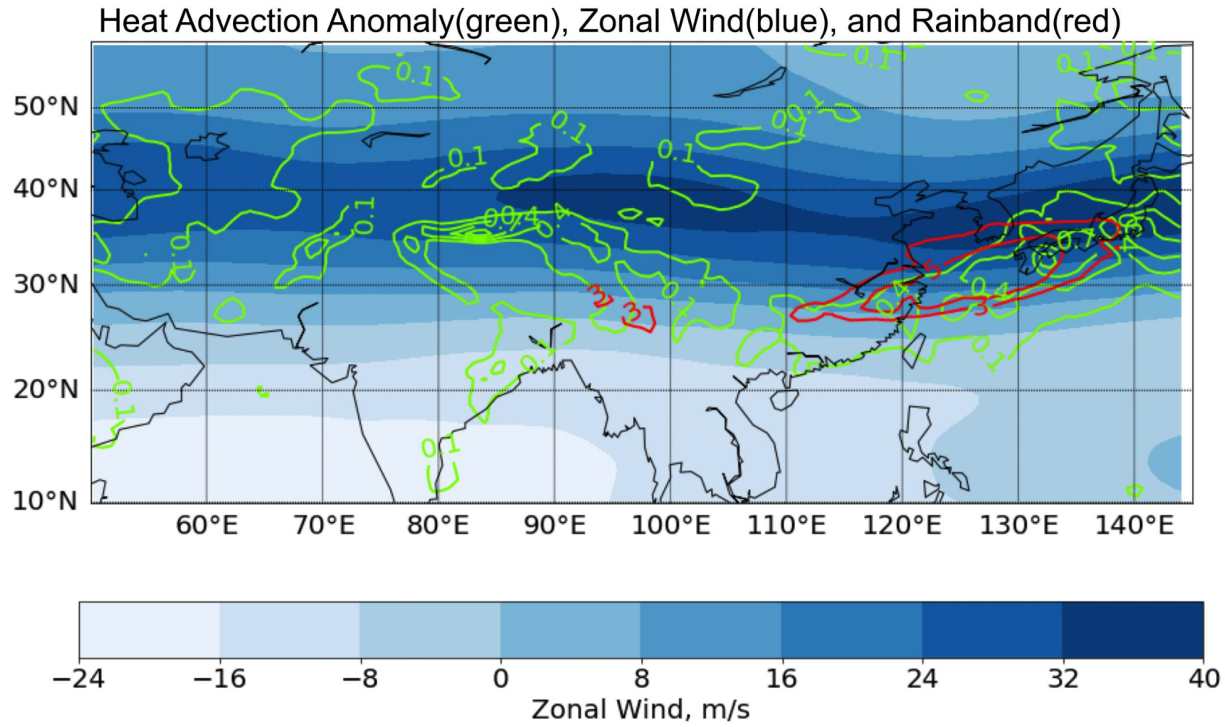


Figure 2.26: The temperature advection anomaly(rainband days minus seasonal average) in green contour, the detected rainfall anomaly(rainband days minus seasonal average) in red contour, and the zonal wind in blue for the standard Meiyu season(June 16$^{\text{th}}$ to July 15$^{\text{th}}$). The latitude of the positive temperature advection is slightly south of the latitude of the detected rainband; the maximum zonal wind is slightly north of the detected rainband.

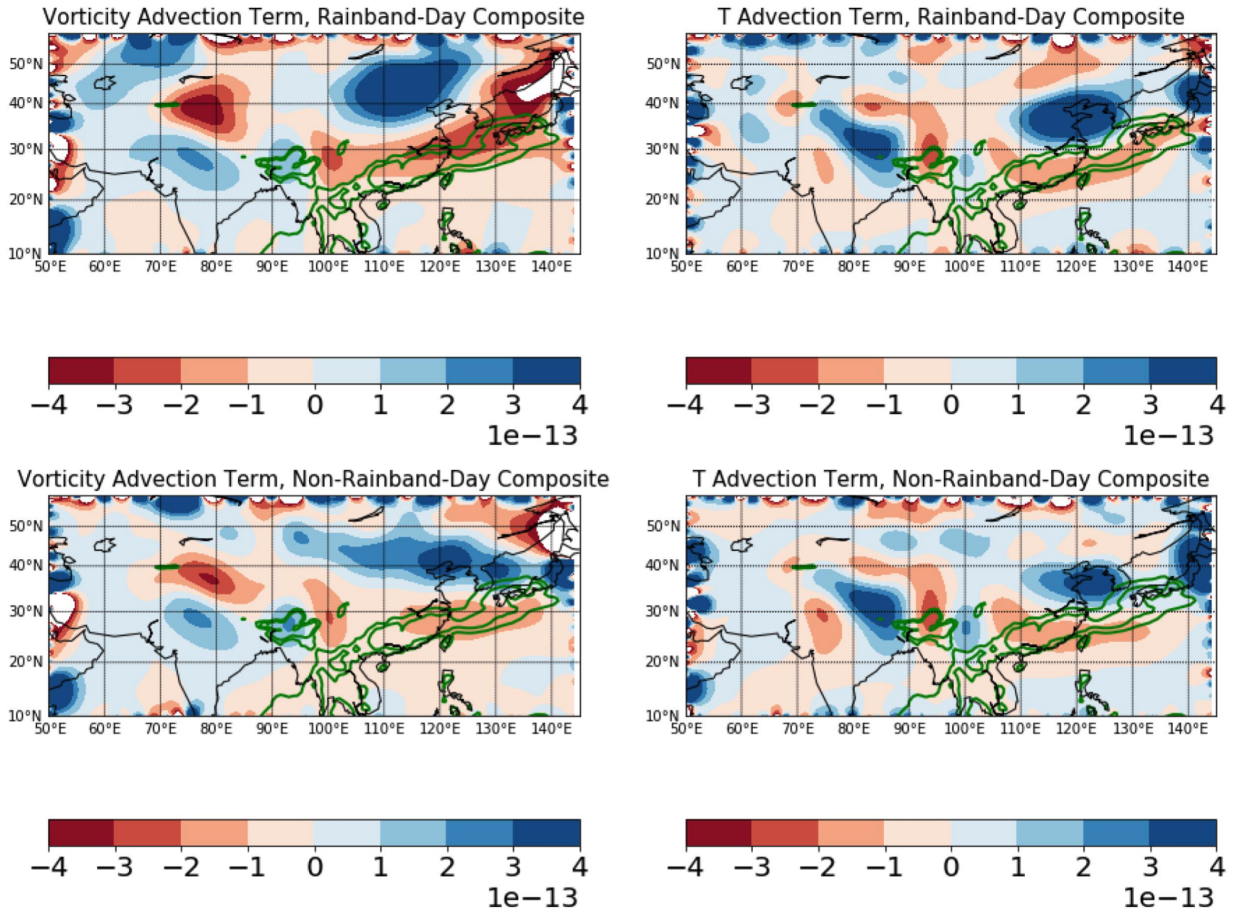


Figure 2.27: The vorticity advection term in Equation 2.1(left column) and the temperature advection term(right column) in color. The rainband-day composite total precipitation(top row) and non-rainband-day composite total precipitation(bottom row) in green contour(in 5 mm/day and 10 mm/day). The vorticity advection for rainband days is approximate twice the magnitude of the temperature advection for rainband days; both advection for non-rainband days are weak. The advection in all four panels follows the position of the detected rainband.

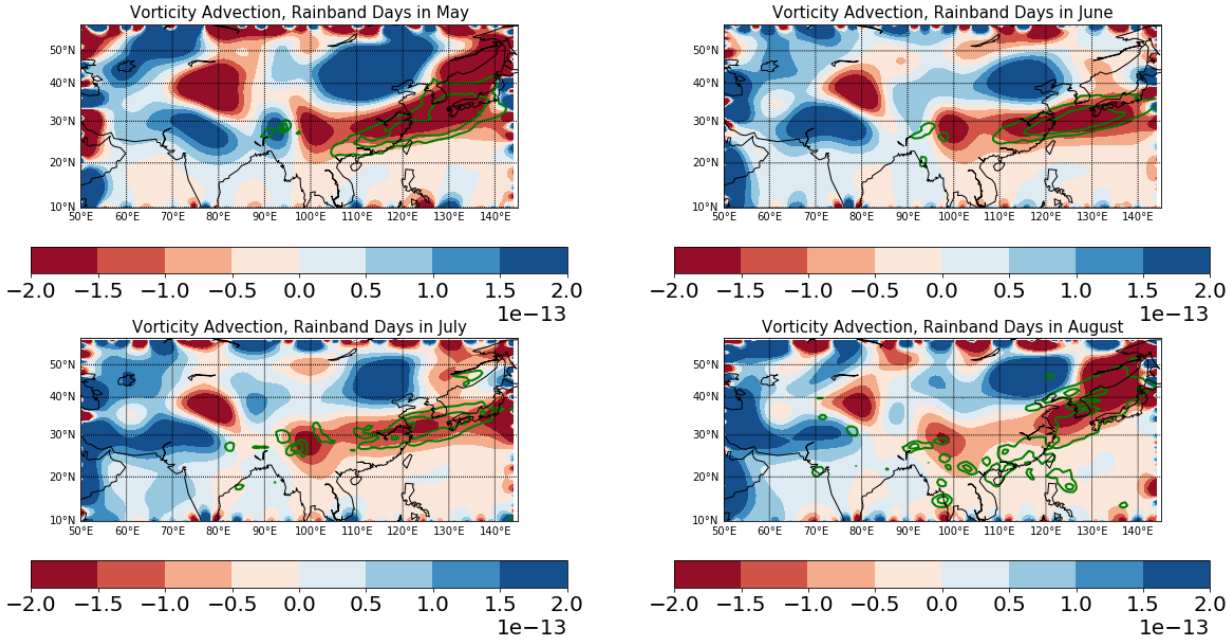


Figure 2.28: The vorticity advection term in Equation 2.1 for rainband days in the four months from May to August(color) and the anomalous precipitation on rainband days(green contour; 3 mm/day and 5 mm/day). The vorticity advection closely follows the position of the detected rainband in all four months.

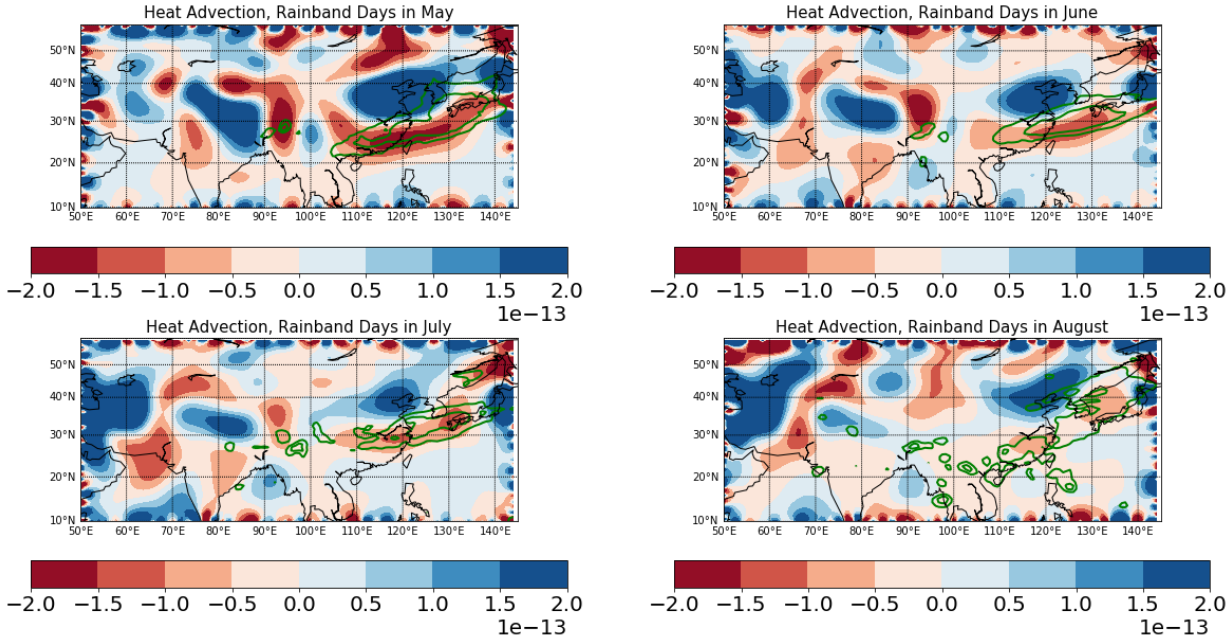


Figure 2.29: The temperature(heat) advection term in Equation 2.1 for rainband days in the four months from May to August(color) and the anomalous precipitation on rainband days(green contour; 3 mm/day and 5 mm/day). The heat advection also follows the position of the rainband but not as well as the vorticity advection does. The magnitude of the heat advection is also smaller than that of the vorticity advection in all four months.

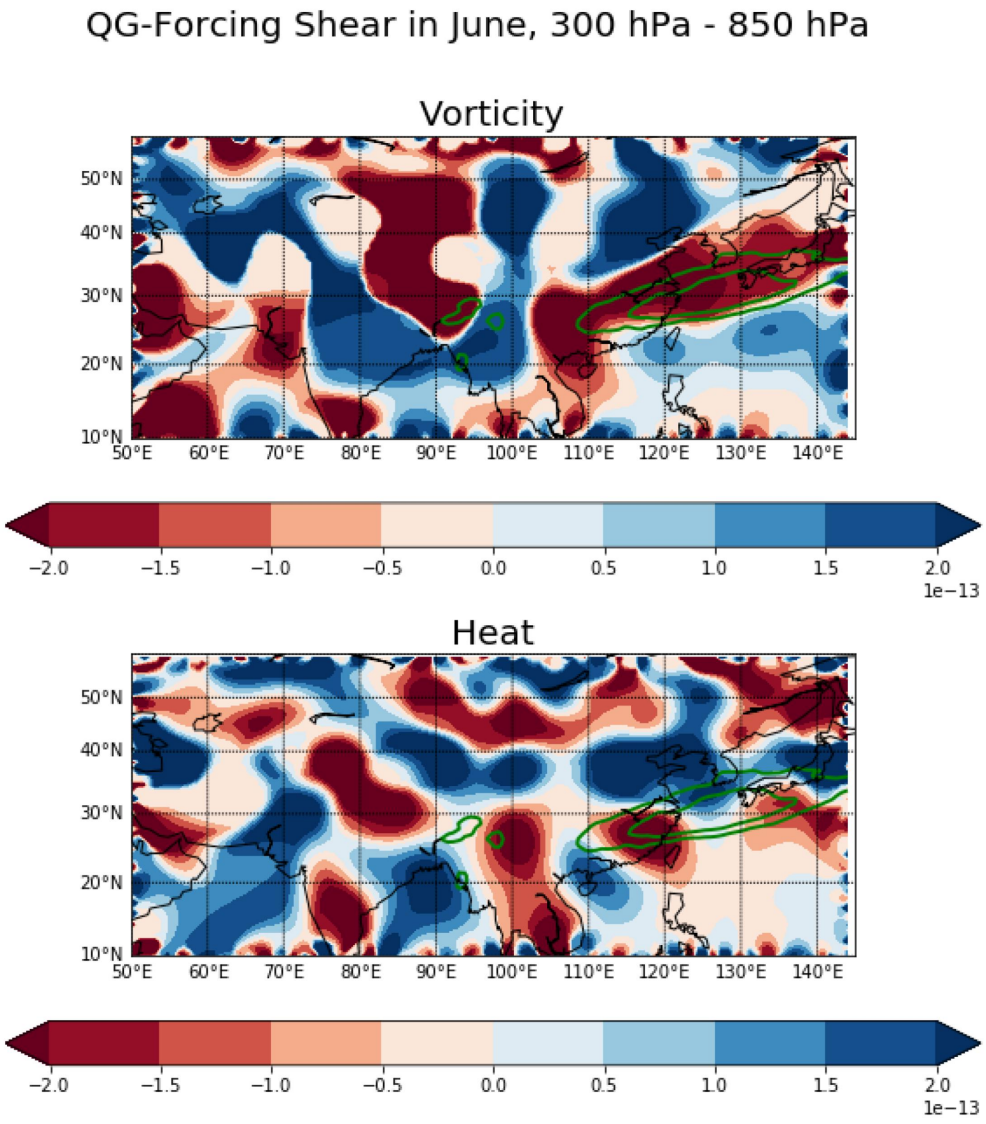


Figure 2.30: The difference between the QG forcing terms in Equation 2.1 at 300 hPa and 850 hPa in June(color shading). The green contour shows the anomalous rainband in June(contours are 3 mm/day and 5 mm/day). The vorticity forcing term shows a positive agreement the detected rainband; the heat forcing term does not show an agreement with the rainband.

Chapter 3

Orographic Stationary Rossby Waves: from Model and Reanalysis

3.1 Introduction

The East Asian rainbands have long been documented as a unique phenomenon not only because of their intensity and persistence but also their regular northward migration from spring to summer. This northward migration occurs contemporaneously with the northward movement of the core of the jet stream from its winter position south of the Tibetan Plateau to its summer position north of the Plateau. This synchrony has inspired a variety of theories attributing the dynamic origin of the East Asian rainbands to the jet stream(Yeh et al., 1959; Sampe and Xie, 2010; Molnar et al., 2010; Chiang et al., 2015b; etc.), with evidence from the earliest balloon measurement of the wind to the speleothem record in Chinese caves.

In this work, we consider the dynamic links between the East Asian rainbands and the jet stream from the perspective of the northerly winds associated with the jet stream. In Chapter 2, we show that the convergence of the meridional winds, especially the southward extent of the northerly wind, defines the latitudinal variations of the rainbands throughout the entire season. In this chapter, we explore the dynamic origin of seasonal northerly wind in the jet stream upstream(to the west) of the Tibetan Plateau. By tracing the link from the rainbands to the northerly wind(Chapter 2) and the link from the northerly wind to the upstream jet(Chapter 3), we establish a two-step relationship that could predict the latitude of the rainbands latitude based

on the upstream jet.

A direct comparison of the jet stream and the East Asian rainbands is difficult, and the result is ambiguous at best. If we focus on the maximum zonal jet on the 200 hPa level, which represents the subtropical jet, neither the latitude nor the timing of the migration matches perfectly for the jet and the rainband. The jet stream starts moving north in March, while the rainbands do not do so until mid-May(Figure 3.1). The jet stream also starts from a much lower latitude around 27.5°N and moves northward faster than the rainbands; by mid-May, the jet stream already moves past 35°N, but the rainbands are still around 30°N. In early June, the jet stream moves past 38°N, the northern edge of the Tibetan Plateau, but the rainbands are still around 33°N and are at their peak strength.

In this chapter, we first use a simple one-layer barotropic quasi-geostrophic model to illustrate how the jet stream causes the seasonal northerly winds over East China, which in turn play a critical role in the formation of the rainband. Then we show that reanalysis data(ERA-interim) are consistent with the results of the model. Finally, the rainbands, the northerly winds, and the upstream jet stream are brought together for a complete chain of not only correlation but physical causation.

3.2 A Simple One-Layer Barotropic Quasi-Geostrophic Model

In Chapter 2, we find that a northerly component of the meridional wind over East China, strongest near the 500-hPa surface, dominates the entire season of rainbands. This kind of zonal asymmetry hints at a planetary wave, especially considering East Asia is located right next to the Tibetan Plateau, the highest topography on earth. Previous studies contemplate the dynamic role of the Tibetan Plateau in the forming of the East Asian summer monsoon(e.g. Molnar et al., 2010); topography in other parts of the world, albeit lower, has also contributed to the local formation of banded precipitation(e.g. Fairman Jr et al., 2016).

To understand this zonally asymmetric circulation, the simplest way is to treat it as a perturbation of the zonally symmetric flow and to linearize from

the zonally symmetric state. In other words, we treat the jet stream as an a priori so that this flow generates a stationary wave when forced upon the Tibetan Plateau. This approach ignores the other zonal asymmetries(from land-sea interaction and other topography, for example) and assumes the nonlinear interactions are negligible. Our goal here is not to use a perfectly realistic model that takes everything into account, but rather to find the simplest theory that can largely explain the connection between the jet stream and the northerly winds over East China.

The potential vorticity is a powerful tool to explain planetary flows in that it takes into account both the Coriolis effect, the rotation of the air parcel itself, and the encounter of topography by the stretching term. Potential vorticity is conserved for individual air parcels, so the three terms(Coriolis, rotation, and topography) can be broken down into a mean state and a perturbation.

In a one-layer quasi-geostrophic model, the conservation of potential vorticity q in the presence of topography is governed by

$$\frac{Dq}{dt} = 0 \tag{3.1}$$

$$q = \zeta + \beta y - \frac{f_0}{H}(\eta - h_b) \tag{3.2}$$

where ζ is the flow vorticity, $f_0+\beta y$ is the Coriolis parameter, H is the average depth of the channel, η is the height of the free surface, and h_b is the bottom topography.

The flow variables $\mathbf{x} = \{u, v, q, \zeta, \eta\}$ can be expressed as the sum of a background state and a perturbation $\mathbf{x} = \overline{\mathbf{x}} + \mathbf{x}'$. Equations 3.1 and 3.2 can be linearized about a mean state with a flat bottom and a zonal velocity $\overline{u}(y)$ to yield

$$\frac{\partial q'}{\partial t} + \overline{u}\frac{\partial q'}{\partial x} + v'\frac{\partial \overline{q}}{\partial y} = 0 \tag{3.3}$$

Following Charney and Eliassen (1949), an Ekman dissipative term $-r\zeta'$ is added to remove resonant singularity. The perturbation potential vorticity equation becomes

$$\frac{\partial \zeta'}{\partial t} - \frac{f_0}{H}\frac{\partial \eta'}{\partial x} + \overline{u}\frac{\partial \zeta'}{\partial x} + \beta v' + [-\overline{u}\frac{f_0}{H}\frac{\partial \zeta'}{\partial x} - v'\frac{\partial \overline{u}^2}{\partial y^2} - v'\frac{f_0}{H}\frac{\partial \overline{\eta}}{\partial y}] = -\overline{u}\frac{f_0}{H}\frac{\partial h_b}{\partial x} - v'\frac{f_0}{H}\frac{\partial h_b}{\partial y} - r\zeta' \tag{3.4}$$

We define a streamfunction $\Psi = \frac{g}{f_0}\eta$, such that

$$\overline{u} = -\frac{g}{f_0}\frac{\partial \overline{\eta}}{\partial y}$$

$$u' = -\frac{\partial \Psi'}{\partial y} = -\frac{g}{f_0}\frac{\partial \eta'}{\partial y}$$

$$v' = \frac{\partial \Psi'}{\partial x} = \frac{g}{f_0}\frac{\partial \eta'}{\partial x}$$

$$\zeta' = \frac{\partial v'}{\partial x} - \frac{\partial u'}{\partial y} = \nabla^2 \Psi'$$

Equation 3.4 can then be written as:

$$\frac{\partial}{\partial t}(\zeta' - \frac{{f_0}^2}{gH}\Psi') + \overline{u}\frac{\partial \zeta'}{\partial x} + \beta v' - v'\frac{\partial \overline{u}^2}{\partial y^2} = -\overline{u}\frac{f_0}{H}\frac{\partial h_b}{\partial x} - v'\frac{f_0}{H}\frac{\partial h_b}{\partial y} - r\zeta' \tag{3.5}$$

In the sections below, we use Equation 3.5 to investigate the variations in topographic Rossby waves for four cases with combinations of u and h_b. The cases start with the simplest setup and increase in complexity to the one that mimics the observations. The cases are as following: (1)a 1-D Gaussian mountain with a zonal wind, (2)a 2-D Gaussian mountain with a uniform impinging zonal wind, (3)a 2-D Gaussian mountain with a varying profile of zonal wind, and (4)realistic Tibetan Plateau with realistic zonal winds. The first case uses the steady-state solution to examine the excited Rossby waves, while the other three use a finite-differencing method to solve for the solutions.

3.2.1 A Steady-State solution for a 1-D Gaussian Mountain

Holton and Hakim (2013) and Vallis (2017) have shown that a sinusoidal boundary

$$h_b = Re[h_0 exp(ik_b x)]cos(l_b y)$$

excites Rossby waves that travel with a velocity of $\overline{u} - \frac{\beta}{K}$, where $K = \sqrt{(k^2 + l^2)}$ is the total wave number. The steady state stream function solution to Equation 3.5 is:

$$\Psi' = Re[\Psi_0 exp(ikx)]cos(ly) \tag{3.6}$$

with

$$\Psi_0 = \frac{f_0 h_0}{H(K^2 - {K_s}^2 - i\epsilon)}$$

where $\epsilon = r\frac{K^2}{k\overline{u}}$.

The topographic Rossby wave $k = k_b, l = l_b$ is stationary when $\overline{u} - \frac{\beta}{K_s} = 0$, or $K_s = \beta/\overline{u}$. In other words, when $\overline{u} = \frac{\beta}{\sqrt{({k_b}^2 + {l_b}^2)}}$, the topographic Rossby wave excited by the sinusoidal boundary is stationary and has the largest amplitude.

We consider a cyclic channel centered at 33°N(approximately the centroid of the Tibetan Plateau) with H = 10km, longitudinal extent of 40,000 km(approximately the circumference of Earth at 33°N), with a Gaussian-shaped mountain at its center x_0:

$$h_b = Aexp\left(-\frac{1}{2}(\frac{x - x_0}{x_m})^2\right)$$

The mountain has a peak height of 4 km and a zonal scale x_m of 400 km. We solve Equation 3.5 with a Fourier Transform with 128 modes.

Figure 3.2 shows v' and Ψ' for various $\overline{u} = U$, where U is constant. With the same Gaussian mountain, a stronger impinging U leads to stationary Rossby waves with stronger northerly wind immediately downwind of the mountain peak and longer wavelengths. For U=10 m/s, the wavelength is so short that the northerly flow is <10 m/s and extends only 20 km downwind of the peak, while the corresponding values are 20 m/s and 400 km for U=70 m/s. It is worth noting that when U is increased from 40 m/s to 70 m/s and 100m/s, the peak northerly winds(the strongest negative v') are approximately the same while the wavelengths increase.

While the wavelength of the stationary orographic Rossby wave is determined by the strength of the zonal flow, the amplitude of the wave is determined by the height of the mountain. With a zonal flow of 40 m/s, the zonal scale of the mountain of 400 km, and peak height varying from 500 m to 6500m, the stationary Rossby waves all have the same wavelength, but with the amplitude increasing with peak height(Figure 3.3). A U of 40 m/s is close to the average speed of the jet stream in spring and early summer west of the Tibetan Plateau. The average altitude of the Tibetan Plateau is 4500 m, and so should excite a downstream Rossby wave with the maximum northerly wind of 10-20 m/s. The downstream meridional wind also agrees with the observation of 10-20 m/s. It is worth noting that the Mongolian Mountains centered around 48°N can also have an impact on the stationary Rossby waves in the winter, although the Tibetan Plateau is the dominating factor from April to June(White et al., 2017).

3.2.2 Gaussian Mountain in 2D: Finite-Difference Method

To further explore the stationary Rossby waves generated by different mean flows, a 2-dimension model is necessary, because not only the topography itself has a profile in the meridional direction(not infinite in the y-axis), but the zonal wind is also not uniform. All year round the zonal mean flow, in the mid to upper-troposphere, should have a meridionally concentrated jet of high speed near the subtropics or the mid-latitude, depending on the time of the year. It is therefore unrealistic to represent this wind as being meridionally uniform.

We set up the 2-D quasi-geostrophic model as following: the domain is 24,000 km in both directions, with 65 grid points in each direction. The domain is cyclic in the x-direction. We assume the center of the channel is at 33°N(approximately the latitude of the centroid of the Tibetan Plateau) and use an Ekman damping factor of $5\times10^6 s^{-1}$ following Holton and Hakim (2013). We solve for Equation 3.5 using a finite differencing method with a second-order leapfrog scheme with a grid spacing of 375 km(64 grids in total) in both directions and integrate for 200 steps with a time step of 30 minutes.

The setup is illustrated in Figure 3.4. The mountain centers at (0,0) and has a 2-D Gaussian shape with a peak of 6000 m(black contour). The imposed zonal wind is uniformly 40 m/s in the y-direction, approximately the average zonal wind speed at 500 hPa in spring upstream of the Tibetan Plateau. The streamfunction is shown in colored contours. The flow is largely zonal south of the Plateau, but the Rossby wave starts to become prominent downslope of the mountain peak. A northerly wind dominates immediately to the east(right) of the mountain peak, and the flow switches to southerly. The wave within the latitudinal range of the Tibetan Plateau has a wavelength of approximately 10,000 km.

With the Gaussian circular mountain and the uniform zonal wind, we can again compare the streamfunction of the resulting Rossby waves from different upstream zonal winds and the height of the mountains. Figure 3.5 shows how the speed of the zonal wind and the height of the mountain matter to the shape of the flow. A taller mountain has a larger effect in creating a stationary Rossby wave; a faster zonal wind also gives a more obvious pattern of a wave in the streamfunction. When the wind is at 40 m/s and the mountain at 4 km or 6 km, the flow has a northerly component right to the east of the mountain. When the wind is too slow or too fast, the flow does not show a prominent northerly to the right of the mountain. A zonal wind of 40 m/s is a typical speed of the jet stream to the west of the Tibetan Plateau from spring to early summer; the Tibetan Plateau has an average elevation of approximately 4500 m. The combination of the wind speed and the height of the mountain in spring and early summer creates the perfect condition for the northerly winds to occur over East China.

3.2.3 Realistic Wind Profile and Topography

Further improvement of the 2-D model can be made by imposing a realistic profile of the zonal wind, using a realistic shape of the mountain, and extending the domain in the x-direction to avoid the downstream waves feeding into the upstream. One setup is that the zonal wind has a Gaussian profile with a peak of 40 m/s(similar to the realistic wind speed of a jet core in spring) and smoothly approaches 0 m/s away from the peak. When the peak wind is far south from the latitude of the mountain(Figure 3.6(a)), the Rossby wave

pattern is significantly weaker than that with the peak wind at the latitude of the Tibetan Plateau(Figure 3.6(b)). The wave weakens when the maximum of the wind shifts north of the topography. The difference among the three scenarios reveals, to the first order, the seasonality of the northerly winds over East China: when the jet core is far south or far north of the Tibetan Plateau, the strong wave pattern will not appear. The disappearance of the northerly winds due to the movement of the jet, in turn, explains the termination of the East Asian rainbands. A zonal wind profile with a sharper peak(Figure 3.7) shows a similar result, with a more concentrated Rossby wave downstream of the topography. When the wind profile is sharp, the Rossby wave almost disappears when the peak of the zonal wind is slightly north of the topography(Figure 3.7(c)). This disappearance suggests that a more meridionally concentrated jet core can lead to earlier termination of the rainband season because it is easier for the Rossby waves to weaken.

The conclusion remains the same when the zonal domain of the model extends to circle the earth and a realistic wind profile is imposed: the strongest northerlies appear when the strong zonal wind aligns with the Tibetan Plateau in latitude(the y-direction). Figure 3.8 shows the streamfunction in a domain that covers the entire northern hemisphere, with the Tibetan Plateau as the only topography and everything else at sea level. Monthly-averaged zonal winds between 70°E and 80° at the 200-hPa surface serve as the impinging flow. In May, the Rossby wave is strong because the peak of the zonal wind profile is close to the Tibetan Plateau(Figure 3.8(a)); when the jet moves north of the Tibetan Plateau and becomes weaker than 20 m/s, the downstream Rossby wave becomes weak, and the northerly wind to the east of the plateau is negligible(Figure 3.8(c)).

3.2.4 Conclusion

To conclude Chapter 3.2, with the aid of a simple one-layer barotropic quasi-geostrophic model of potential vorticity, we are able to explain the relationship of the northerly over East China and the jet stream to the first order. We further explore the important factors for the northerlies to happen at the correct location with the correct speed for the rainbands to happen; the shape of the zonal wind profile, the height of the mountain, and the position of the

mountain are all important. A mountain with a height between 4000 m and 6000 m will generate Rossby waves downstream of the mountain and create northerlies of wind speed between 10 m/s and 20 m/s as seen in Chapter 2. The climatological profile of the zonal wind in May will generate a prominent wave, while the profile in August is weak and centered too far north to create such a wave. We build up from providing the 1-D steady-state solution to a Gaussian mountain to using a finite-difference method with realistic winds and topography. It is worth noting that a single-layer linear model is a stepping stone to a more comprehensive non-linear response to orography, as the orography will also influence the heating to the atmosphere and the transient eddy fluxes. We are aware of the many extraordinary modeling experiments done on this topic(e.g. Held et al., 2002), but the simplest linear approach is able to illustrate the point that the northerlies important for East Asian rainbands have their location and strength determined by the upstream zonal wind interacting with the Tibetan Plateau.

3.3 The Connection Between the Westerly Jet West of the Tibetan Plateau and the Northerly Wind over East China

In Chapter 3.2, we use a one-layer quasi-geostrophic model of potential vorticity to illustrate that a zonal mean flow can interact with topography and generate topographic Rossby waves that propagate downstream. We propose that this mechanism gives rise to the northerly wind over East China, downstream of the Tibetan Plateau, from the subtropical westerly jet stream interacting with the Tibetan Plateau. The resulting northerly wind, in turn, plays a crucial role in forming the banded precipitation over East China, as explained in Chapter 2.

In this section, we aim to make the connection of the westerly jet stream to the northerly wind over East China using historical observational data. We omit thermal forcing which is the other major source of stationary waves, topographical features smaller than the Tibetan Plateau, and transient disturbances. However, in mid-latitude, with enough years of data to eliminate

the transients, the simple linear model we introduce in Chapter 3.2 should give a reasonable approximation to the wind field. In fact, with fine-tuning of the friction and resonant wavenumber, a similar one-layer Charney-Eliassen model achieves close approximation to observation using a realistic topography at 45°N(Vallis, 2017, Figure 3.9)

We will begin this section by a detailed examination of the meridional wind, its seasonal cycle, latitudinal and longitudinal extents, and interannual variability over East China and downstream of the Tibetan Plateau in general. Then we connect the meridional wind downstream of the Tibetan Plateau to the westerly zonal flow west of the Tibetan Plateau using the topographic Rossby wave framework presented in Chapter 3.2. In the end, we investigate the variability of the north-south migrations of the East Asian rainbands and their relationships to the strength of the upstream westerlies.

In Chapter 3.3, we will use historical data of the zonal and meridional wind from ERA-interim(Dee et al., 2011) from 1979 to 2018. The wind field at the 500-hPa surface will be primarily used because this is a height where the surface drag is negligible(compared to 850-hPa), the zonal wind is strong enough to have an effect, and where the Tibetan Plateau can still reach(about 5,500 meters above the sea level).

3.3.1 Climatology of the Northerly Wind

The northerly wind is an important feature of the atmospheric flow accompanying the banded precipitation over East Asia in spring and summer, as described in Chapter 2. This wind is also a dominant feature over East China north of approximately 32°N from May to August. We shall focus on the domain of East China, 110°E to 120°E and 20°N to 50°N.

A climatology of this northerly wind averaged from 1979 to 2018 reveals its prominent seasonal cycle. Figure 3.10 shows the climatology of the maximum speed of the 500 hPa northerly wind over East China; the time resolution is 6-hour. The northerly wind is strong around 20 m/s during winter and weakens as spring approaches; from May to August, the maximum northerly weakens further from 18 m/s to 10 m/s. In the fall, this northerly wind strengthens again and reaches its peak in December.

The position of the maximum northerly wind over China also changes through the year(Figure 3.11). In the winter, this northerly lingers north of 42°N and is strong, approximately 20 m/s. In May, the maximum northerly wind weakens and starts to move southward and reaches approximately 10 m/s and 36°N in July and August. In the fall, the maximum northerly strengthens and shifts north to its maximum value and northernmost position in December.

The climatology of the longitudinal position of the maximum northerlies completes the picture of its seasonal changes(Figure 3.12). The strongest northerly wind has a greater likelihood to be east at 115.5°E in the winter when the winds are strong and west of 114.5°E in the summer when the wind is also stronger. The changes in its longitudinal position are relatively small compared to those in its latitudinal position(a 2° change compared to a 10° change), but it is nevertheless important to recognize the east-west movement of the northerly wind in this region. We note that the longitudinal position of the rainbands over East Asia also goes through noticeable changes from the early season to late season, even though the latitudinal change is more prominent and has been the center of focus for many previous studies.

A broad view of the meridional wind in the same range of latitude(36°N to 46°) reveals the uniqueness of this northerly flow over East China. Figure 3.13 presents the meridional wind(V) from upstream of the Tibetan Plateau at 60°E(approximately where Iran borders Afghanistan) to 120°W(approximately the west coast of the United States). The western and eastern boundaries of the Tibetan Plateau are marked by dashed white lines(at 75°E and 105°E, respectively). The east coast of China is marked by a solid white line(at 120°E). The only longitudes where northerlies are strong and dominant for the most part of the year are over East China between 105°E and 120°E(dark red). The rest of the meridional winds within this latitude range of 36°N to 46°N are predominantly southerlies.

Over the course of a year, the northerlies dominate East China over winter and spring. Starting in May, the northerly wind between 105°E and 120°E weakens and is eventually replaced by southerlies in August. In the fall, the weak northerlies return and strengthen in October and November, reaching their peaks in December. This primary northerly wind also encompasses the region as far east as around 140°E, and this west-east spread in part can ex-

plain why Japan also experiences the banded precipitation. This climatology is consistent with the findings from Figure 3.10 and Figure 3.11 although it focuses on a range of longitudes instead of searching for the maximum within a region.

The meridional wind over the North Pacific from 140°E eastward also shows a seasonal cycle, albeit in the opposite direction from that over East China(Figure 3.13). In winter, the meridional winds from 140°E to 120°W are predominantly strong southerlies. The southerlies progress westward and weaken to June when weak northerlies appear around 150°E. In other words, the change of direction of the meridional winds between East China and the Pacific Ocean happens within a shorter distance in the summer than in the winter, suggesting a wave of a shorter wavelength in summer than in winter.

Over the course of a year, the northerlies dominate East China over winter and spring. Starting in May, the northerly wind between 105°E and 120°E weakens and is eventually replaced by southerlies in August. In the fall, the weak northerlies return and strengthen in October and November, reaching their peaks in December. This primary northerly wind also encompasses the region as far east as around 140°E, and this west-east spread in part can explain why Japan also experiences the banded precipitation. This climatology is consistent with the findings from Figure 3.10 and Figure 3.11 although it focuses on a range of longitudes instead of searching for the maximum within a region.

The meridional wind over the North Pacific from 140°E eastward also shows a seasonal cycle, albeit in the opposite direction from that over East China(Figure 3.13). In winter, the meridional winds from 140°E to 120°W are predominantly strong southerlies. The southerlies progress westward and weaken to June when weak northerlies appear around 150°E. In other words, the change of direction of the meridional winds between East China and the Pacific Ocean happens within a shorter distance in the summer than in the winter, suggesting a wave of a shorter wavelength in summer than in winter.

3.3.2 The Wavelength of the Rossby Waves and the Jet Stream

The annual cycle of the meridional winds suggests a wave downstream of the Tibetan Plateau, with wavelengths that shorten from winter to summer. To estimate the wavelength for each time slice, we proceed eastward from 75°E and mark the longitudes of the local maxima and minima of the meridional wind. We define the wavelength as the distance between the first two minima(strongest northerlies). If the second minimum is beyond the domain(120°W), we define the wavelength as double the distance between the first minimum and the first maximum. If multiple waves are present, we use the average of the wavelengths as the wavelength of this particular time of the year.

The calculated wavelength shows a seasonal cycle in agreement with the aforementioned observation of a shortening wave from winter to summer. At 40°N, the wavelength eastward of 75°E is about 170° in longitude, approximately 14,517 km in January, and less than 50° longitude, approximately 4270 km, in June and reaches its minimum in July(Figure 3.15). These wavelengths are comparable to the topographic Rossby wavelengths estimated from the one-layer quasi-geostrophic model: 16,000 km for U=70 m/s and 6,000 km for U=10 m/s(Figure 3.15). It is also clear from Figure 3.15 that a shorter wavelength is associated with weaker northerlies in East China immediately downwind of the Tibetan Plateau.

A scatter plot(Figure 3.14) shows the relationship between the upstream speed of the zonal wind and the wavelength estimated from the meridional velocities. The upstream 500 hPa zonal wind is averaged between 60°E to 75°E and 36°N to 46°N. To lowest order, a fast westerly wind upstream of the Tibetan Plateau corresponds to a long wave downstream. The four colors correspond to the four different seasons: in summer(red), the zonal wind is slow and sometimes even an easterly; the downstream wavelength is around 50° in longitude. In winter(blue), the zonal wind is the strongest among the four seasons, and the downstream wavelength can reach beyond 160° in longitude. The two shoulder seasons are in the middle both in terms of the upstream wind speed and the downstream wavelength.

Figure 3.15 compares the annual cycle of the speed of the westerlies up-

stream of the Tibetan Plateau, upstream jet latitude, the downstream wavelength, and the downstream meridional wind from the reanalysis. The latitude range of the Tibetan Plateau(28°N to 38°N) is marked in both the second panel and the fourth panel in Figure 3.15 in dashed lines. Both the speed of the upstream westerlies and the downstream wavelength undergoes a smooth decrease from winter to summer. The relationship found in the reanalysis data is consistent with the one-layer quasi-geostrophic model, that the characteristics of the topographic Rossby wave vary with the upstream U impinging on the topography.

At 90°E, the longitude of the Tibetan Plateau, the jet stream is south of the Plateau(<28°N) in winter and north of the Plateau(>38°N) in August. At 75°E, upstream of the Tibetan Plateau, however, the core of the upstream jet stays around 30°N from December to April and only starts moving north in April. The upstream jet moves past the northern boundary of the Tibetan Plateau in mid-June and continues northward until August; then it retreats southward again. The jet core therefore only encounters the Tibetan Plateau from April to mid-June. As the jet comprises westerlies that are broader than the jet core, the westerlies impinging on the Tibetan Plateau have a different latitudinal profile than the jet core. It is the summer weakening of the westerlies between 28°N to 38°N that contribute to the shortening of the Rossby waves downstream. When the upstream zonal wind reaches its annual minimum around May, the downstream wavelengths also decrease to its annual minimum.

3.3.3 Interannual Variations

A comparison of interannual variations of the upstream 500-hPa zonal wind speed and the downstream wavelength departures from their respective climatology explores topographic Rossby wavelengths, and hence northerlies in East China could be estimated from upstream winds(Figure 3.16). In the summers when the upstream zonal wind is anomalously weak(below 42 m/s), the downstream wavelengths are particularly short, for example as around August 1989 and 2001. In some winters when the upstream wind speed is faster than normal, the downstream wavelengths are also longer than normal, as in March 2010 to 2012. While the co-variations are suggestive, the relation

on interannual time scales cannot be established with statistical significance as other causes, such as variations in the North Pacific high-pressure system, are likely to play a role.

3.3.4 Conclusion

In this study, we hypothesize that the westerlies impinging on the Tibetan Plateau excite topographic Rossby waves; part of these Rossby waves, the northerly flow immediately downstream of the Plateau, govern the northward migration of the rainbands of East Asia. Our analysis of historical wind fields(1979-2018) confirms that wavelengths estimated from longitudinal oscillations of the meridional wind are consistent with those of topographic Rossby waves calculated using the one-layer quasi-geostrophic model(Chapter 3.2). In particular, faster westerlies impinging on the Tibetan Plateau in winter excite Rossby waves with longer wavelengths and stronger northerlies in East China, immediately downstream of topography. We note the central parameter for determining the topographic Rossby wavelength is the speed of the impinging westerlies and not the latitude or strength of the jet core, even the two are related.

The wavelengths of the Rossby waves and associated northerlies can now be linked to the number of occurrences of the rainbands we detected in Chapter 2. Figure 3.17 suggests that rainbands are more frequent in years with faster upstream zonal wind and a longer Rossby wavelength. In 1998, for example, long waves(dark green) penetrated further into spring and summer, resulting in the most number of rainbands in these 40 years; similar events happened in 2011. Anomalously low years in occurrences of rainbands are 1986 and 2007, and their accompanying wavelengths are short(yellow). By taking a two-step connection we have established the link from the rainbands to the northerly winds, and from the northerly wind to the upstream westerly zonal wind. While the association is not statistically significant, the result suggests that upstream westerlies and the topographic Rossby waves may contribute to the frequency of rainbands in East China. Future work involves establishing statistical relationships between the wavelength, the northerlies, and the rainband metrics, while taking into considerations that other factors,

including the moisture supply, could influence the relationship between the Rossby waves and the rainband.

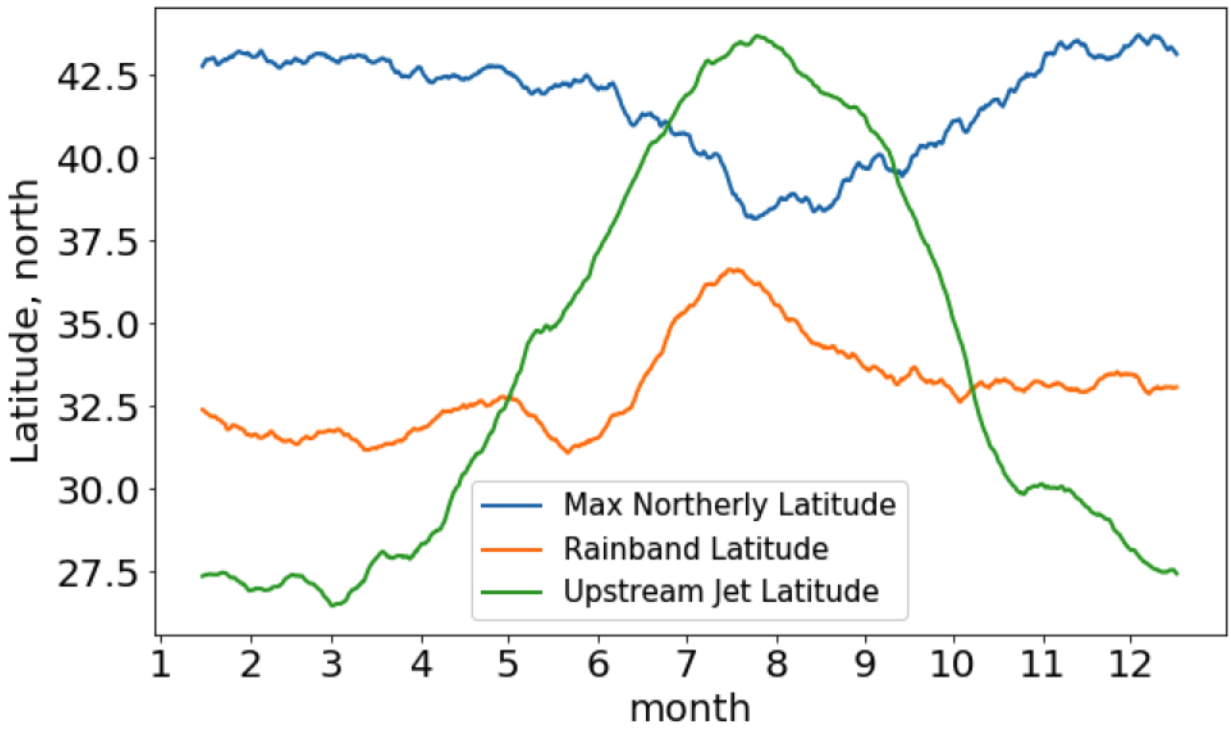


Figure 3.1: The latitude of the maximum northerly wind(blue), the detected rainband(orange), and the jet stream upstream(west) of the Tibetan Plateau(green). The maximum northerly wind stays around 42.5°N in winter and moves south in June, while both the rainband and the upstream jet stream moves north. The rainband starts to move north in June, and the upstream jet stream starts to move north in March. Both the latitude of the rainband and the upstream jet peaks in late July. The jet stream travels a broader range of latitude than both the northerly wind and the rainband do.

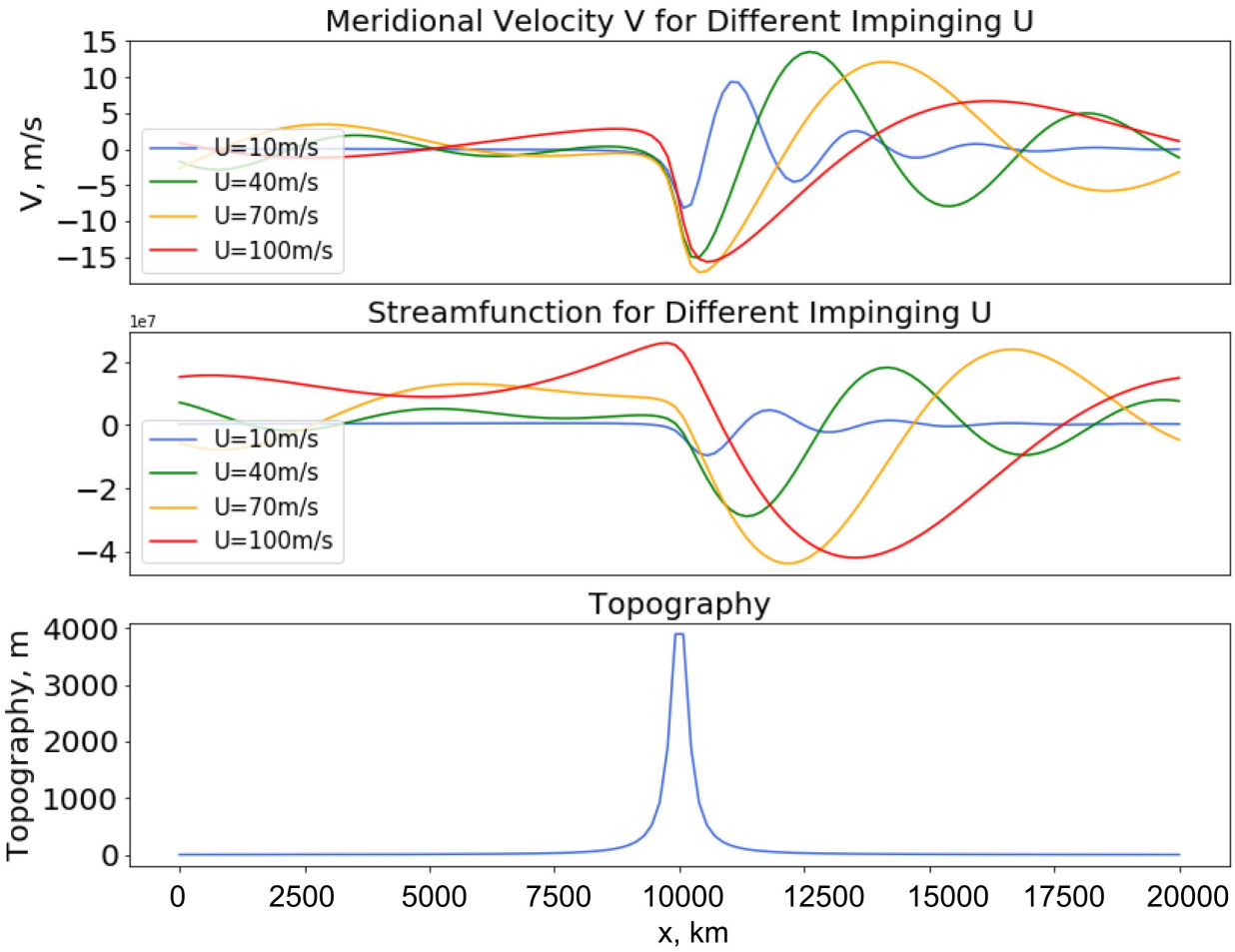


Figure 3.2: The 1-D steady-state solution for a Rossby wave excited by a mountain of 4000 m for different impinging zonal wind. The bottom panel shows the 1-D topography with a peak of 4000 m; the middle panel shows the streamfunction for an impinging wind of different speeds ranging from 10 m/s to 100 m/s. The top panel shows the corresponding meridional wind for the different impinging wind. The faster impinging wind generates a Rossby wave with longer wavelength; the impinging wind of 40 m/s generates the fastest meridional velocity associated with the wave.

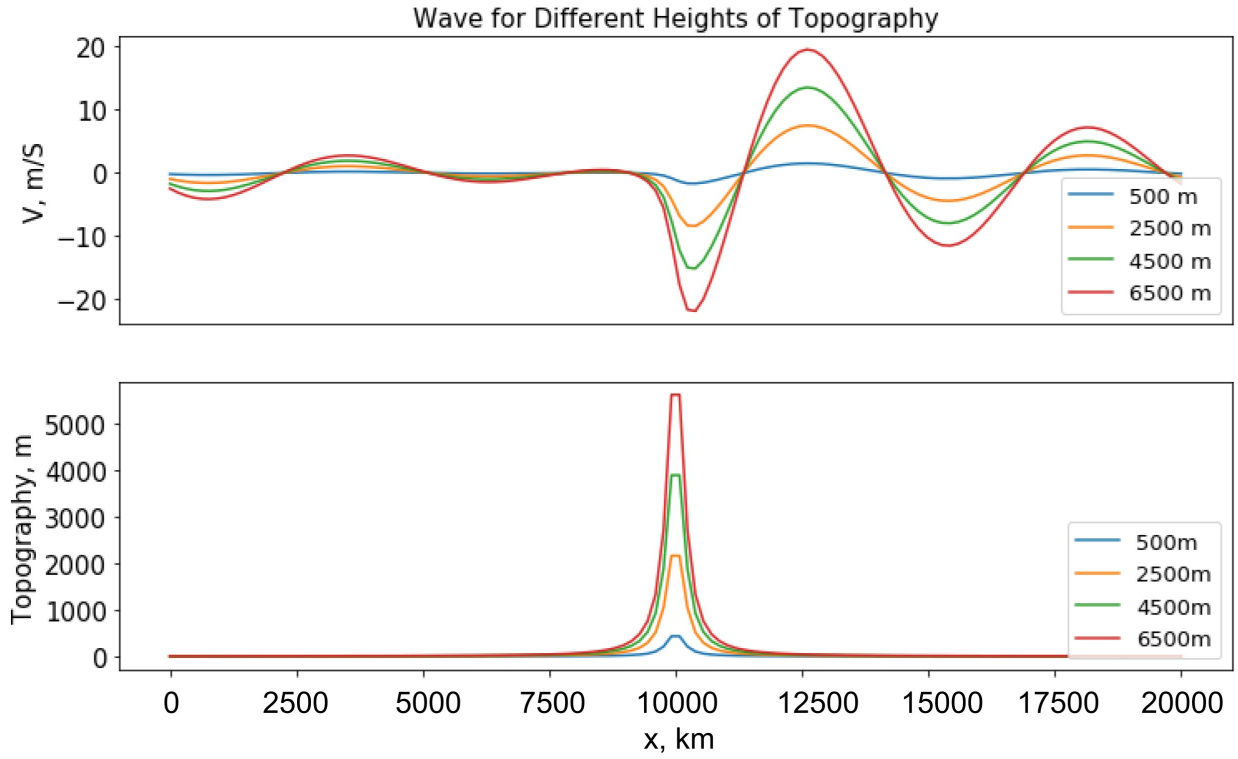


Figure 3.3: The 1-D steady-state solution for a Rossby wave excited by mountains of various heights and an impinging wind of 40 m/s. The mountains have peaks from 500 m to 6500 m(lower panel). The excited Rossby waves have the same wavelength but different magnitude: the higher mountains generate faster meridional winds downstream. The meridional wind first appears as a northerly wind(negative) to the right side of the mountain.

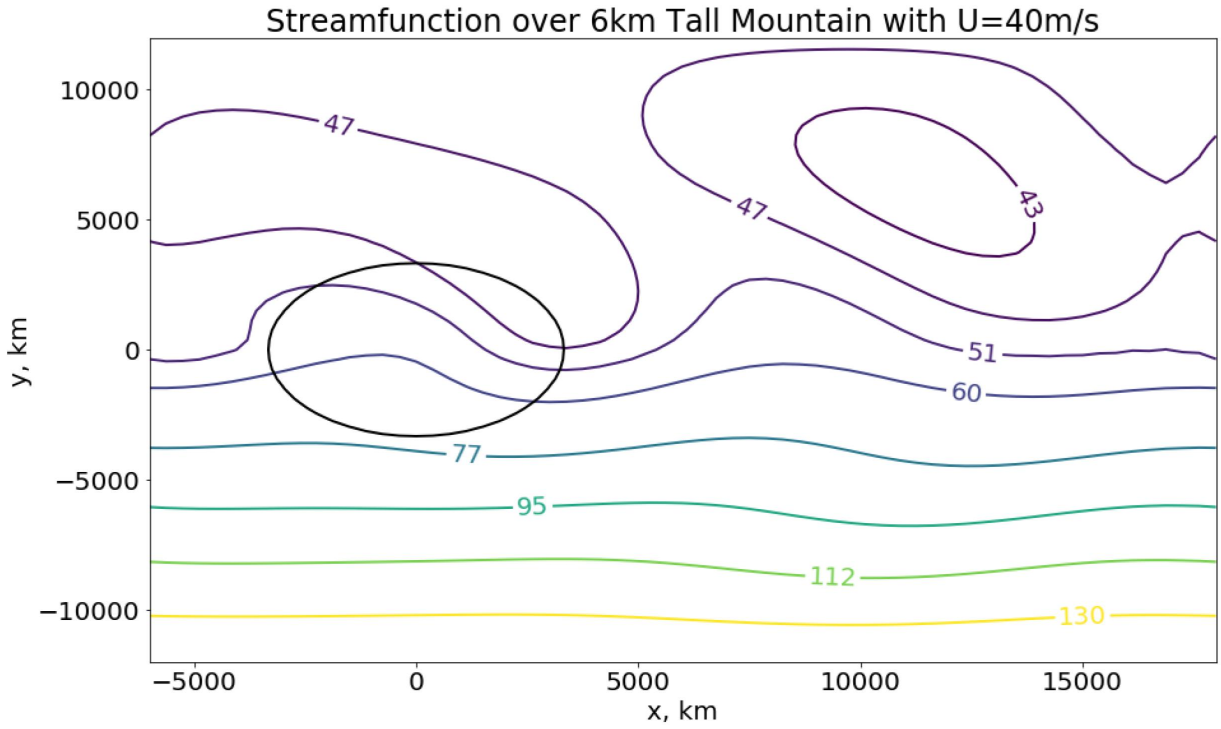


Figure 3.4: The 2-D solution to the one-layer quasi-geostrophic model of potential vorticity. The mountain is circular and has a peak of 6000 m(black contour). The colored contour shows the streamfunction of the excited Rossby wave(1×10^7). The northerly part of the Rossby wave appears immediately to the right of the mountain; the flow south of the mountain is largely zonal.

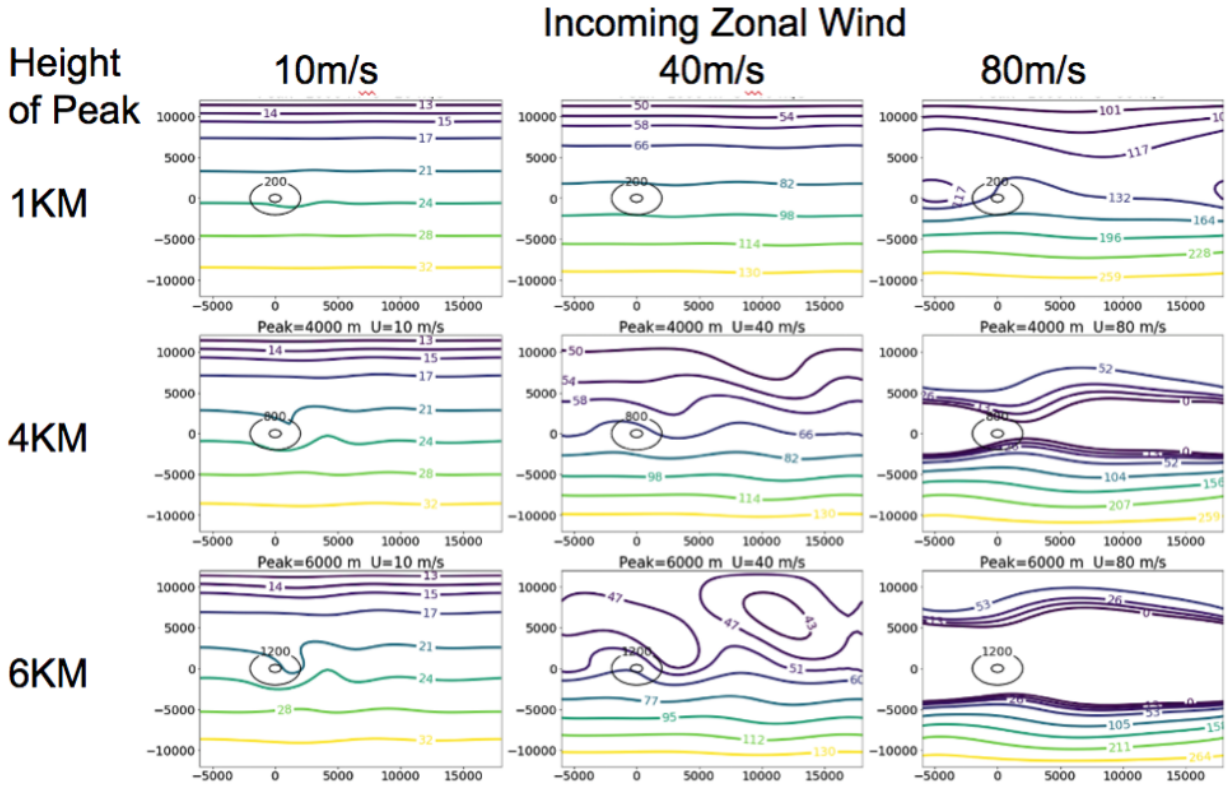


Figure 3.5: The 2-D solution to the one-layer quasi-geostrophic model of potential vorticity. The three rows show circular mountains with peaks of 1 km, 4 km, and 6 km. The three columns represent uniform impinging wind of 10 m/s, 40 m/s, and 80 m/s respectively. The colored contour shows the streamfunction of the excited Rossby wave(1×10^7). A slow impinging wind of 10 m/s and a short mountain of 1 km excite minimal wave; the wave grows bigger when a fast zonal wind(40 m/s or 80 m/s) impinges on a tall mountain of 4 km or 6 km.

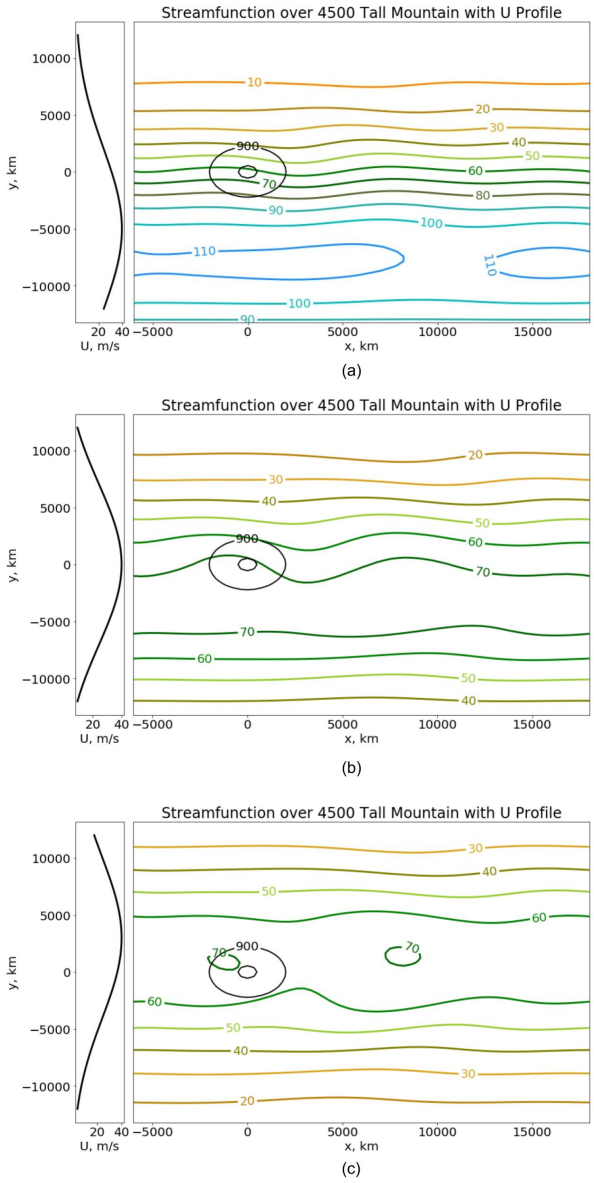


Figure 3.6: Streamfuncions for the Rossby waves by zonal winds with different wind profiles impinging on a circular mountain. The mountain has a peak of 4500 m, similar to the Tibetan Plateau. The zonal wind profiles have a maximum of 40 m/s with Gaussian profiles. (a)The peaks of the zonal wind profiles are south of the mountain, and the excited Rossby wave is minimal. (b)The peak zonal wind is aligned with the mountain, the Rossby wave is maximal with a northerly component immediately to the right of the mountain. (c)The peak wind is north of the mountain. The wind profiles mimic the zonal jet stream that moves northward from spring to summer.

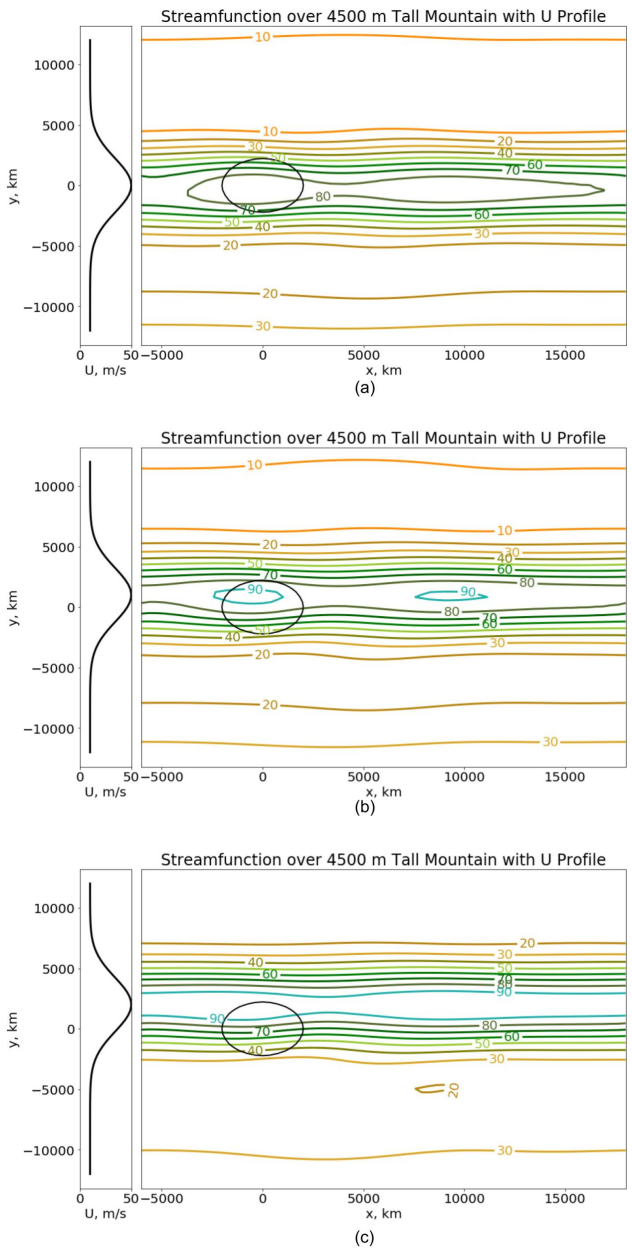


Figure 3.7: Streamfuncions for the Rossby waves by zonal wind with different wind profiles impinging on a circular mountain. The mountain has a peak of 4500 m, similar to the average height of the Tibetan Plateau. The zonal wind profiles have a maximum of 50 m/s and have Gaussian profiles narrower than the ones in Figure 3.6. When the maximum of the wind aligns with the latitude of the mountain, the Rossby wave is maximal(top panel), with a northerly component immediately to the right of the mountain.

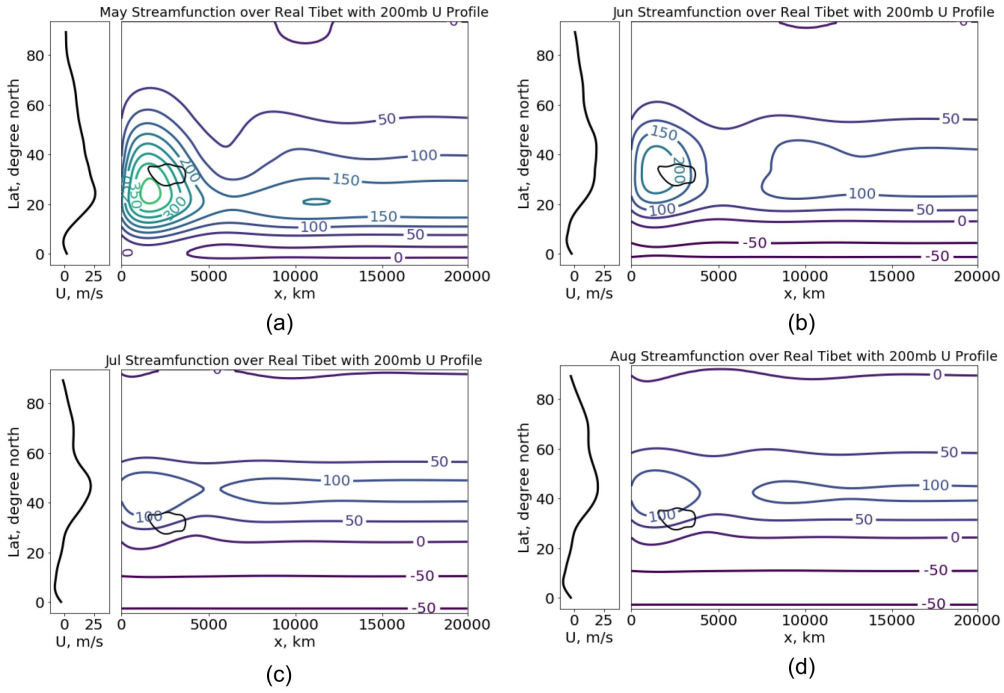


Figure 3.8: Streamfunctions for the Rossby waves excited by the true zonal wind profiles and the real topography of the Tibetan Plateau from May to August. The left panel of each subplot shows the climatology(1979-2018) of the averaged zonal wind averaged from 60°E to 70° on the 200-hPa surface. The right panel of each subplot shows the topography of the Tibetan Plateau(black contour) and the streamfunction(colored contour). The most prominent Rossby wave happens in May with the impinging zonal wind aligned with the latitude of the Tibetan Plateau. In June, the latitude of the peak zonal wind and the topography still align, but the zonal wind is weak and has a less sharp peak than in May. In July and August, the peak of the zonal wind is north of the plateau, and the excited Rossby wave is minimal.

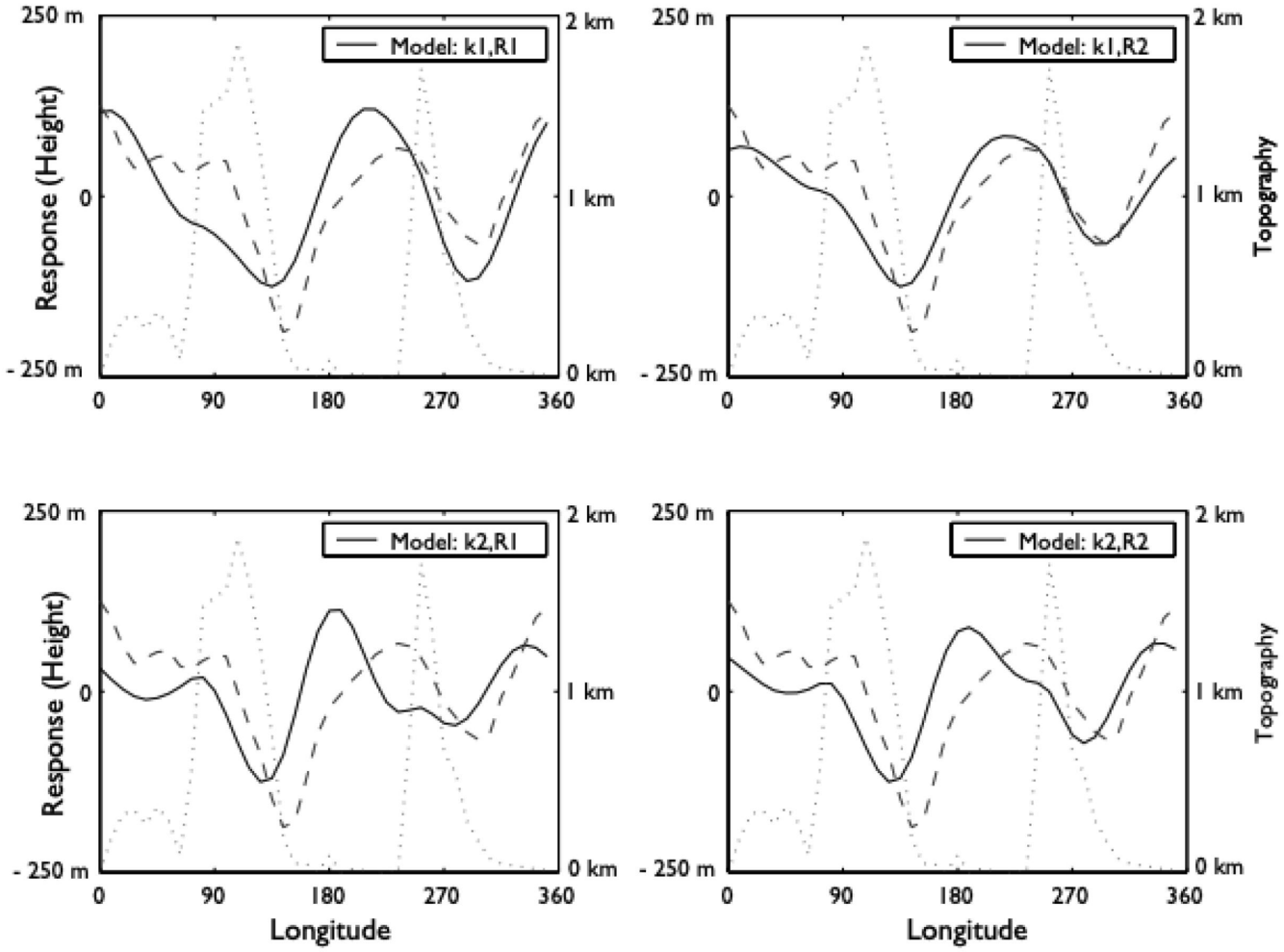


Figure 3.9: Fig. 13.2 from Vallis, 2017. Solutions of the Charney-Eliassen model. The solid lines are the steady solution using the Earth's topography at 45°N with two values of friction(R1 $\approx$ 6 days, R2 $\approx$ 3 days) and two values of resonant zonal wavenumber(2.5 for k1, 3.5 for k2), corresponding to zonal winds of approximately 17 and 13 ms^{-1}. The solutions are given in terms of height, η', where $\eta' = f_0\psi'/g$, with the scale on the left of each panel. The dashed line in each panel is the observed average height field at 500 mb at 45°N in January. The dotted line is the topography used in the calculations, with the scale on the right of each panel.

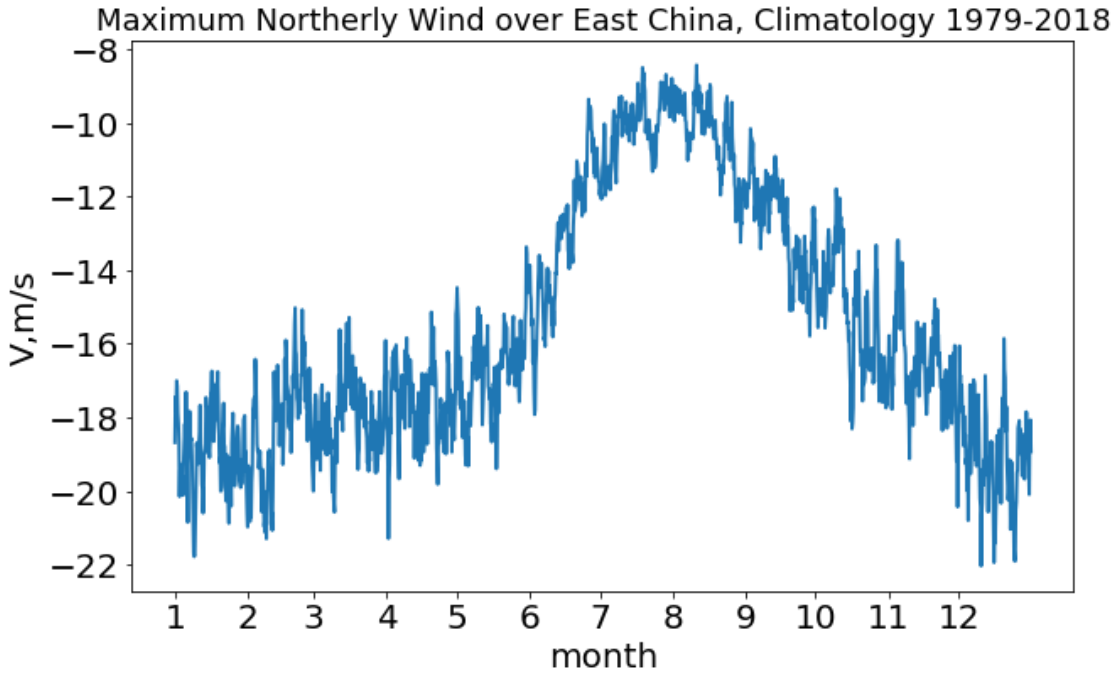


Figure 3.10: The climatology of the speed of the maximum northerly wind over East China at 500 hPa. East China is defined as 110°E to 120°E and 20°N to 50°N. The maximum northerly in this domain is sampled every 6 hours from 1979 to 2018. The northerly wind is the strongest in winter, reaching -22 m/s(negative indicates the northerly direction). The wind speed slowly decreases in spring and starts to drastically decrease in May, until it reaches its minimum around -10 m/s in August. In the fall, the northerly wind strengthens again.

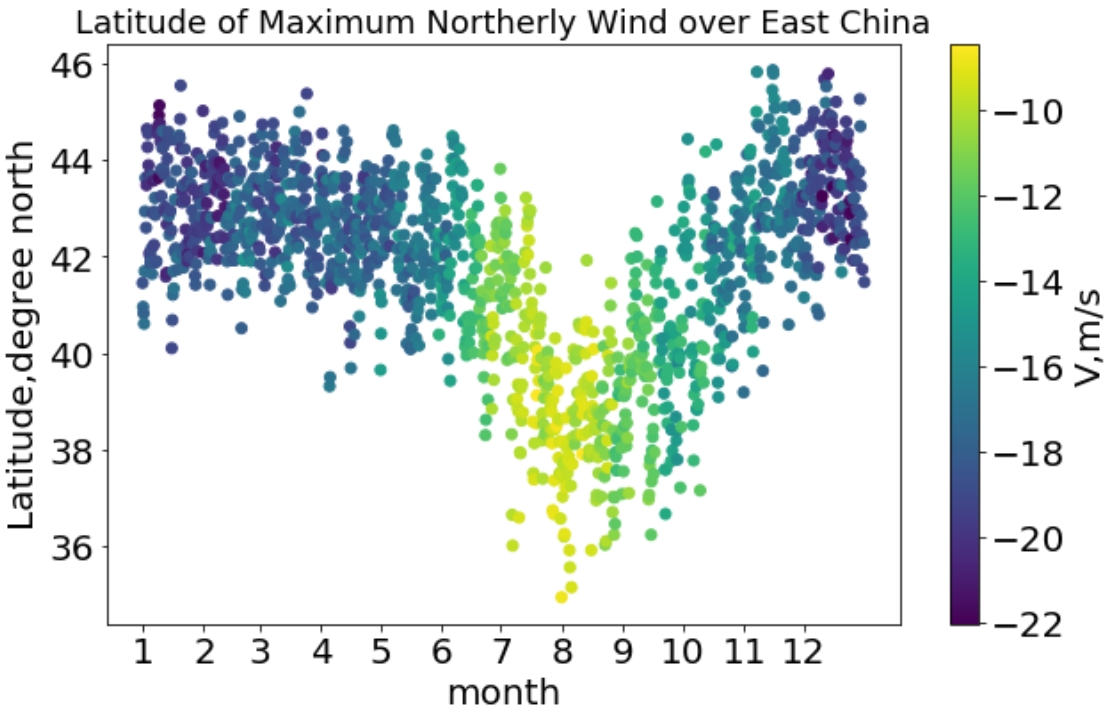


Figure 3.11: The climatology of the latitude and the speed of the maximum northerly wind over East China at 500 hPa. East China is defined as 110°E to 120°E and 20°N to 50°N. The maximum northerly in this domain is sampled every 6 hours from 1979 to 2018. The northerly wind is the strongest and north at 45°N in winter. The wind speed slowly decreases and moves south in spring. The northerly starts to drastically move south and weaken in May until it reaches its minimum around -10 m/s at 36 ° in August. In the fall, the northerly wind strengthens and moves north again.

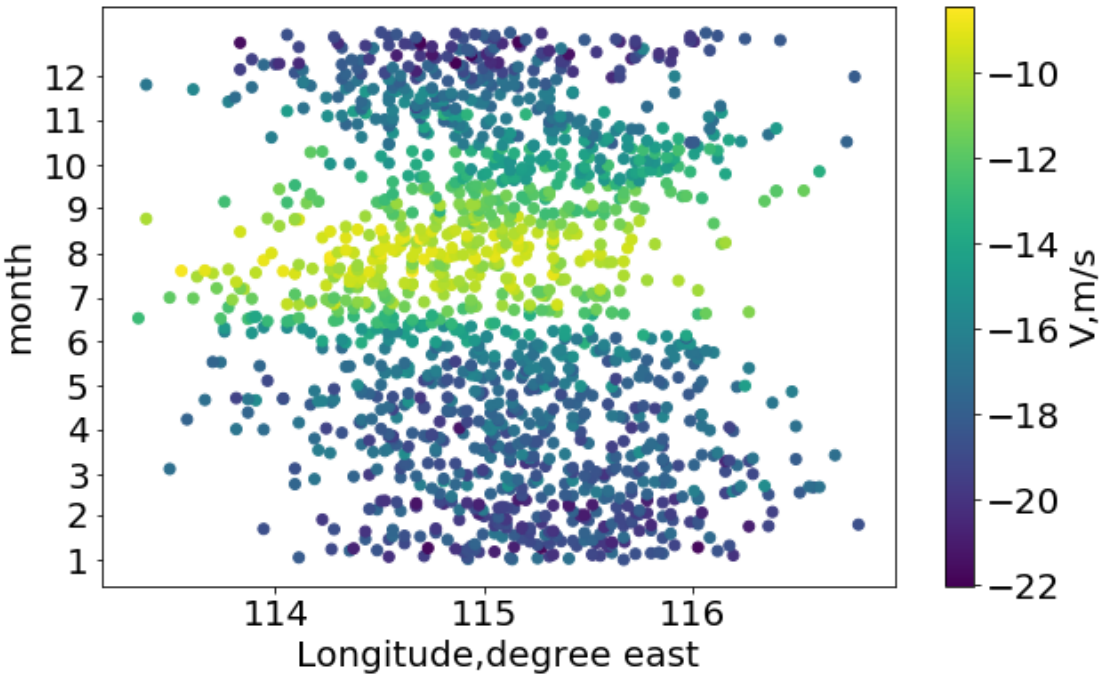


Figure 3.12: The climatology of the longitude and the speed of the maximum northerly wind over East China at 500 hPa. East China is defined as 110°E to 120°E and 20°N to 50°N. The maximum northerly shows a seasonal cycle of a small amplitude of 2° in longitude. The northerly wind is more to the east in winter at 116° than in the summer at 114°.

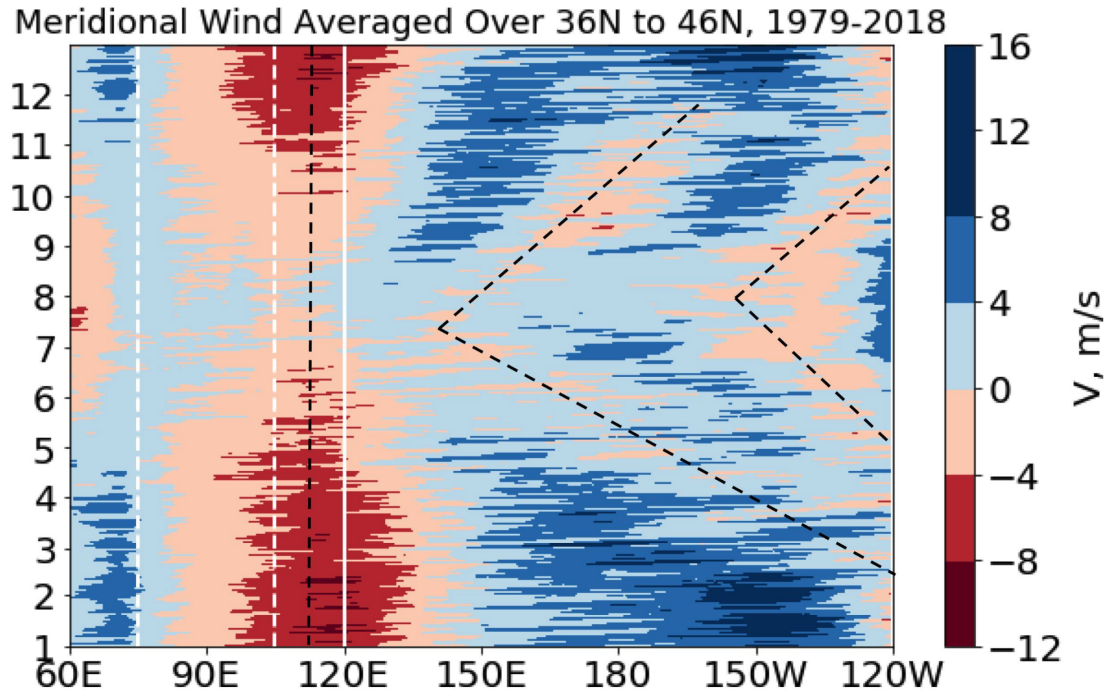


Figure 3.13: The climatology of the meridional wind(V) averaged over 36°N to 46°N. The three black dashed lines mark the first, the second, and the third northerly, respectively from left to right. The white dashed lines mark the western and eastern boundaries of the Tibetan Plateau at 75°E and 105°E, respectively. The solid white line marks the longitude of the east coast of China at 120E. Over East China, the northerly wind dominates from winter to spring and only becomes weak in the summer. Downstream(east) of the Tibetan Plateau, the meridional wind switches sign(from red to blue and the opposite) after a longer distance in the winter than it does in the summer. The secondary and the third northerly winds do not appear in winter.

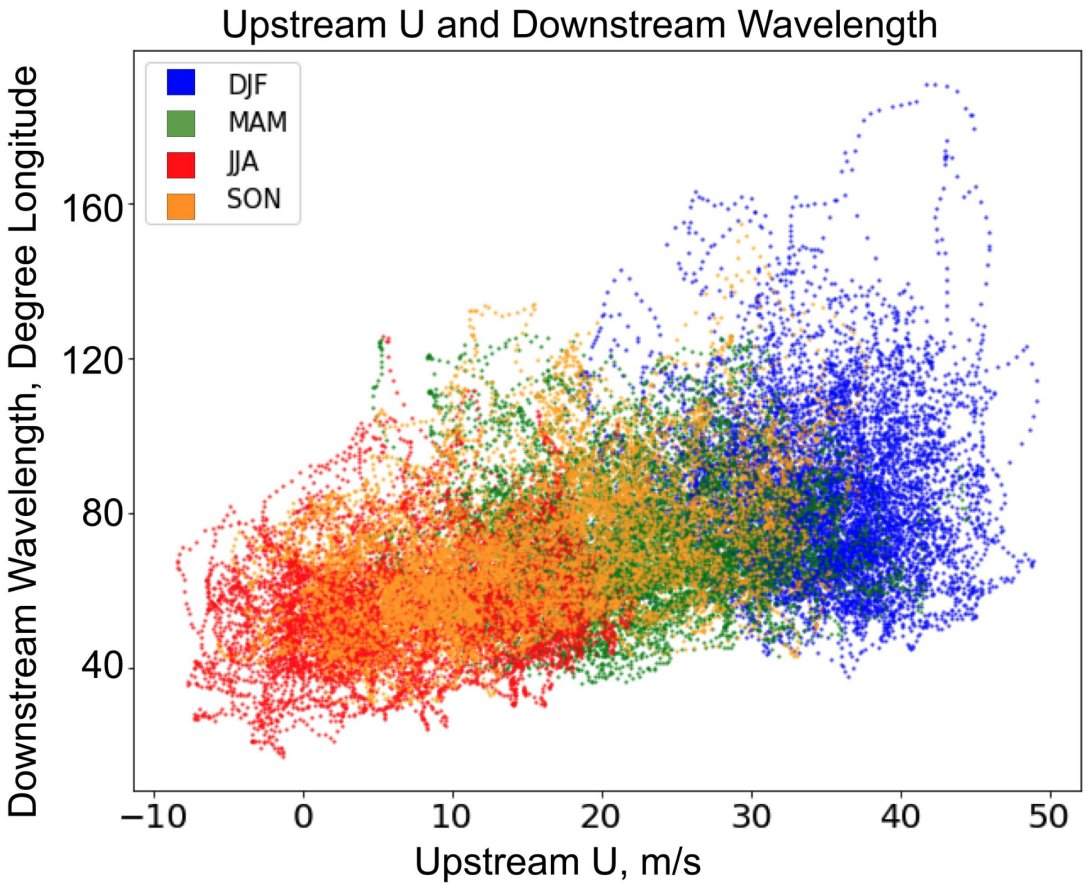


Figure 3.14: The scatter plot of the upstream zonal wind at 500 hPa averaged between 60°E to 75°E and 36°N to 46°N and the downstream wavelength calculated by the switching of the meridional wind directions. Each dot represents a 6-hour snapshot of the data in the period of 1979 to 2018. The red dots are in summer(June, July, and August); the green dots are in spring(March, April, and May); the orange dots are in fall(September, October, and November); the blue dots are in winter(December, January, and February). In general, longer upstream zonal wind corresponds to a longer wavelength downstream. The U and wavelength are the strongest in winter and the weakest in summer.

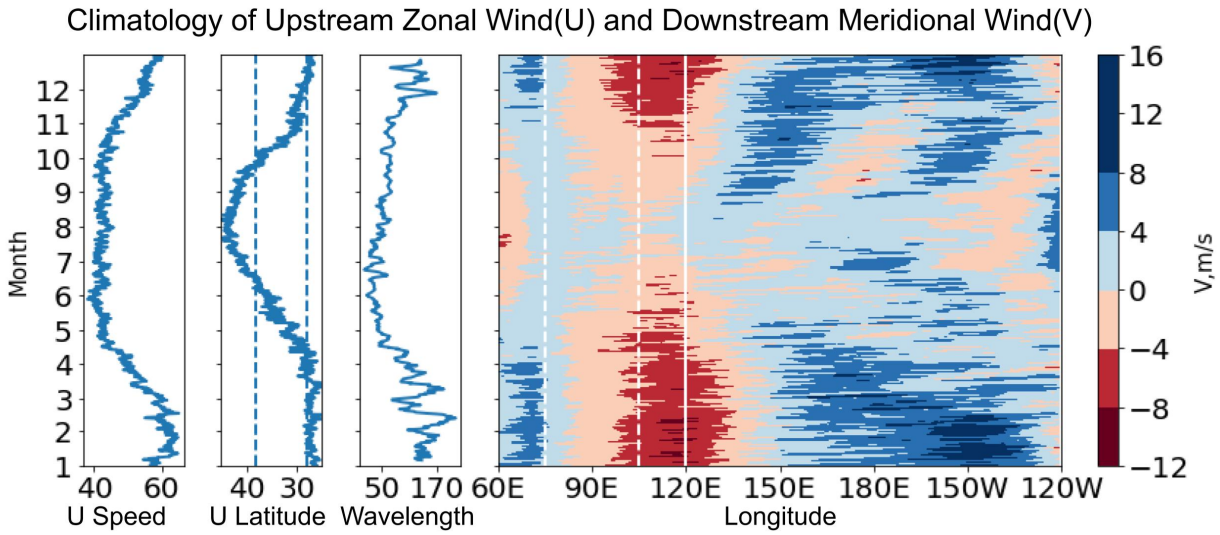


Figure 3.15: The climatology of the upstream zonal wind(U) and downstream meridional wind(V) of the Tibetan Plateau. The left two panels describe the zonal wind at 500 hPa averaged between 60°E to 75°E. The first panel is the maximum speed of this zonal wind; the second panel is the latitude where this maximum speed occurs. The right two panels describe the meridional wind downstream of the Tibetan Plateau averaged between 36°N to 46°N. The third panel is the downstream wavelength to the east of the Tibetan Plateau; the fourth panel is the meridional wind. The upstream zonal wind and the downstream meridional wind go through a similar seasonal cycle. The U is the strongest and at the lowest latitude in winter, and the wavelength is the longest in winter.

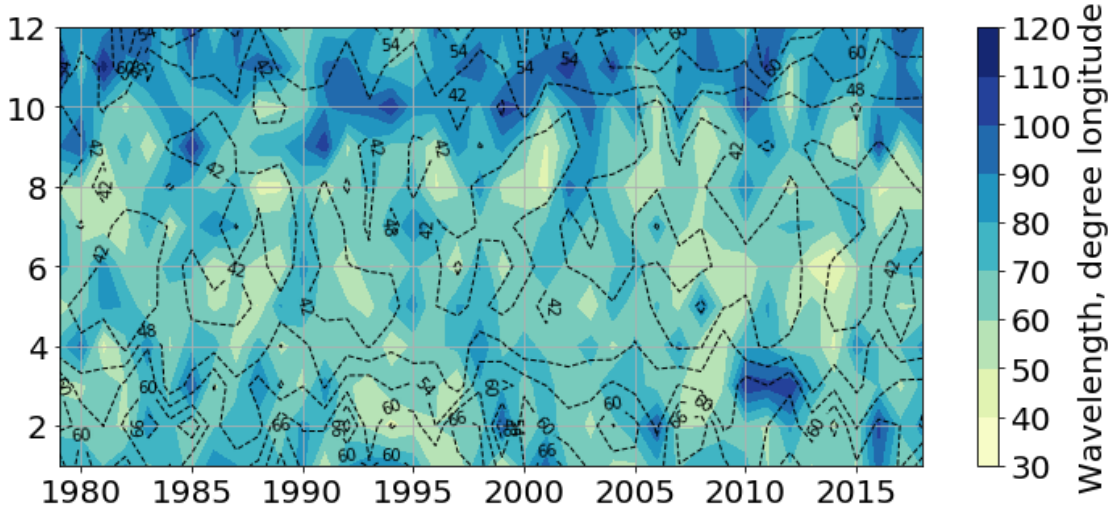


Figure 3.16: Comparison of the upstream zonal wind speed averaged over 60°E to 75°E in dashed contour and downstream wavelengths in the colored contour. Both the upstream zonal wind and downstream wavelengths are monthly from 1979 to 2018. Some exceptionally low years in the downstream wavelength correspond to the weak upstream zonal wind, for example in 2001 and 2005.

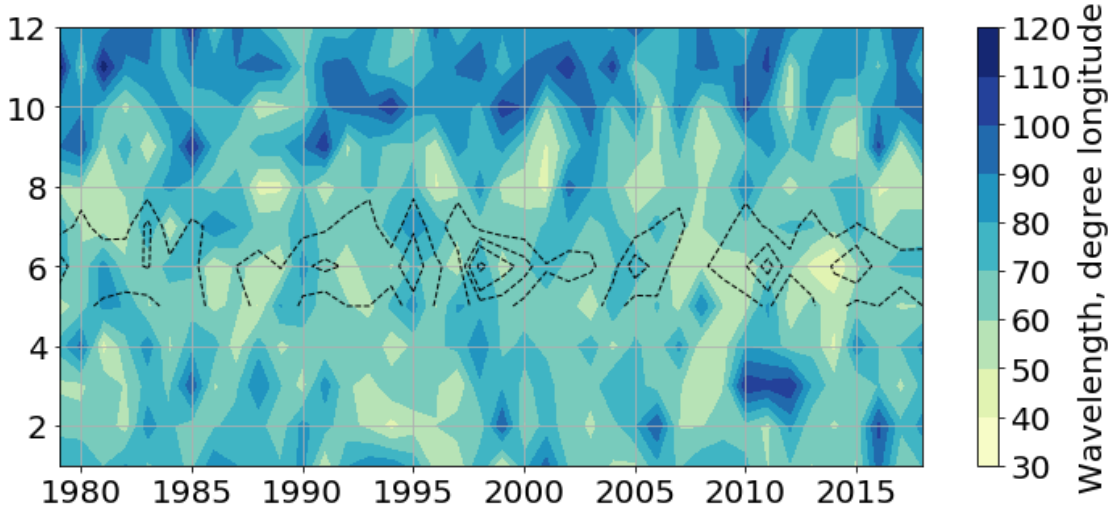


Figure 3.17: Comparison of the number of occurrences of the East Asian rainbands in dashed contour and downstream wavelength in the colored contour. Both the rainband and downstream wavelengths are monthly from 1979 to 2018. The high-occurrence year of the rainband usually corresponds to long wavelengths in spring and summer, for example, in 1995, 1998, and 2011.

Chapter 4

A Characterization of the Jet Streams in East Asia

4.1 Introduction

The East Asian rainband is a signature of the climate in China, Japan, and Korea from May to August and can have a zonal scale of as much as 2,000 km. The rainband is frontal precipitation and has its origin in the large-scale dynamics, as analyzed in the previous chapters. Because of the unique seasonality and northward migration of this precipitation, the East Asian rainband is often associated with the jet stream by previous studies(e.g. Yeh et al., 1959, Chiang et al., 2015a). In Chapter 2 we detect the individual events of the East Asian rainband and closely examine their characteristics and their accompanying atmospheric circulation. We conclude that mid-tropospheric northerly winds over East China are a crucial component for the formation of the rainbands. In Chapter 3 we use a one-layer quasi-geostrophic model to demonstrate that the crucial northerly wind is part of the stationary Rossby waves excited by topography(the Tibetan Plateau); the resulting meridional winds from the model are comparable to the realistic winds in reanalysis. With a fixed shape and height of the topography, a strong westerly zonal wind impinging the topography is the most important factor in generating the crucial northerly wind downstream.

At the heart of this zonal flow is the jet stream. Previous studies have long speculated on the relationship between the jet stream and East Asian climate, mostly because they share the northward movement in spring and

early summer. In Chapters 2 and 3, however, we derive a two-step relationship between the East Asian banded precipitation and the zonal wind upstream of the Tibetan Plateau and find the link between the jet stream and the rainbands to be not the most straightforward. We reach this conclusion by closely examining a variety of aspects of the jet stream. Although a direct link cannot be clearly established, our detailed characterization of the jet stream uses novel methods and shows features of the jet stream that are not well-known. This chapter will focus on this characterization of the jet stream in East Asia because the jet stream is important to weather and climate in East Asia in general, although it might not be the single most useful indicator for the East Asian rainbands.

4.2 An introduction to the Jet Streams

Jet streams are narrow fast-flowing currents of air in the upper troposphere, often near the tropopause. They are one of the most prominent and ubiquitous features in atmospheric circulation. They play essential roles in dynamic processes like synoptic-scale cyclogenesis and atmospheric blocking. Their features, including their locations and strengths, are widely used in weather forecasting and closely tied to regional climates.

Two jet streams circle each hemisphere: the subtropical jet and the polar jet, also referred to as the eddy-driven jet. The subtropical jet resides at the poleward boundary of the Hadley Cell as a result of the angular momentum transport from the deep tropics. The polar jet, on the other hand, is driven by the baroclinic eddies, usually concentrated in the mid-latitudes. The rapid flow from these two sources can combine or diverge, and interact with each other depending on the time of the year and their locations. For example, the subtropical jet appears to be strong over the Pacific, but the eddy-driven jet is not prominent there; between 60°W and 20°E, however, the two jets are evident and well-separated(Lee and Kim, 2003).

Jet streams have large meanders across the globe. The degree of the meanders affects upper-level divergence and is therefore important for frontogenesis. In fact, the waviness of the jet streams affects the occurrence of regional weather extremes in temperature and precipitation(Röthlisberger et

al., 2016). Sustained large-amplitude meanders of the jet streams have been linked to persistent and severe heat waves and droughts(e.g. Brikas et al., 2006; Wang et al., 2016).

Jet streams are typically identified by the monthly mean maximum westerly wind at the 200-hPa or the 250-hPa pressure level. While this approach successfully captures the jet migrating northward and weakening from winter to summer, there is much more to the behavior of the jets. The subtropical and polar jets are not always distinctly separate in the atmosphere. Their locations and meanders vary on a much finer time scale, sometimes daily and hourly. Previous attempts to track the jet streams rely on finding zonal winds that exceed a single threshold(e.g. 30 m/s) in some domains at 200 or 250 hPa(e.g. Namias, 1950; Schiemann et al., 2009). This method captures one maximum of the jet stream but is not designed to disentangle the two or more jet streams and risks mistaking one jet stream for another. In winter, the subtropical jet is usually the faster one and thus usually captured as the maximum; in spring and summer, the eddy-driven jet sometimes exceeds the subtropical jet in speed and is thus identified as the maximum instead. If the latitude and altitude of the maximum of the jet speed are recorded, we might find sudden jumps inconsistent with the actual movements of the jet. This inconsistency could affect our judgment of the seasonality of the jet stream.

Apart from the zonally symmetric features, the jet stream exhibits especially interesting behavior due to its interaction with large and high topography, including the Tibetan Plateau, the Rocky Mountains, and the Andes. When a zonal jet of sufficient strength encounters the large topography, stationary Rossby waves are excited and continue to the downstream of the mountains; otherwise, the waves are turned back(Bolin, 1950). When the jet stream splits into two branches to circumvent a mountain, it becomes faster once it passes the mountain and the two branches join each other(Namias and Clapp, 1949). This local maximum of the jet speed downstream of the Tibetan Plateau, together with a zonally asymmetric diabetic heating collocated with the local jet core, shapes the low-level flow that brings in the moisture from the South China Sea and fuels the East Asian summer monsoon(Molnar et al., 2010). It has also been suggested that, in the summer, the jet stream advects heat from the eastern flank of the Tibetan Plateau and helps to lift air in the mid-troposphere over China, thus creating a band

of precipitation(Sampe and Xie, 2010).

In the region around the Tibetan Plateau, both the zonal and the meridional components of the jet stream play important roles for the local climate. The latitudinal position of the zonal jet relative to the Tibetan Plateau affects the phase of the East Asian summer monsoon downstream, as shown in Yeh et al. (1959). In agreement with paleoclimate records, the timing of the zonal jet stream migration from the south of the plateau to the north of the plateau controls the sharp transition from the spring regime to the Meiyu regime of rainfall over Eastern China(Chiang et al., 2015b).

As the jet stream has its maximum speed aligned with the latitudinal range of the Tibetan Plateau in spring, the meridional component of the jet becomes prominent. The northerly winds to the east of the Plateau are essential in creating the front, together with the moisture transport from the south; the retreat of the northerlies marks the demise of the Meiyu rainfall(Kong and Chiang, 2020). The timing of the transition is within days, and the length of the Meiyu season contributes significantly to the interannual variability of the precipitation. The latitudinal position of the jet stream is also correlated with the altitude of the jet core in different seasons(Rikus, 2018). The behaviors of the jet stream in this region, therefore, deserve more detailed documentation than monthly means.

In this chapter, we focus on the jet streams in the East Asian region around the Tibetan Plateau, where the jet stream interacts with the highest topography on earth. In Chapter 4.3, we introduce a novel method to identify the jet stream, including its multiple branches, both in the 2-D and 3-D space on the 6-hourly timescale. In Chapter 4.4, we describe the seasonality of the zonal wind over East Asia and track the jet streams accordingly. We identify the subtropical jet and the eddy-driven jet and present the climatology of their speed, latitude, and altitude, respectively, in both 2-D and 3-D. We track the two jets not only by their physical location but also by their dynamic sources. We also identify the number of maxima in the jet streams to capture the seasonal phenomenon of multiple branches of jet near the latitudinal range of the Tibetan Plateau. Finally, we present the northerly component of the jet stream and relate it back to the East Asian rainband discussed in previous chapters.

Our study aims to bridge the gap between the actual jet streams in the

atmosphere and the previously documented single maximum in zonal wind referred to as the jet stream. We attempt to complete the picture of the northward migration of the jet streams in East Asia by identifying the behavior of each jet and to avoid mistaking a polar jet as a migrated subtropical jet. Our methods to capture the jet streams are valuable for other locations of interest as well, and our results provide a solid basis for studies that make connections between the jet stream and other features of the East Asian climate.

4.3 Data and Method

4.3.1 Data

This work uses ERA-interim(Dee et al., 2011), a reanalysis dataset that is the optimal fit between historical observations with forecasts from the advanced numerical weather forecast model of the European Center for Medium Range Forecasting to yield global distributions of the atmospheric circulation. We use the data in ERA-Interim from the past 40 years, from 1979 to 2018 at a 6-hourly temporal, 0.75° spatial resolution(approximately 80 km, with T255 spectral), and 26 pressure levels.

4.3.2 Method to Track the Jet Stream

We present two automated tracking algorithms to identify features of the jet stream in a domain in East Asia, chosen to span 0°N to 90°N in latitude and 60°E to 160°E degree in longitude. The tracking is done at every 6-hourly time step with the ERA-interim dataset from 1979 to 2018(40 years). The first method captures the fine 2-D characteristics of the jet stream on the 200-hPa surface; the second method reveals the vertical structures of the jet stream in the 3-D space.

4.3.2.1 The Distribution of the Wind Speeds on 200-hPa Surface

Previous work usually defines the jet stream as a westerly wind faster than 30 m/s at the 200-hPa or 250-hPa surface(e.g. Koch et al., 2006; Schiemann

et al., 2009). Across seasons, however, the jet stream changes its speed and therefore a constant 30 m/s might not always work to distinguish this current from the background wind.

Here we examine the distribution of the wind speed over East Asia, the domain of our focus, on the 200-hPa surface near the tropopause. Figure 4.1 shows the histogram of the monthly mean wind speed $\sqrt{U^2 + V^2}$ from 1979-2018 on the 200-hPa surface at each grid box within the East Asian domain(0° to 90°N, 60°E to 160°E). During the winter, the fastest wind easily exceeds 100 m/s, whereas in summer it is capped at 50 m/s. Another pronounced characteristic is that the peak of the distribution lies to the very left, close to 0 m/s during the winter, and shifts to around 10 m/s during the summer. That is to say, during the winter, the fast wind, presumably the jet streams, stands out from a background of weak winds, while during the summer the weaker jet stream is less distinguishable from a stronger background, and the wind around 10 m/s is dominant.

Knowing the distribution of the wind speed in our chosen domain, we closely examine our choice of the cut-off for identifying the jet stream. Figure 4.2 shows the cumulative distribution function of the wind speed for each month within the East Asian domain on the 200-hPa surface. The summer months are shown in warm colors, and the winter months are shown in cold colors. We find that a wind of 30 m/s, a commonly used threshold for jet detection(Schiemann et al., 2009), is faster than 92% of the winds in our chosen field in July, but is only faster than approximately 60% of the winds in December.

To consider the choice of the cut-off wind speed for the jet stream, therefore, we need to take into account the seasonal difference in the distribution of the wind speed. For this study, we want to investigate the seasonal migration of the jet streams and their relative positions to the Tibetan Plateau in all seasons. For this purpose, we need a lenient threshold on the wind speed so that we do not miss the jet streams in summer even if they are weak. We therefore choose the 20 m/s as a threshold for the tracking of the jet streams, as this speed represents the 60^{th} percentile of the wind speed in summer. The 30 m/s threshold adopted by previous work can successfully capture the wind stronger than 60% of the winds in winter but will miss the majority of the winds in summer.

A threshold for the wind speed at 20 m/s will only serve as an initial criterion in the jet tracking; the local maxima of wind speed will then be located as the jet core. We experiment with the threshold at 30 m/s and 20 m/s respectively and find the tracking results of the jet core to be exactly the same, except for the cases in spring and summer when the wind maxima drop below 30 m/s; in those cases, a threshold at 30 m/s will completely miss these maxima and create a discontinuity in an otherwise smooth seasonal migration of the jet core. We have also tested using the 60^{th} percentile wind in each month as the threshold and found similar results for the identified jet streams. For simplicity, we use the 20 m/s as the lower bound for the jet stream throughout this work.

4.3.2.2 Tracking the Jet Stream on the 2-D Plane

For the first method of detection in the 2-D plane, we choose the wind field (U, V) at the 200-hPa pressure level over East Asia. The first step selects all the grid points with absolute wind speeds faster than 20 m/s($\sqrt{U^2 + V^2} \geq$ 20 m/s) and with a westerly wind component($U > 0$)(Figure 4.3). We test different thresholds as lower bounds for the wind speed to be considered a jet stream and find that any threshold from 20 m/s to 40 m/s preserves the same general structure of the jet stream. A threshold lower than 20 m/s will include the majority of the domain; a threshold higher than 40 m/s will lose the grand shape of a continuous jet stream and only leave disjoint patches. We choose the 20 m/s in order to catch the jet streams in summer when winds are weak in general.

The second step finds the connected components in the chosen wind field, in which each grid point has a speed $>$ 20 m/s and a westerly component. We utilize the technique of connected-component labeling, which has been applied to the identification of atmospheric rivers in climate models(Byna et al., 2011). Contiguous grid points are defined such as each grid point touches at least one other grid point in the same group on its side, or namely, "4-connectivity" as the term in image processing. The contiguous grid points are grouped, and each point in a group is given a label unique to the group. We do not consider a grid point part of a group if only a corner of this grid touches the other members(known as "8-connectivity"). We choose this

option of 4-connectivity to ensure that we pick up realistic continuous flows in the atmosphere and eliminate noise adjacent. Also, this choice proves to be optimal in accommodating the algorithm to gather the data for the splitting of the jet stream, which we will discuss further in Chapter 4.4.3.

We next rank the labeled groups by their sizes, or namely, the number of the connected grid points in each group. We remove the patches that are smaller than 10°x10° in size. These small patches might be falsely counted as splits of the jet stream in the next steps if not removed. The remaining labeled groups are identified as the jet streams.

4.3.2.3 Tracking the Jet Stream in 3-D

Previous studies(e.g. Bolin, 1950; Schiemann et al., 2009) consider only the winds on the 200-hPa surface when identifying the jet stream. The altitude of the core of the jet streams, however, varies at different times of the year as well as at different longitudes and has been documented to be correlated with the latitude of the jet in the monthly data(Rikus, 2018). As a result, simply identifying the jet stream on a 2-D plane may miss or misinterpret important information. For example, if the core of the jet stream changes its height from 200 hPa to higher or lower without a change in its speed, the jet stream on the fixed 2-D plane will seem weakened. The structure of the jet stream in 3-D, therefore, needs to be understood and documented before any variability of the jet is attempted.

The climatology of the zonal wind already shows interesting signatures in the vertical dimension. Figure 4.5 shows latitude-pressure cross-sections of the zonal wind at four different longitudes: 75°E(west of the Tibetan Plateau), 95°E(on top of the Tibetan Plateau), 110°E(East China), and 140°E(Japan). In January, the jet stream is at its max at 25°N on the 200-hPa surface at 75°E, but the 30 m/s contour expands both northwards to 40°N and downward to the 400-hPa surface. Downstream of the Tibetan Plateau at 140°E, the 30 m/s contour reaches further down to 600 hPa. In April, the zonal wind weakens, but the general shape of the 10 m/s contour holds the same for all longitudes. The wind maximum migrates north and is directly on top of the Tibetan Plateau, as shown in the 90°E cross-section. In July, the zonal wind is significantly weaker and its contour shrinks in the vertical

direction. Two maxima form at 40°N and 75°N, respectively. In October, the two maxima remain, but the speed of the zonal wind increases again.

If we closely compare the zonal winds in the same month but at different longitudes, we also see the changes in the shape of the jet stream as it travels eastward. In January, for example, at 75°E, the jet stream encounters high topography and forms two branches. At 140°E, the jet stream is much more concentrated in latitude. This finding agrees with the merging and splitting of the subtropical jet and the eddy-driven jet found by Lee and Kim (2003). It is important to note that the branch of the jet at the higher latitude(around 60°N to 70°N) has a maximum lower than 200 hPa, further suggesting that a zonal wind on the 200-hPa surface does not grant the complete picture of the jet stream.

To track the vertical variations of the jet core, we focus on the pressure-latitude cross-section of the 6-hourly(ERA-interim) wind field at the four different longitudes that we focus on(75°E, 95°E, 110°E, and 140°E). We locate the local maxima of the wind speed on each of these transects and record their latitude, altitude, and speed(Figure 4.6). We dictate that the maximum winds must be westerlies(having a positive U component) and discard the easterlies if present. When we locate more than two maxima(Figure 4.6(a)), we choose the two most pronounced maxima, the ones that have the highest wind speeds compared to the average of the entire plane(Figure 4.6(b)). We also allow it if there is only one maximum. This way we gather data not only on the latitude and the strength of the jet stream but also on the altitude and whether there are two branches.

4.4 Results

4.4.1 The Latitude and the Speed of the Jet Streams at 200 hPa

The latitude of the jet stream has been an important characteristic in the general circulation, as it signals the seasonal shift of the Hadley Cell and brings various meteorological phenomena along with it, including storms, atmospheric rivers, and blocking events. The jet is of even more interest in

the region of East Asia because of the existence of the Tibetan Plateau. The latitude of this wind relative to the plateau, in particular, has also been identified as the culprit for the organized precipitation over East China, Korea, and Japan(Ding and Chan, 2005). All of the importance above necessitates an accurate record of the latitude of the jet stream in East Asia.

The latitude of the jet stream in East Asian has been documented in broad terms, typically by tracing the maximum westerly wind at 200 hPa or 250 hPa(see Schiemann et al., 2009). The northern hemisphere, however, can have multiple fast and concentrated atmospheric flows that are bewilderingly named the 'jet stream'. The dynamic origins and the interactions of these different jet streams are beyond the scope of this study, but previously used tracking methods do not distinguish the different jet streams. Tracking a single maximum westerly wind could, therefore, result in finding different jet streams within a short time window, especially in spring and summer when the jet streams have similar speed. Previous descriptions of the latitude of the jet often have abrupt jumps(e.g. Figure 6 in Schiemann et al., 2009). It is not that the jet itself moves so far in latitude within a few hours, but rather the algorithm is picking up a different jet in the next moment that is far and happens to be stronger.

It is therefore important to distinguish the different jet streams and to give justice to each of them. Here we use the 2D jet tracking method(see Chapter 4.3.2.2) to produce 6-hourly maps of the jet stream, i.e. connected groups with wind speeds >20 m/s at 200 hPa. The 20 m/s threshold is used here to allow for weak jet streams during the summer. We focus on four different longitudes in the domain of East Asia: 75°E upstream of the Tibetan Plateau, 95°E right on top of the Tibetan Plateau, 110°E downstream of the Tibetan Plateau over the land of China, and 140°E over the Pacific Ocean(approximately the same longitude with Tokyo, Japan). At each longitude, we run across our map of the jet stream from 0° to 90°N; every time we encounter a jet stream(a connected group), we record the maximum wind speed and its latitude.

Figure 4.7 shows the climatology of the latitude and the maximum wind speeds of the two jet cores at the four longitudes. The most prominent feature is the relatively coherent jet stream in the south - positioned at around 25°N in the winter and migrating to 45°N in the summer. This jet represents

the subtropical jet stream at the northern bound of the Hadley Cell and undergoes a clear seasonal movement in latitude. The subtropical jet starts migrating northward in April until August when it reaches 45°N before it returns south again in the fall. Its speed is the fastest in the winter above 60 m/s and becomes slower starting in April. This jet is the weakest in summer, with a speed of approximately 20 m/s. It is worth noting that a wind slower than 20 m/s will not be identified as a jet stream in our work, as it will not significantly stand out against a 10 m/s background wind.

A secondary jet stream is evident at a higher latitude(between approximately 40° and 70°N), and its core location is more spread out and less organized than the subtropical jet. This secondary jet stream is strong in winter and weak in summer, just like the subtropical jet. Its latitudinal location indicates that it can be the eddy-driven jet in the mid-latitude. The variation of this jet stream in latitude(about 30°) is larger than that of the subtropical jet(less than 20°), but the variation of this jet stream in speed is smaller. The secondary jet is slower than the subtropical jet in winter but faster than the subtropical jet in summer; from April to October, the secondary jet is the stronger one between the two jets and will be captured if only one maximum is identified as the jet stream.

Across the four different longitudes, the northward movement of the two jet streams is more prominent at 110°E and 140°E than at 75°E and 95°E. This difference may be because the jet streams encounter Tibetan Plateau and become wavier after the Rossby wave is excited downstream of the plateau. Also, the two jet streams at 95°E are closer than at the other longitudes and less distinguishable from each other. The latitude of the two jet streams at different longitudes indicates that the search for a single maximum is not robust to the choice of longitude; capturing at least two maxima in the jet streams give a clearer characterization of the seasonal transition of the jet stream over the entire East Asian domain.

4.4.2 The Jet Streams in 3D

The positions of the subtropical jet and eddy-driven jet vary not only latitudinally but also in altitude. The 3-D tracking method in this work, therefore, is valuable because it allows us to see, for the first time, the change in the

vertical position of the two jet streams. Also, the distinction between the two jet streams is clearer if we look at them in the 3-D space.

The core of the jet stream where the maximum wind speed is located appears high in the atmosphere during winter at around or above the 200-hPa pressure level and moves lower as summer comes. The important thing to note in the variation of the height, however, is that by capturing the maximum wind speed, previous works may not be consistently capturing one single jet stream. When a drop in elevation is seen for the position of the maximum wind speed, there are two possible explanations. One is that the same jet stream moves to a lower altitude; the other is that there are at least two fast-flowing wind streams, at different altitudes, and the lower one becomes stronger than the higher one, hence being captured as a lowered maximum wind.

The method to identify the jet stream that allows for two branches of the jet stream, therefore, provides insight into the co-existence of the different kinds of the jet stream. Using the algorithm to track at most two peaks in the wind field within the pressure-latitude plane, mentioned in Chapter 4.3.2.3, we are able to disentangle the climatology of the two jet streams: the subtropical jet and the eddy-driven jet.

The subtropical jet stream, the most familiar to us and shown in blue in Figure 4.8, appears at the poleward boundary of the Hadley cell and migrates poleward from winter to summer together with the Hadley cell. The eddy-driven jet, shown in red, stays at around the same latitude of 55°N but makes an abrupt jump in mid-summer before it returns to 55°N in the fall. The two jets are therefore the closest to each other in spring and fall, and farther apart in winter and summer.

The height of the two jets also differs. The subtropical jet appears relatively stable around 200 hPa, and this fact helps the traditional tracking method of the jet stream successfully capture the subtropical jet by only looking at this altitude. The eddy-driven jet varies more in height, making almost periodical jumps from the 100-hPa surface to the 325-hPa surface, occasionally crossing with the subtropical jet at 200 hPa in the winter. The eddy-driven jet is usually lower in the spring, summer, and fall months.

If we combine Figure 4.8(a) and Figure 4.8(c), we can see that the two jet streams can become difficult to distinguish - they can appear on the same

pressure levels and share similar speeds. In fact, especially in winter months, we see the jet stream in the pressure-latitude plane as one elongated core across a big range of latitude(see Figure 4.5), simply because the two jet streams merge and become indistinguishable from each other. Our tracking method provides a new way to disentangle these two different jet streams just from their physical speed and location without any prior knowledge of their dynamic origin. This knowledge is valuable especially for the studies on the East Asian climate where only one jet is of interest instead of both.

4.4.3 The Dynamics of the Subtropical Jet and the Eddy-Driven Jet

Now that we have identified the two separate jet streams over East Asia both in 2-D and 3-D, we need to confirm that what we find are indeed the subtropical jet and the eddy-driven jet. The subtropical jet is formed at the poleward edge of the Hadley cell because of angular momentum conservation. The edge of the Hadley cell can be found at the closest point to the equator where the integrated meridional flow is 0(e.g. Kang and Polvani, 2011). The eddy-driven jet, on the other hand, is the strongest where the most eddy-momentum flux is deposited. Because the eddy-driven jet is also barotropic, previous works usually locate it by finding the maximum zonal wind(U) in the lower atmosphere, for example at 850 hPa(e.g. Kang and Polvani, 2011) or across multiple low levels(e.g. Woollings et al., 2010).

Here we examine these proxies for the theoretical positions of the subtropical jet and the eddy-driven jet. We take the region between 110°E and 120°E as an example, as it is a small area relevant to the East Asian rainband and the Meiyu. From Figure 4.9, the subtropical jet should be where the vertically-integrated density-weighted meridional transport above 500 hPa(purple) crosses 0 the first time north of 20°N. The subtropical jet is therefore at approximately 28°N in January and 42°N in July. This result agrees with our findings in Figure 4.7.

The eddy-driven jet, on the other hand, should be where the zonal wind at 850 hPa is at its maximum in Figure 4.8(green). Multiple prominent peaks can be observed in January, April, and October; the zonal wind is relatively

weak in July. In January, the peaks are at 42°N and 62°N; the positions are similar in April and October. In July, the peaks are small, and at 42°N and 78°N. This result agrees with our findings in Figure 4.8 in particular because the eddy-driven jet seems to have a wide range of its latitude in both winter and summer. It is possibly because there are two preferred locations of the eddy-driven jet at mid- and high-latitude, so that the eddy-driven jet appears more spread out in both Figure 4.7 and Figure 4.8. Also, the meandering of the eddy-driven jet can cause our detection algorithm to capture jet streaks that can appear in a wide range of latitudes.

A more direct indicator of the eddy-driven jet is the divergence of the eddy momentum flux; the eddy-driven jet is driven by a deposit of the eddy momentum flux. The most negative divergence, as shown in blue shading in Figure 4.10 is where the maximum eddy-driven jet should be in the zonally averaged field. In January, the peaks of the negative divergence are around 38°N and 50°N. In July, the divergence is weaker than that in January, and a smaller peak of the negative divergence is found around 50°N. The eddy momentum flux divergence roughly captures the two peaks of the eddy-driven jet found with the simple indicator of U at 850 hPa(in Figure 4.9) in January; the U at 850 hPa has three local maxima, and one of them appears near 50°N. The eddy activities are generally weak in summer and can be zonally asymmetric, and it is reasonable that the resulting signature of the eddy-driven jet does not have a perfect agreement with the zonally averaged eddy momentum flux. In fact, there is usually an offset between the latitude of the jet stream and that of the eddy momentfum flux divergence in idealized experiments(e.g. Bordoni and Schneider, 2008). Nevertheless, Figure 4.10 confirms that the jet stream around 50°N can be driven by eddy activities almost all year round.

Overall, we confirm our findings that the subtropical jet is around 28°N in winter and moves to 45°N in summer; the eddy driven jet takes up a broader range of latitude and can have several preferred locations, but should be found between 45°N and 60°N in winter and between 50°N and 70°N in summer. Again, there can be significant overlap of the latitude of the two jets, and many times they are not physically separable at all in some parts of the world in certain seasons. Nevertheless, our tracking method is able to disentangle the two jets correctly, confirmed by their dynamic sources respectively.

4.4.4 The Number of Maxima in the Jet Streams

The number of maxima in the jet streams is an important trait that has rarely been captured, especially in the East Asian domain where the Tibetan Plateau comes in as a crucial player. Within the East Asian domain, multiple local maxima of the zonal wind can be observed along the same longitude. The multiple maxima of the jet speed, or the split of the jet stream, can be viewed from two different perspectives. The first is the distinction between the subtropical jet and the eddy-driven jet. According to Lee and Kim (2003), the jet stream has a single maximum when the subtropical jet is strong and pulls the eddy-driven jet close to it, and has double maxima when the subtropical jet is weak. On top of that, the previous section also shows that the eddy-driven jet can have several preferred locations, because the eddy momentum flux divergence can peak at multiple locations at the same time.

The second perspective is the conservation of potential vorticity; similar to a Taylor-column problem, the Tibetan Plateau serves as an obstacle that forces the flow to go around it. A single jet stream can split into a northern and a southern branch when it encounters the plateau. The subtropical jet stream, therefore, can further split into more than one branch if it is within the latitudinal range of the Tibetan Plateau. Although the subtropical jet is baroclinic and the strongest at high altitude(around 200 hPa), the lower and slightly weaker component in it can still be influenced by the tall Tibetan Plateau that reaches above 4000 m in height. The split configuration of the subtropical jet stream is also linked to important phenomena, including the East Asian Summer Monsoon. In this case, there can be 3 to 4 jet maxima, taking into account the two branches of the subtropical jet and the one or two preferred locations of the eddy-driven jet.

Following the identification of the jet stream, we design an algorithm to capture the different configuration of the jet stream over the East Asian domain. We now define the number of maxima in the jet streams for East China: from 90°E to 110°E, at each longitude(0.75° apart) we count how many times we cross the previously identified jet streams. For example, if the jet stream has a single maximum within the predefined box, we will count one; if the jet stream splits into two branches, we will count two. We also

make sure that we do not mistake some small protruding shape of the jet stream for a branch by eliminating a count that is 2 degrees closer to the previous count. Then we average all counts from 90°E to 110°E to a single number and call it the number of jets over East China.

Here we show a climatology of the number of maxima in jet streams over East China(Figure 4.11). During the winter, the subtropical jet stream is strong and concentrated to the south of the Tibetan Plateau. The flow of the subtropical jet is not blocked by the topography, so it is more likely to stay coherent. The eddy-driven jet appears separate sometimes but can merge with the fast subtropical jet. The number of maxima is between 1 and 2, meaning that about half of the time there is only one jet observed; the other times there are two jets. As it proceeds into the spring, the number of maxima gradually increases and reaches a peak of approximately 2.6 in May, also the month when the peak rainband season in East Asia starts. During this season, more than three maxima of the speed of the jet stream are sometimes detected along the same longitude.

Spring is the season when the subtropical jet migrates north within the latitudinal range of the Tibetan Plateau; the blockage of the topography can cause the jet to form two branches to circumvent it. In fact, this behavior can be confirmed by disentangling the subtropical jet and the eddy-driven jet and counting their maxima respectively. In Figure 4.12, the baroclinic subtropical jet is represented by the vertical difference of U between 200 hPa and 850 hPa; the barotropic eddy-driven jet is represented by the vertically averaged U between 200 hPa and 850 hPa. The numbers of maxima in each jet are then collected for each longitude between 90°E and 100°E before averaged. The number of maxima in the subtropical jet increases in spring from 1.25 to 1.75, while the eddy-driven jet mostly remains one branch. After this peak, the number of maxima in jet streams drops low during the summer when the jet stream continues to move north to pass the northern edge of the Tibetan Plateau. Also in summer, both the eddy-driven jet and the subtropical jet become weak so that sometimes they drop below the 20 m/s threshold to be detected as a jet. When the wind returns south again during the fall, the number of maxima once again rises and reaches near 2 in November, before it decreases into winter. It is worth noting that the jet stream with multiple maxima is a characteristic of the East Asian region and does not hold in

the zonal-mean zonal flow where only one jet appears at 30°N in winter(e.g. Figure 7.5 in Peixoto and Oort, 1992).

4.4.5 The Northerly Component in the Jet Stream

In Chapter 2, we find that the northerly flow over East China is critical to the formation of the Meiyu front. We hypothesize that this northerly wind is part of the Rossby wave excited by the Tibetan Plateau in Chapter 3. Previous studies also propose that when the northerly wind over East China weakens, the Meiyu season terminates(Kong and Chiang, 2020). The northerly flow is therefore important to study for the climate over East Asia.

In this section, we characterize the seasonal variation of the northerly component of the jet stream on the 200-hPa level over East China, as an important part of the atmospheric circulation over East Asia. This is different from the northerly wind in the mid-troposphere(at 500 hPa) described in Chapter 2, as they are on different levels.

To capture the northerly component of the jet stream over East China, we first identify the jet stream in the East Asian domain by the method mentioned in Chapter 4.3.2.1. Then, we narrow down the field to East China that includes only the region from 25°N to 50°N, 105°E to 120°E. Within the identified jet stream in this smaller region, we look for the northerly component. For each time step, we use two metrics to characterize this northerly component: the maximum northerly wind speed(V) and the sum of meridional wind speed of all grid points with northerly wind speed($V<0$). The latter serves as an integrated strength for the northerly in the upper level of the atmosphere.

The climatology of the northerly wind is again gathered from 1979 to 2018. As shown in Figure 4.13, the strongest northerly wind within the jet stream stays around 20 m/s from mid-autumn to early spring. Then towards the end of May and the beginning of June, the northerly wind speed picks up and rises to 30 m/s. This late-spring and early-summer timing are the same as the peak of the season of the East Asian rainband as described in Chapter 2. In summer, the northerly wind dies down to the global minimum of the year at around 5 m/s. This abrupt transition from the peak in June to

the plunge in July corresponds to the weakening and the demise of the East Asian Summer Monsoon within the same period.

The integrated strength of the northerly component in the jet stream also shows an abrupt change in its climatology. In Figure 4.14, the color signifies the number of the grid points with a northerly component in the jet, whereas the y-axis shows the integrated strength of this northerly, calculated as the sum of the magnitude of all northerly winds in the domain. From late fall to early spring, the integrated strength stays around the same, unlike the maximum northerly which shows a significant peak in spring. However, starting from June, both the number of grid points with northerly and the integrated strength decline significantly and stay at the bottom until September. This result indicates that northerlies over East China are rare and weak during the summer.

On top of the magnitude and integrated strength of this northerly component in the jet stream, we also investigate the change in its location. When locating the single maximum of the northerly component for each time step, we record the latitude and the longitude of each maximum. Note all the wind fields are at 200 hPa, usually considered the level of the jet stream. The climatology is summarized in Figure 4.15. The latitudinal location of the northerly component has a distinct seasonal cycle: in winter, the maximum northerly appears around 45°N, and gradually migrates south. In spring, this maximum centers around 40°N and penetrates as far as 30°N in mid-summer. The northerly is the strongest when it is near the northern edge of our chosen domain and is the weakest near the south.

As far as the longitudinal position goes, the climatology again shows a different cycle. In spring, the maximum northerly is the furthermost to the east, situated around 115°E. Then the maximum gradually migrates westward, stopping in August around 107°E, and starts coming back east in fall. In mid-winter, the maximum again drifts to the west, but not as west as in mid-summer, only reaching around 112°E. Here it is worth noting that the range of changes in longitudinal positions, although with a clear seasonal cycle, is small and confined to the relatively flat part of the land in East China.

While this work investigates the behaviors of the jet stream, often defined to be centered near the tropopause or around the 200-hPa surface, the

northerly winds in the mid-troposphere around 500 hPa deserves our attention. The northerlies over east China are interesting mainly because they interact with the Tibetan Plateau, most of which stands around the height of 5000 m to 6000 m, corresponding to the 500-hPa surface. So the northerlies on the 200-hPa surface are interesting as part of the jet stream, but those at 500 hPa is more significant for the understanding of the regional circulation and climate.

For the study on the climate in the East Asian region, the northerlies around 500 hPa are crucial in that its strength dictates how far the northward transport of the moisture from the ocean can penetrate east and north China. The climatology of the northerlies is closely tied to that of the Meiyu front(Kong and Chiang, 2020).

Not surprisingly, the northerlies on the 500-hPa surface undergo a seasonal transition both in its speed and its latitudinal location. Unlike on the 200-hPa surface, however, the northerlies do not peak in the spring but gradually weaken from the winter into the summer. The figure below shows the maximum northerly within the East Asian domain on the 500-hPa surface. The northerlies in this region undergo a regime change: the winter and the spring see a stable maximum northerly around 30 m/s, and from late spring the northerlies weaken to reach around 20 m/s. The months when the northerlies gradually decrease in speed and retreat north correspond to the time when the moisture can penetrate north and leads to a northward migrating precipitation front.

4.5 Summary and Discussion

In this work we present a detailed description of the jet streams, focusing on the region of East Asia and around the Tibetan Plateau. We are able to identify the position and speed of the subtropical jet and the eddy-driven jet, respectively, both in 2-D and 3-D in the ERA-Interim reanalysis dataset. The number of maxima in jet streams and the northerly within the jet are also examined. The main findings are below:

- We have developed a novel method to track the jet streams in East Asia by finding connected components in wind fields faster than 20

m/s in the 3-D space and then locating the maxima of wind speed. By allowing a lower threshold for wind than the traditional threshold(30 m/s) and multiple maxima, we are able to show the coexistence of the subtropical jet and the eddy-driven jet throughout the year. Both the subtropical jet and the eddy-driven jet undergo seasonal northward migrations from winter to summer. The subtropical jet is coherent in its latitude while the eddy-driven jet is more sporadic in all seasons. The subtropical jet is strong in winter and located around 25°N; it weakens in spring and summer and is located around 45°N in July, and moves back south in fall. This latitudinal range of movement agrees with the findings by Schiemann et al. (2009). The eddy-driven jet, on the other hand, can be found between 45°N and 60 in winter and between 50°N and 70°N in summer, with a smaller drop in speed in summer than the subtropical jet has. The location of the eddy-driven jet has more variability and can also have multiple preferred locations based on the location of the eddy momentum flux divergence. The subtropical jet is the stronger of the two jets in winter, but starts to weaken in spring and can be the weaker of the two in spring and summer. Our work successfully captures each jet and avoids mistaking the stronger eddy-driven jet in spring and summer as a subtropical jet that has moved north. Our characterization of the jet streams extends the traditional view resulting from looking for a single zonal wind maximum in the upper troposphere or at a single pressure level.

- The number of maxima in the jet streams is defined and identified for East Asia in this work. It is shown that the jet stream has on average 1.6 maxima in January at the lowest and 2.6 maxima in May at the highest. This result suggests that there is usually more than one jet stream present(the subtropical jet and the eddy-driven jet). In spring, when the subtropical jet is within the latitudinal range of the Tibetan Plateau, the topography will further make the subtropical jet split into more than one branch; the eddy-driven jet can also have multiple preferred locations. Therefore, we often see several maxima in jet streams between 2 to 5, and the number averages to 2.6 in May. After this peak in May, the subtropical jet moves further north and

is less influenced by the Tibetan Plateau, so the number of maxima decreases. The "split-flow" configuration of the subtropical jet is also captured in Schiemann et al. (2009), and our characterization of the eddy-driven jet completes the picture of multiple jets in the vicinity of the Tibetan Plateau.

- The northerly component within the jet stream is important for understanding the regional climate in East Asia and especially around the Tibetan Plateau. The northerly on the 200-hPa surface is weak in the winter, increases and reaches its peak in the spring, decreases in the summer, and sees another smaller peak in the fall. On the 500-hPa surface, the maximum northerly wind remains the same from winter to spring and starts to weaken from spring into summer before it picks up again in the fall. This weakening phenomenon allows for northward penetration of the moisture into north China in the spring and summer. The northerly wind, both on the 200-hPa and 500-hPa surface, has been in the focus for the first time because it is a direct signature of the fast-flowing jet stream interacting with the Tibetan Plateau. The northerly wind can also be tied to the East Asian rainband and the Meiyu season in general, and therefore contributes significantly to the understanding of the timing of the Meiyu termination.

- This work provides an unprecedented characterization of the jet streams in 2-D 3-D space over East Asia throughout the year. The familiar story of the jet stream moving north across the latitudinal range of the Tibetan Plateau(28°N to 38°N is about the subtropical jet, not the eddy-driven jet, as the eddy-driven jet is always north of that range. The multiple branches of jet seen over East Asia, however, are a combination of both the subtropical jet and the eddy-driven jet. Both jets contribute at least one branch; both can have multiple. The subtropical jet can split to travel around the Tibetan Plateau, while the eddy-driven jet can have multiple preferred locations. The subtropical jet is the one responsible for most theories that relate the jet to the East Asian precipitation(e.g. Yeh et al., 1959; Sampe and Xie, 2010; Chiang et al., 2015a), but the eddy-driven jet can also play a role by

modulating the baroclinity and creating transverse flows in the area.

4.5.1 Future Work

Potential future work includes establishing a quantitative relationship between the different features(the number of maxima and the northerlies) of the jet streams and precipitation metrics over East Asia. a similar characterization of the jet streams not only for the region of East Asia but over the entire globe. The jet stream is an interesting feature for the climate in many different regions, carrying baroclinicity, storms, blocking, and other weather phenomena with it. The jet stream also serves as a link between the weather and climate in locations far away from each other. Using the identification and tracking method established in this work, the jet stream will be easily captured and analyzed for its role in different parts of the world.

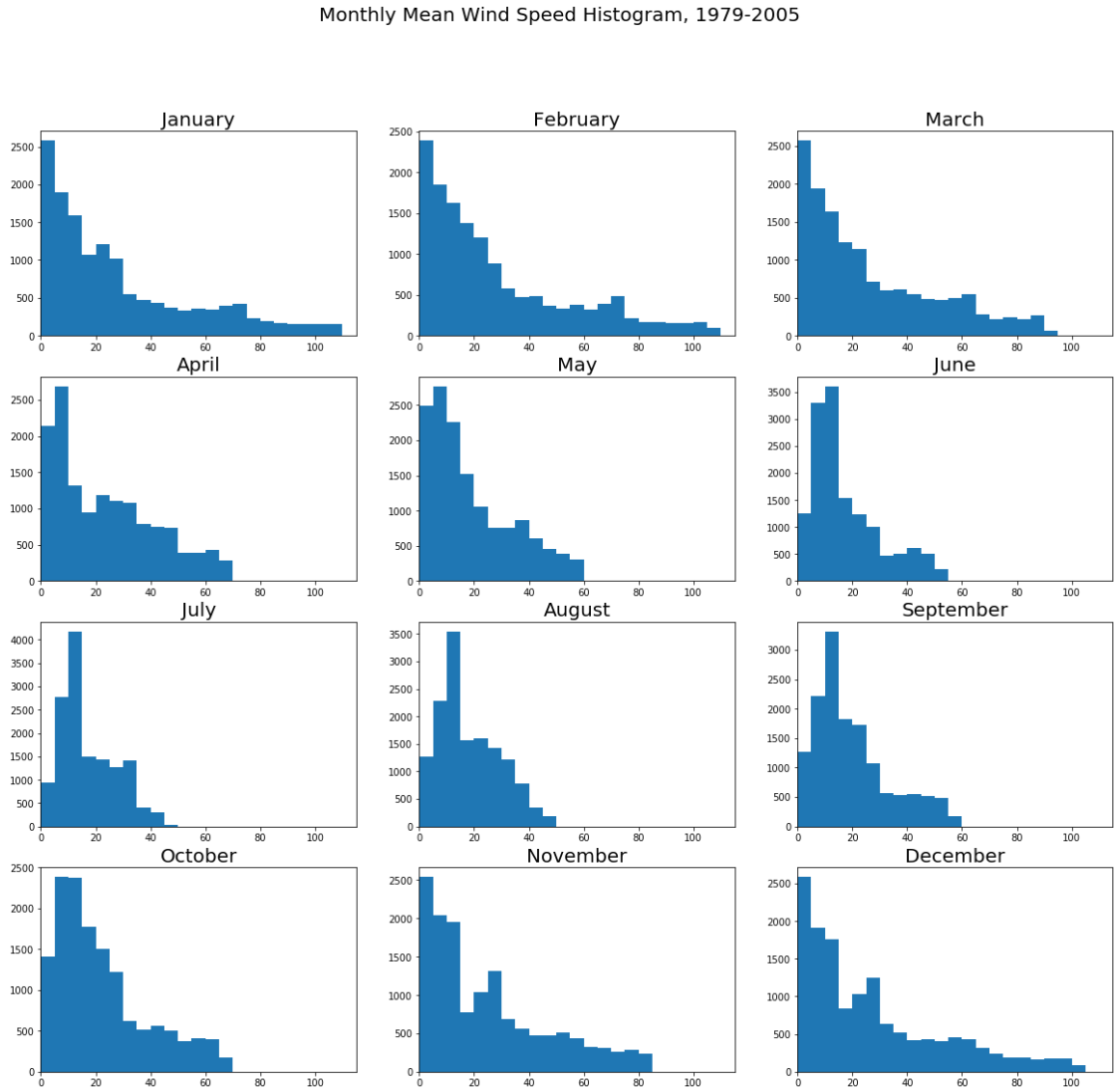


Figure 4.1: Climatology(1979-2005) of the distribution of the wind speed in each month on the 200-hPa pressure level. The x-axis shows the wind speed($\sqrt{U^2+V^2}$) and the y-axis shows the number of occurrences in each month. In winter, fast winds above 100 m/s are observed, while in summer the winds are capped below 60 m/s.

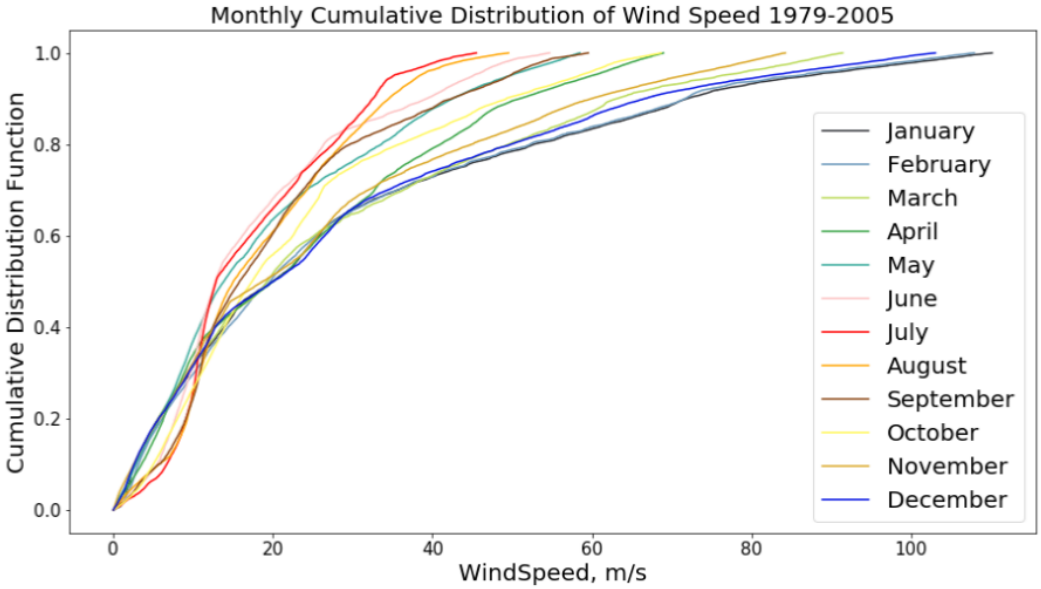


Figure 4.2: Cumulative Distribution Function of the wind speed over East Asia on the 200-hPa level, climatology for 1979-2018. The wind speed is defined as $\sqrt{U^2 + V^2}$. The warmer colors represent warm months, and cold colors are cold months. The wind is the slowest in July and the fastest in January.

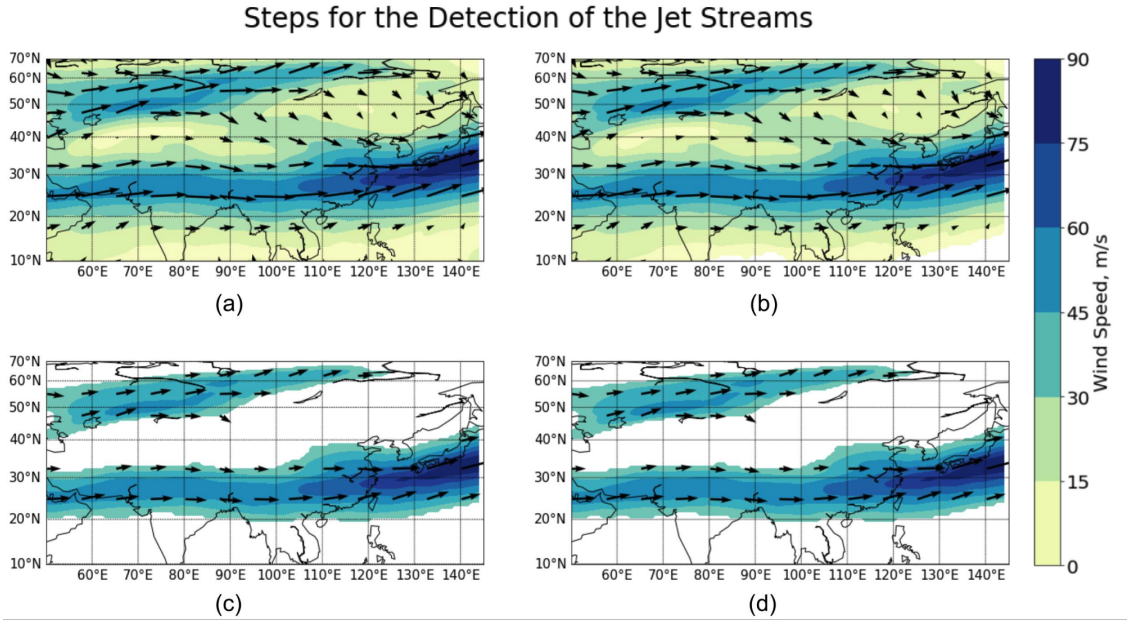


Figure 4.3: The steps to identify the jet stream in the 200-hPa wind field. (a) shows the original wind field(the color is wind speed) on January 1st 00:00, 1979 over Asia. (b) shows the wind field where the wind has a westerly zonal component($U > 0$). The field is largely westerly at this timestamp, but notice some areas over the bottom right corner are removed. (c) shows the wind field where the wind speed($\sqrt{U^2 + V^2}$) $\geq$ 20 m/s.(d) shows the filter in (b) and (c) combined, so the remaining wind has both $U > 0$ and $\sqrt{U^2 + V^2} \geq$ 20 m/s.

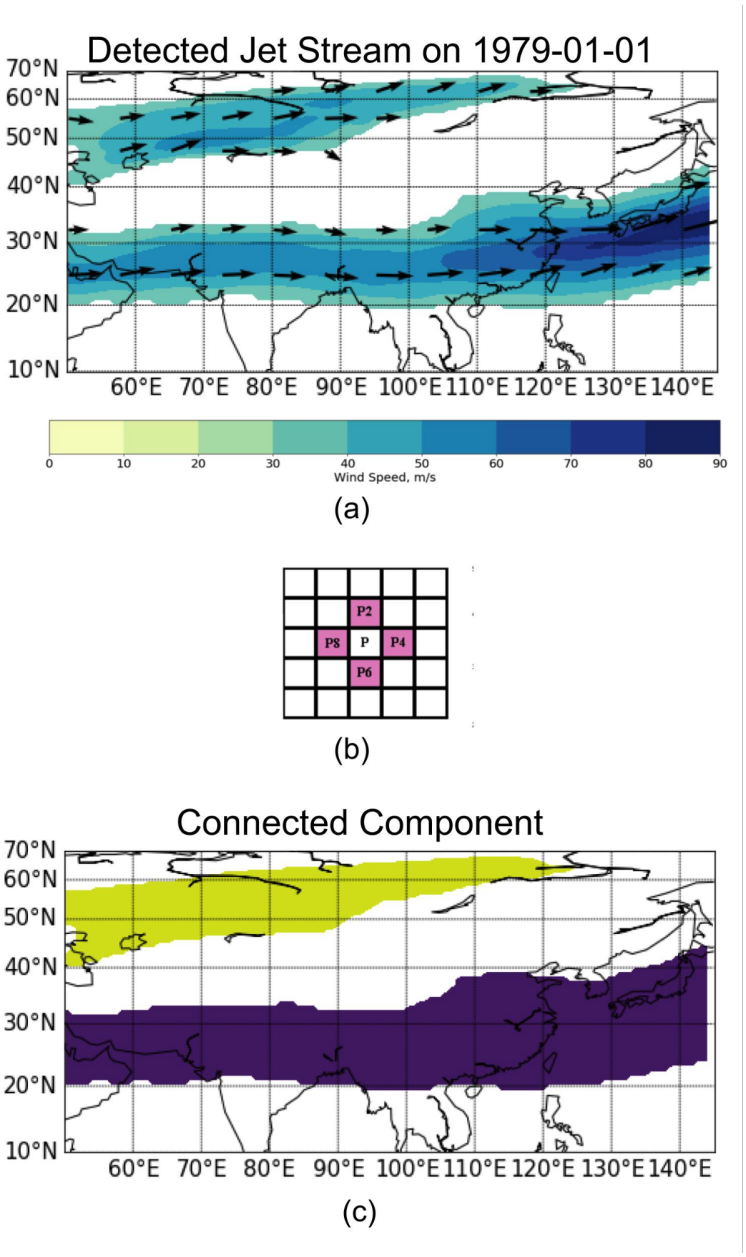


Figure 4.4: An illustration of the detection of connected components. (a): the wind field that meets the requirement of $U > 0$ and $\sqrt{U^2 + V^2} \geq 20$ m/s. (b): the 4-connectivity in which only the grids that share a side are considered connected. (c): the two detected connected components(in yellow and purple, respectively).

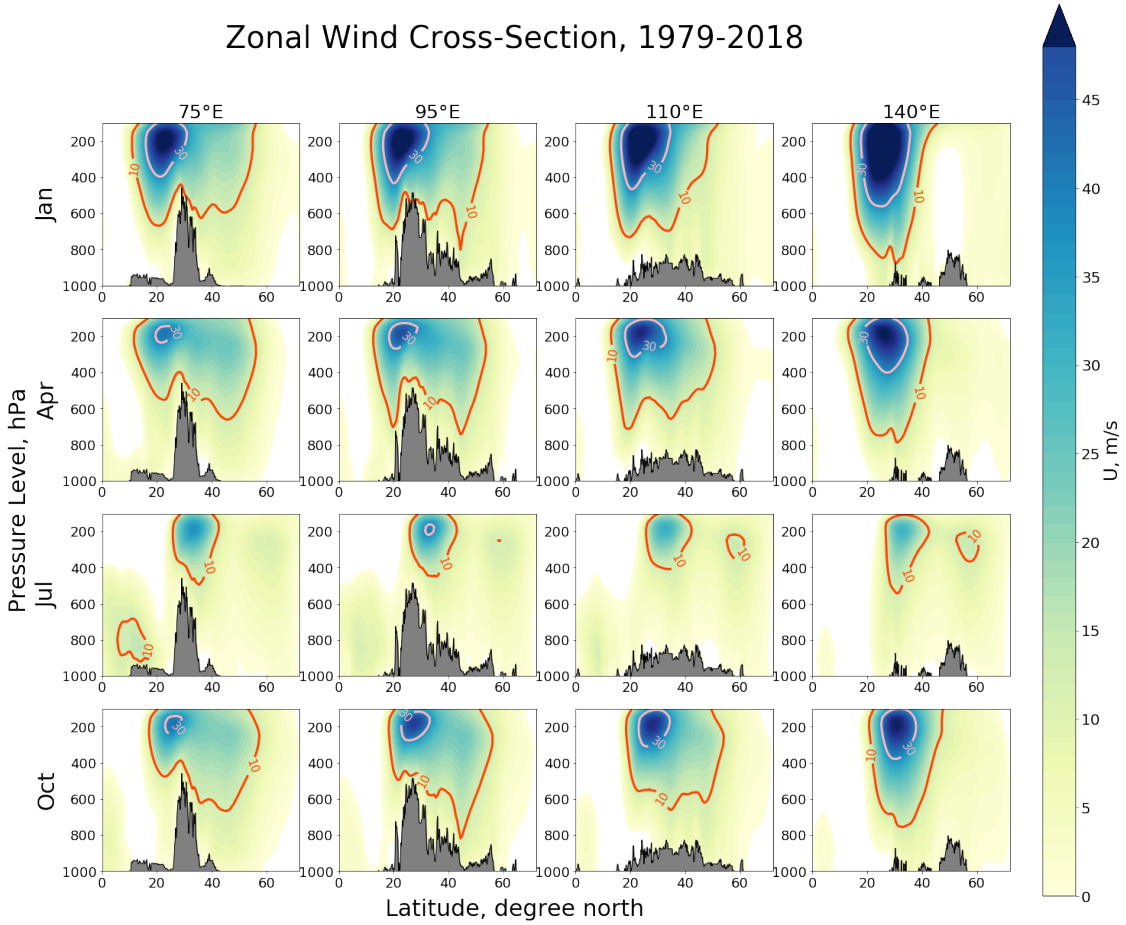


Figure 4.5: The cross-section of the zonal wind at 75°E(west of the Tibetan Plateau), 95°E(over the Tibetan Plateau), 110°E(East China), and 140°E(Japan). The climatological wind is calculated for January, April, July, and October for 1979-2018. The shading is zonal wind U in m/s, and the contours are 30 m/s(pink) and 10 m/s(red). The grey shading is topography.

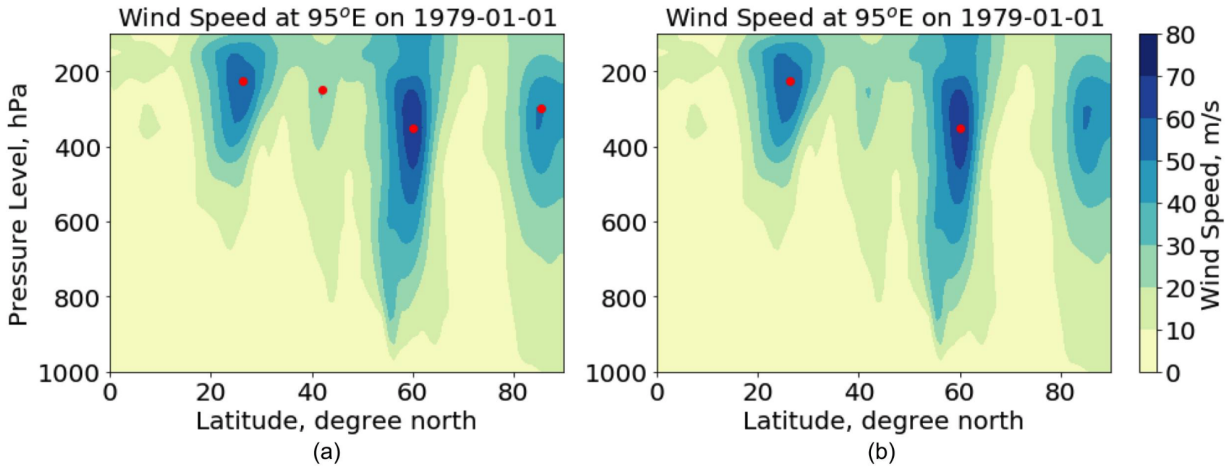


Figure 4.6: Tracking the jet stream by locating the maxima of the wind speed in the latitude-pressure plane. The wind speed(in color) is defined as $(U^2 + V^2)^{1/2}$. The example here shows the cross-section of the wind speed at 95°E(from 0°N to 90°N, and from 1000 hPa to 100 hPa). The local maxima of the wind speed are detected first(red dots) in(a); only the two most prominent maxima(strongest wind speed) are kept for the final result of detection in (b). This way the two strongest signatures of the jet streams are detected and the smaller features and branches are neglected.

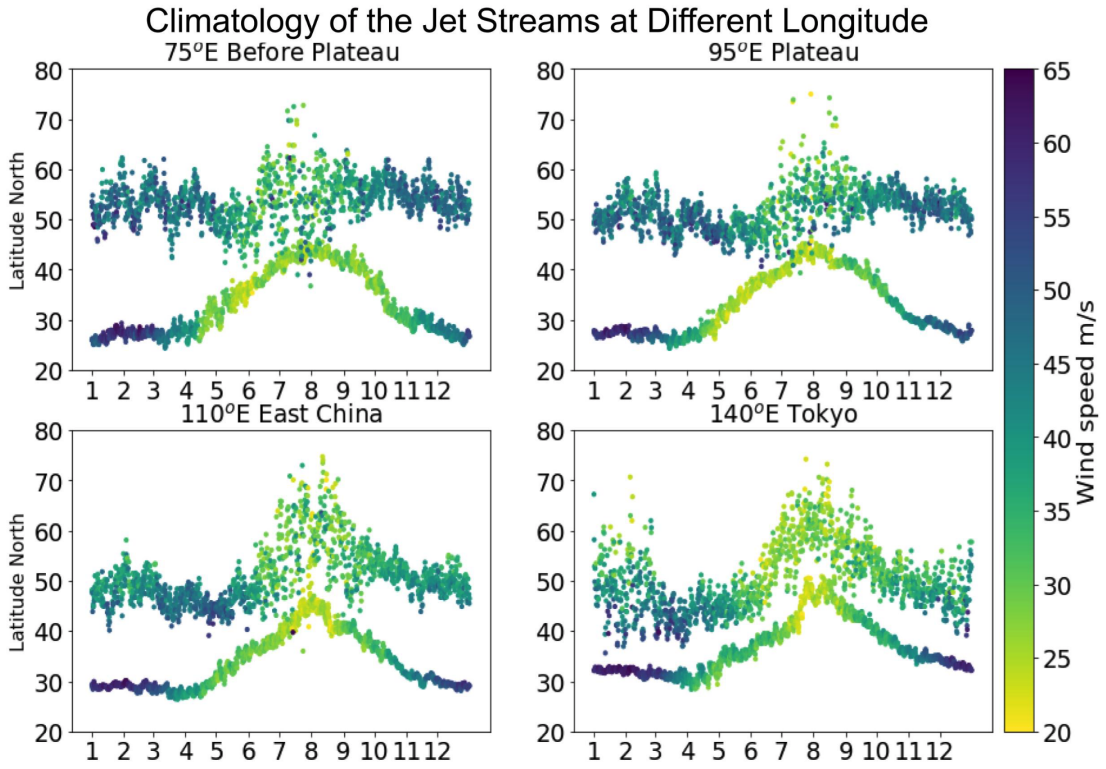


Figure 4.7: The climatology of the latitudinal position of the jet stream (a)west of the Tibetan Plateau, (b) over the Tibetan Plateau, (c) east of the Tibetan Plateau, (d) over east Pacific.

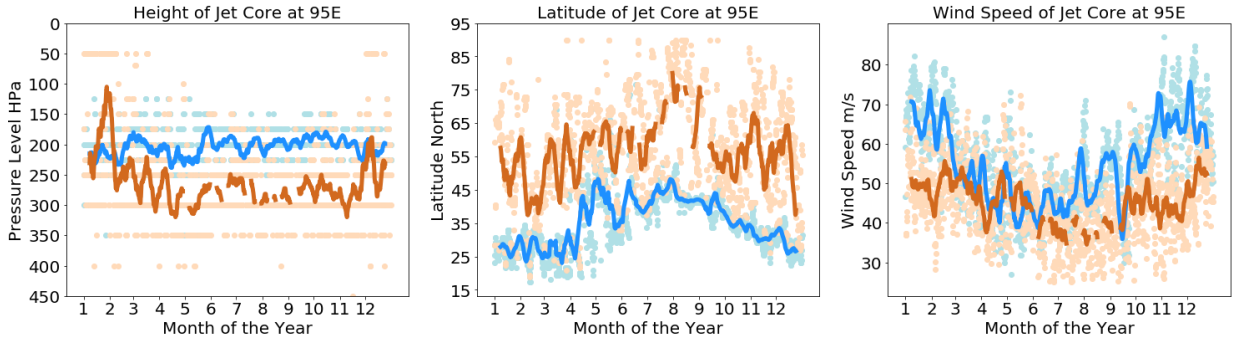


Figure 4.8: The climatology of the subtropical jet(blue) and the eddy-driven jet(red) at 95°E, 1979-2018. The height of the subtropical jet is stable at around 200 hPa throughout the year, while the eddy-driven jet fluctuates between 100 hPa and 325 hPa. The eddy-driven jet is lower in summer and higher in winter. Both the subtropical jet and the eddy-driven jet migrate north from winter to summer; the subtropical jet moves from 25°N to 45°N, while the eddy-driven jet moves from 45°N to 75°N. Both jets are fast in winter and slower in summer. The subtropical jet is much faster than the eddy-driven jet in winter, but their speeds become similar in spring and summer.

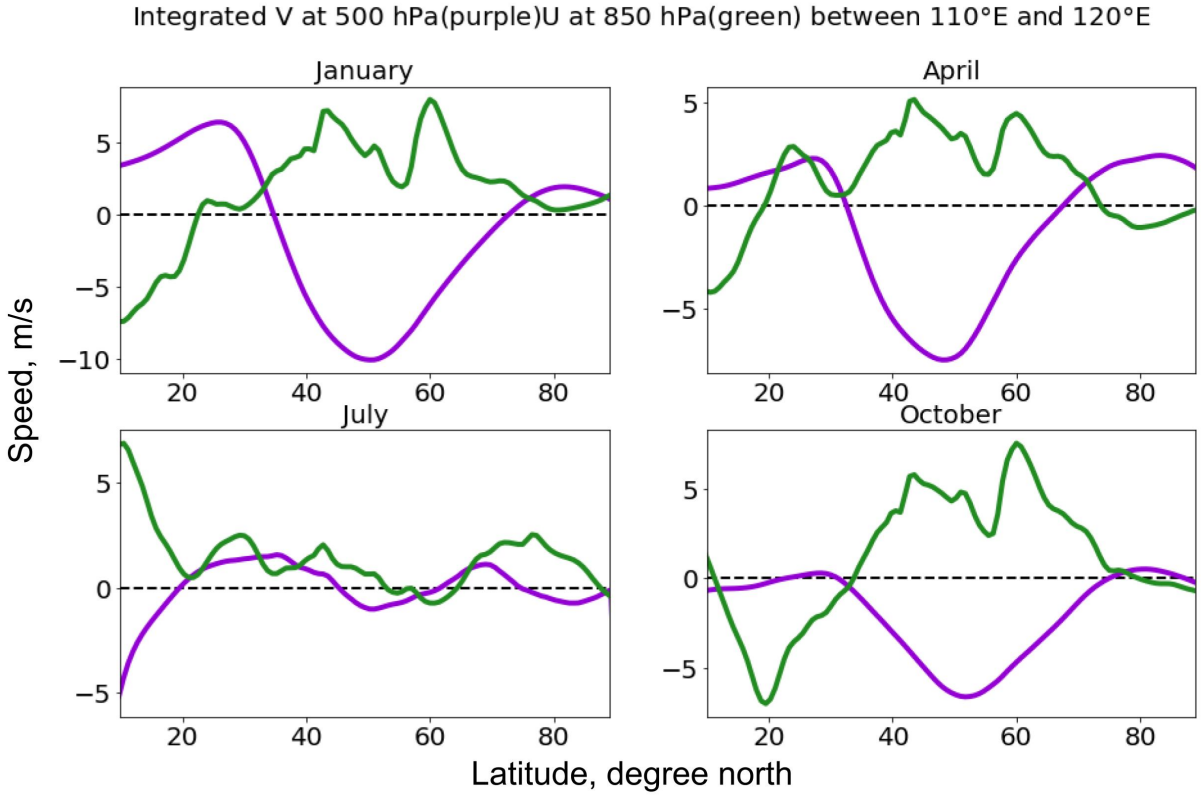


Figure 4.9: The integrated meridional wind at 500 hPa(purple) and the maximum zonal wind at 850 hPa(green) between 110°E and 120°E. The integrated meridional wind serves as a proxy for the Hadley cell; where it crosses 0 for the first time north of 23°E is the northern edge of the Hadley cell. Maximum U at 850 hPa is a proxy for the eddy-driven jet; its peak shows where the eddy-driven jet is the strongest.

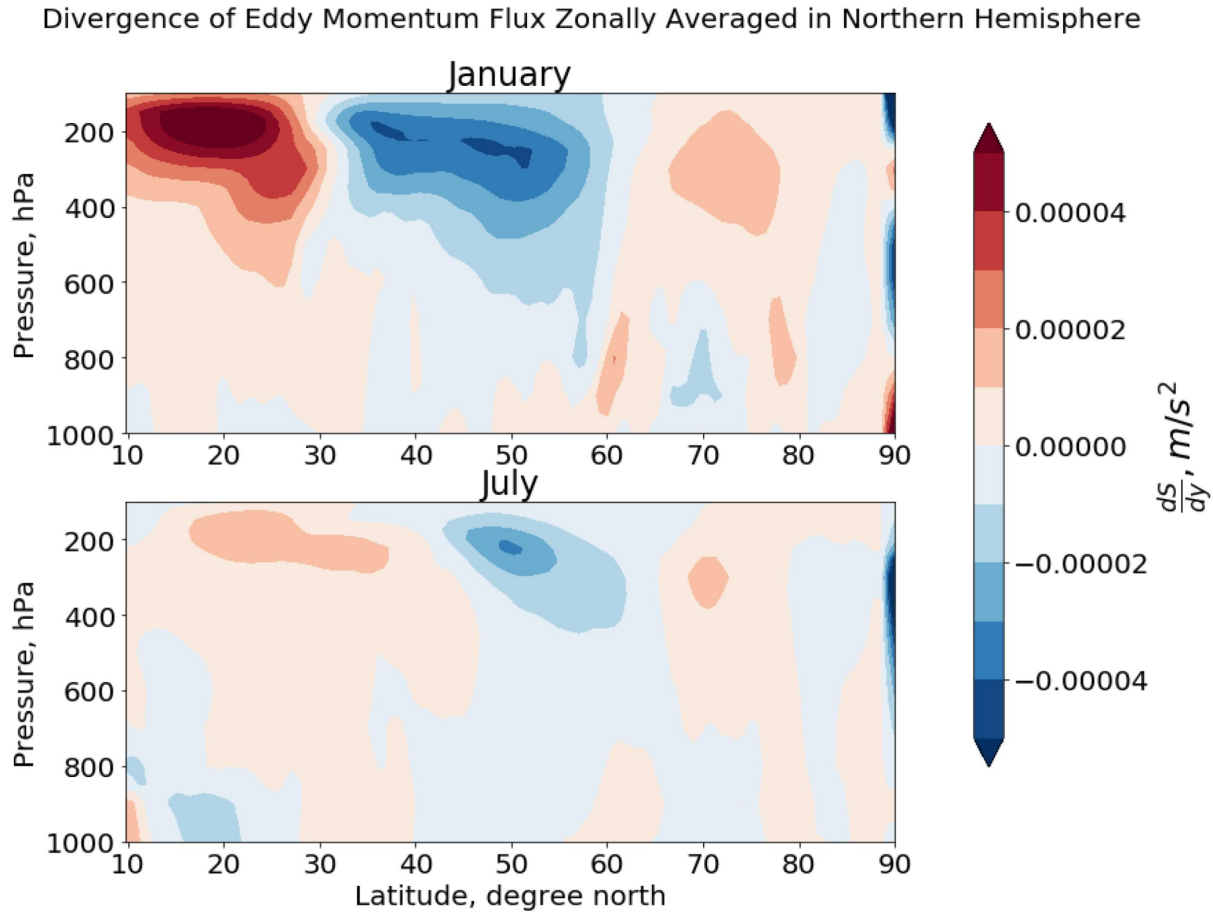


Figure 4.10: The zonally averaged divergence of eddy momentum flux in January and July. The darkest blue shading is where the most eddy momentum flux is deposited. In January, there are two maxima at 38°N and 50°N. In July, the divergence is weak with a single maximum at 50°N.

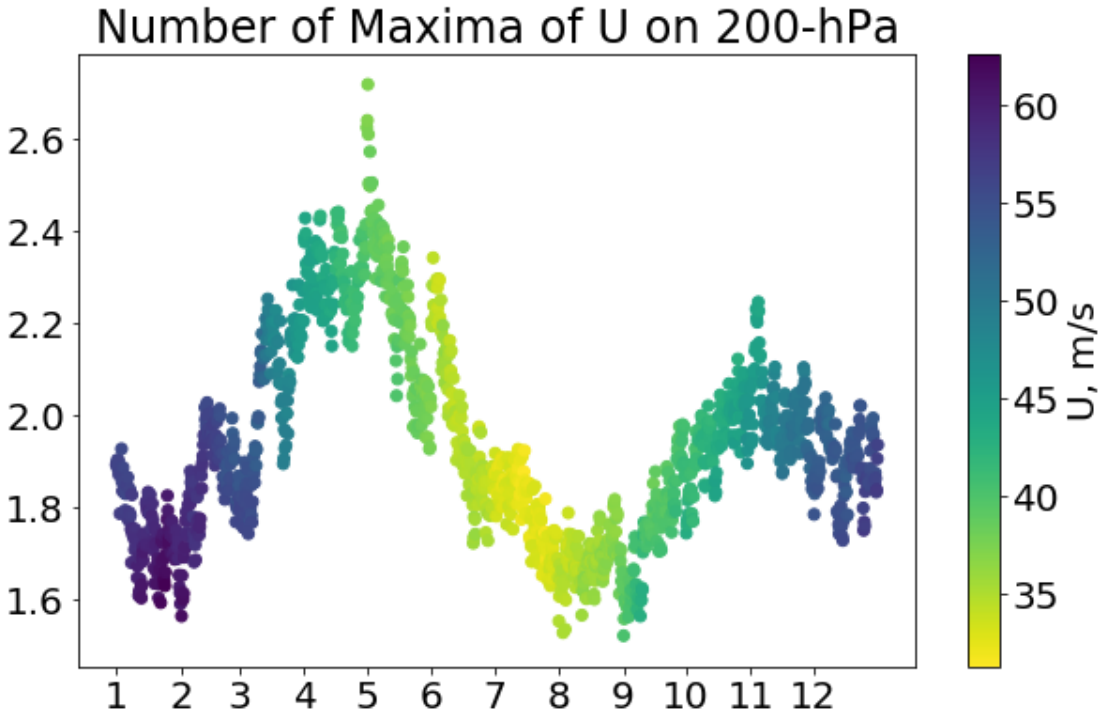


Figure 4.11: The climatology of the number of maxima in jet streams(y-axis) and the corresponding speed of the jet stream(color), 1979-2018. The jet is fast and has a maxima branches of 1.6 in winter. The number of maxima increases in spring and reaches its peak in May before it decreases again. This increase is associated with the subtropical jet moving in the latitudinal range of the Tibetan Plateau in this season; the topography forces the flow to split to move around it. A smaller peak of the number of maxima in jet happens in November.

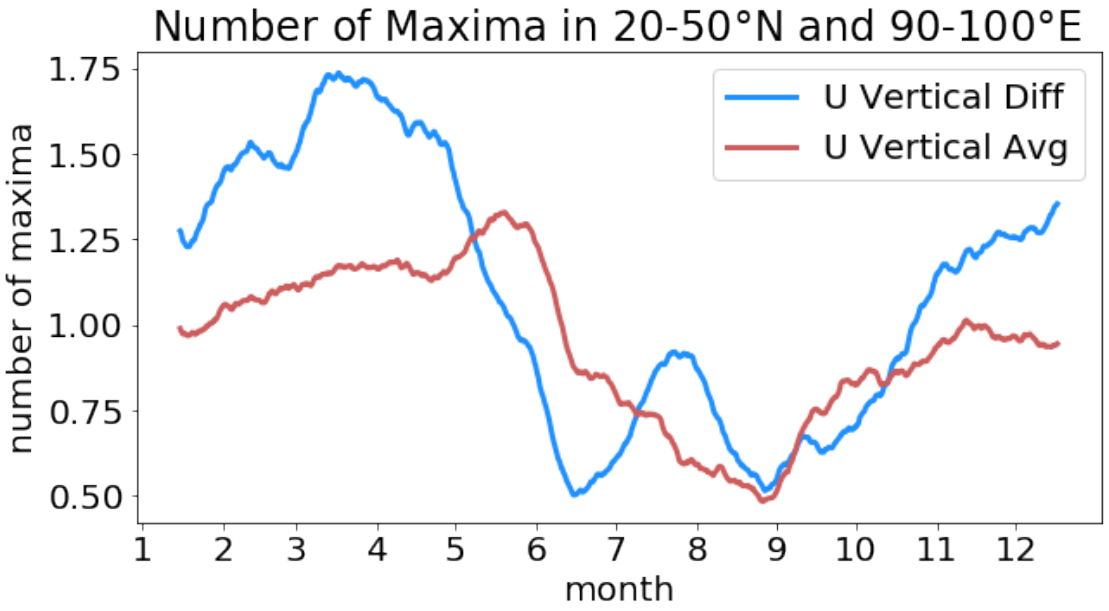


Figure 4.12: The climatology of the number of maxima in jet streams(y-axis) in 20-50°N and 90-100°E. The blue shows the number of maxima in the vertical difference of U between 200 hPa and 850 hPa; this serves as a proxy for the baroclinic subtropical jet. The red shows the number of maxima in the vertically averaged U between 200 hPa and 850 hPa; this serves as a proxy for the barotropic eddy-driven jet. In spring, the subtropical jet splits around the Tibetan Plateau to form two branches and has an increase in the number of maxima. The eddy-driven jet remains approximately 1 maximum until it is sometimes too weak or too far north to be detected in summer, therefore the drop in the number of maxima starting in June.

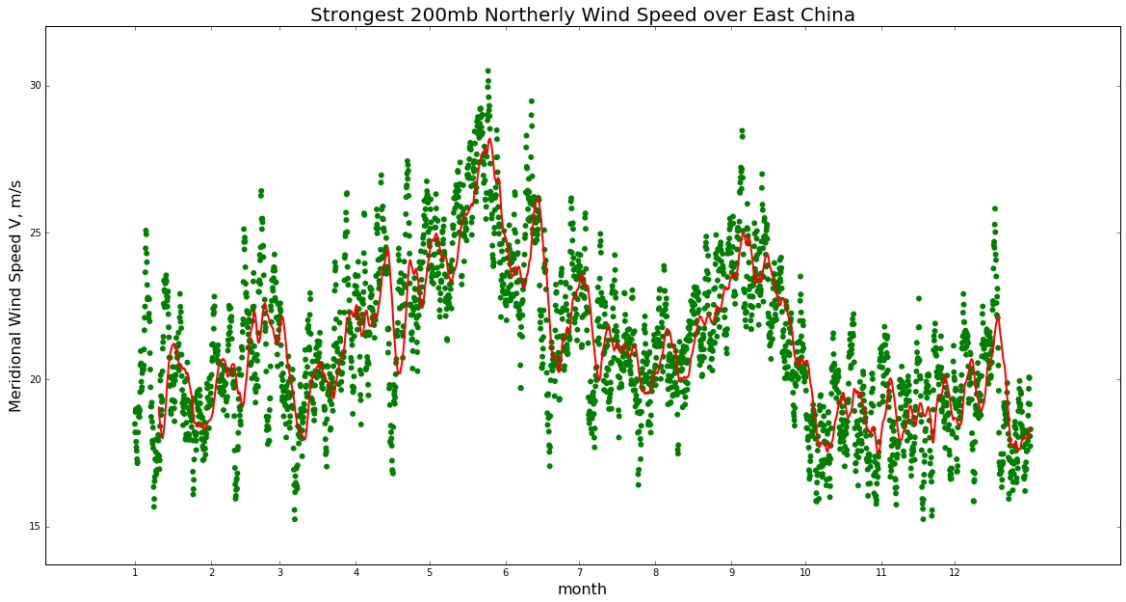


Figure 4.13: The climatology of the maximum northerly wind at 200 hPa over East China. The northerly wind on 200 hPa is slow in winter and grows strong to reach its peak in May. This peak happens at the same time as the peak in the jet split index; the increase in the northerly wind is most likely due to the interaction between the jet stream and the Tibetan Plateau. A secondary peak happens in September when the jet stream retreats south.

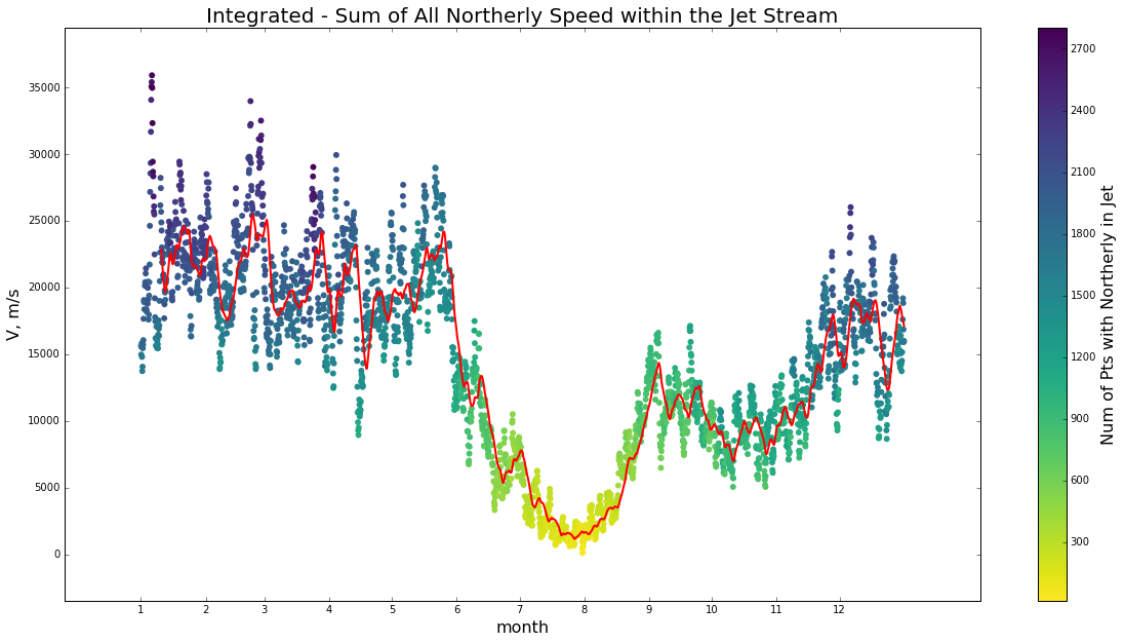


Figure 4.14: The climatology of the integrated strength of the northerly wind over East China, 1979-2018. The integrated strength is defined as the sum of all northerly wind over the region of East China. The integrated strength is strong from January to April. Starting from mid-May, it takes a plunge to reach its minimum in July and August before it rises again in fall.

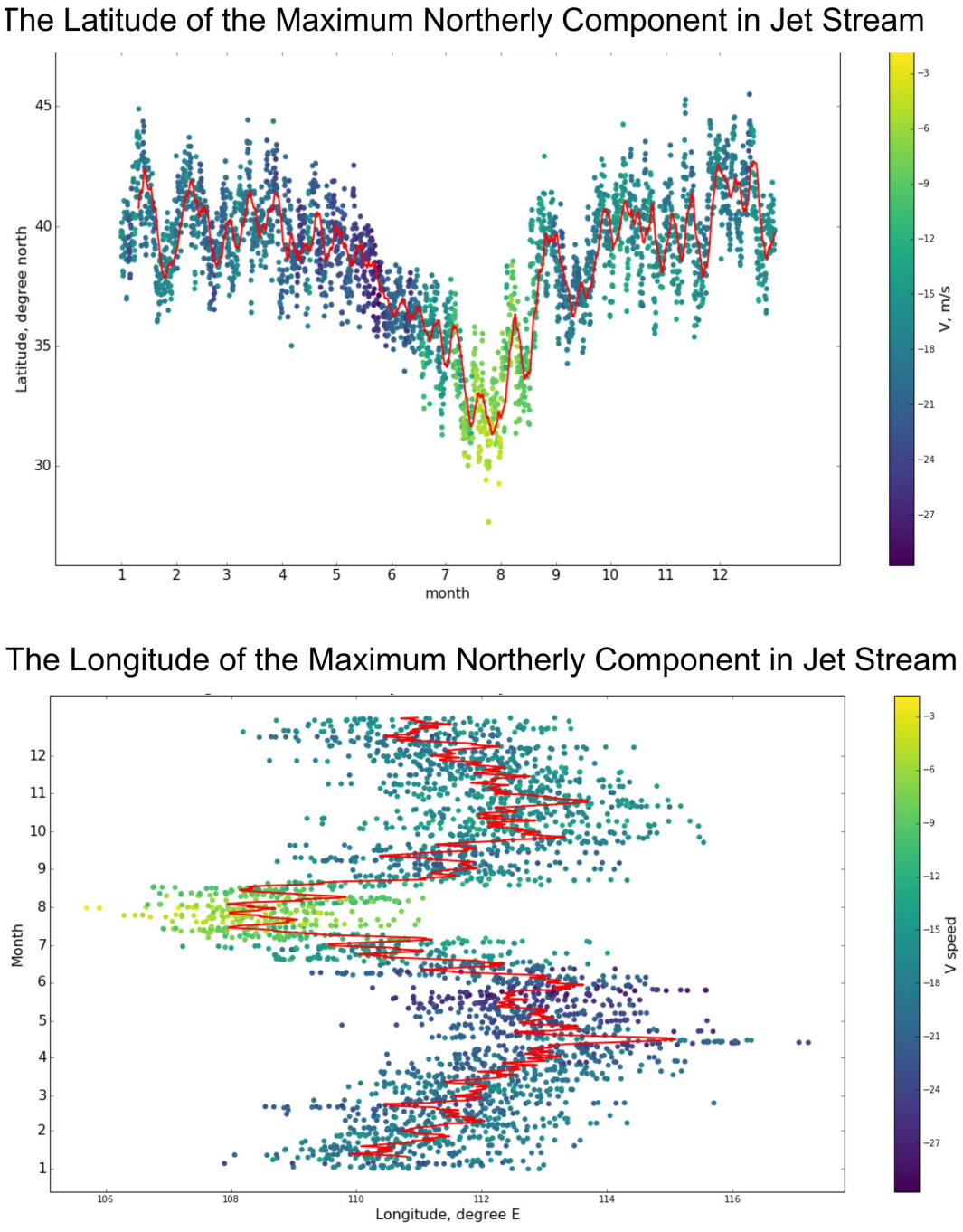


Figure 4.15: The climatology of the latitudinal position(first panel) and the longitudinal position(second panel) and the speed(color) of the northerlies over Eastern China(1979-2018). The strongest northerly wind has a seasonal cycle in both the latitudinal and the longitudinal position: it is at its northmost and eastmost in April and southmost and westmost in August. The east-west movement(about 10 degrees) is smaller than that of the north-south movement(about 15 degrees).

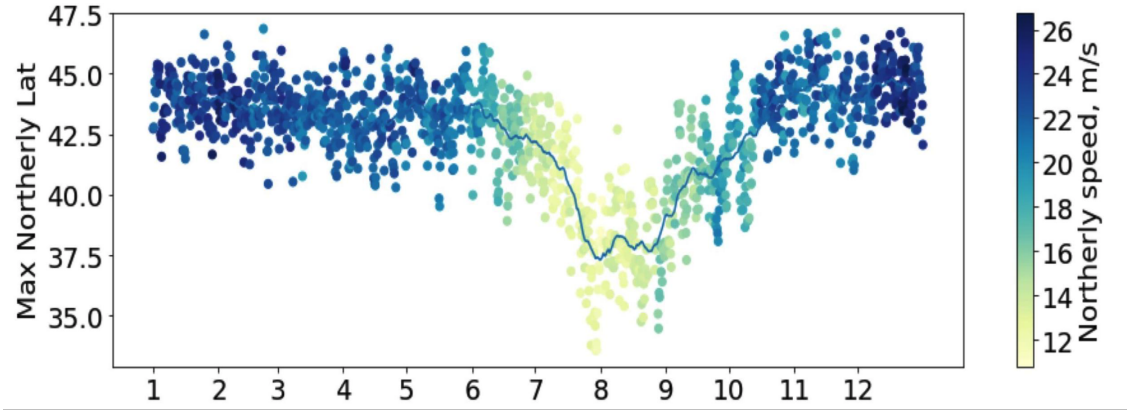


Figure 4.16: The climatology of the northerly wind on the 500-hPa surface: the latitude(y-axis) and the wind speed -V(color) of the maximum northerly. The maximum northerly wind is at 45°N and strong in winter until May, when it starts to move south and weakens. In August, the northerly is the weakest at 12 m/s and 35°N before it strengthens and moves north again.

Bibliography

Barrett, A. I., Gray, S. L., Kirshbaum, D. J., Roberts, N. M., Schultz, D. M., & Fairman Jr, J. G. (2015). Synoptic versus orographic control on stationary convective banding. *Quarterly Journal of the Royal Meteorological Society*, *141*(689), 1101–1113.

Bolin, B. (1950). On the influence of the earth's orography on the general character of the westerlies. *Tellus*, *2*(3), 184–195.

Bordoni, S., & Schneider, T. (2008). Monsoons as eddy-mediated regime transitions of the tropical overturning circulation. *Nature Geoscience*, *1*(8), 515–519.

Brikas, D., Karacostas, T., Pennas, P., & Flocas, A. (2006). The role of the subtropical jet stream during heat wave events over north-central greece. *Meteorology and Atmospheric Physics*, *94*(1-4), 219–233.

Byna, S., Wehner, M. F., & Wu, K. J. (2011). Detecting atmospheric rivers in large climate datasets, In *Proceedings of the 2nd international workshop on petascal data analytics: Challenges and opportunities*.

Cai, R., Tan, H., & Kontoyiannis, H. (2017). Robust surface warming in offshore china seas and its relationship to the east asian monsoon wind field and ocean forcing on interdecadal time scales. *Journal of Climate*, *30*(22), 8987–9005.

Chang, E. K. (2009). Diabatic and orographic forcing of northern winter stationary waves and storm tracks. *Journal of climate*, *22*(3), 670–688.

Charney, J. G., & Eliassen, A. (1949). A numerical method for predicting the perturbations of the middle latitudehttps://www.overleaf.com/project/5e648ccb09e westerlies. *Tellus*, *1*(2), 38–54.

Chen, B., Yang, J., & Pu, J. (2013). Statistical characteristics of raindrop size distribution in the meiyu season observed in eastern china. *Journal of the Meteorological Society of Japan. Ser. II*, *91*(2), 215–227.

Chen, G. T.-J. (2004). Research on the phenomena of meiyu during the past quarter century: An overview, In *East asian monsoon*. World Scientific.

Chen, J., & Bordoni, S. (2014). Orographic effects of the tibetan plateau on the east asian summer monsoon: An energetic perspective. *Journal of climate*, *27*(8), 3052–3072.

Chen, X., & Li, D. (2016). The features of meiyu under the new standard. *J. Meteorol. Sci*, *36*, 165–175.

Chiang, J. C., Fischer, J., Kong, W., & Herman, M. J. (2019). Intensification of the pre-meiyu rainband in the late 21st century. *Geophysical Research Letters*, *46*(13), 7536–7545.

Chiang, J. C., Fung, I. Y., Wu, C.-H., Cai, Y., Edman, J. P., Liu, Y., Day, J. A., Bhattacharya, T., Mondal, Y., & Labrousse, C. A. (2015a). Role of seasonal transitions and westerly jets in east asian paleoclimate. *Quaternary Science Reviews*, *108*, 111–129.

Chiang, J. C., Fung, I. Y., Wu, C.-H., Cai, Y., Edman, J. P., Liu, Y., Day, J. A., Bhattacharya, T., Mondal, Y., & Labrousse, C. A. (2015b). Role of seasonal transitions and westerly jets in east asian paleoclimate. *Quaternary Science Reviews*, *108*, 111–129.

Day, J. A., Fung, I., & Liu, W. (2018). Changing character of rainfall in eastern china, 1951–2007. *Proceedings of the National Academy of Sciences*, *115*(9), 2016–2021.

Day, J. A., Fung, I., & Risi, C. (2015). Coupling of south and east asian monsoon precipitation in july–august. *Journal of Climate*, *28*(11), 4330–4356.

Dee, D. P., Uppala, S. M., Simmons, A., Berrisford, P., Poli, P., Kobayashi, S., Andrae, U., Balmaseda, M., Balsamo, G., Bauer, d. P., Et al. (2011). The era-interim reanalysis: Configuration and performance of the data assimilation system. *Quarterly Journal of the royal meteorological society*, *137*(656), 553–597.

Ding, Y. (1992). Summer monsoon rainfalls in china. *Journal of the Meteorological Society of Japan. Ser. II*, *70*(1B), 373–396.

Ding, Y., & Chan, J. C. (2005). The east asian summer monsoon: An overview. *Meteorology and Atmospheric Physics*, *89*(1-4), 117–142.

Fairman Jr, J. G., Schultz, D. M., Kirshbaum, D. J., Gray, S. L., & Barrett, A. I. (2016). Climatology of banded precipitation over the contiguous united states. *Monthly Weather Review*, *144*(12), 4553–4568.

Fairman, J. G., Schultz, D. M., Kirshbaum, D. J., Gray, S. L., & Barrett, A. I. (2016). Climatology of banded precipitation over the contiguous united states. *Monthly Weather Review*, *144*, 4553–4568.

Ge, Q., Guo, X., Zheng, J., & Hao, Z. (2008). Meiyu in the middle and lower reaches of the yangtze river since 1736. *Chinese Science Bulletin*, *53*(1), 107–114.

Hagen, M. (1992). On the appearance of a cold front with a narrow rainband in the vicinity of the alps. *Meteorology and Atmospheric Physics*, *48*(1-4), 231–248.

He, L., Chao, Y., Suzuki, K., & Wu, K. (2009). Fast connected-component labeling. *Pattern recognition*, *42*(9), 1977–1987.

Held, I. M., Ting, M., & Wang, H. (2002). Northern winter stationary waves: Theory and modeling. *Journal of climate*, *15*(16), 2125–2144.

Hobbs, P. V. (1987). The gulf stream rainband. *Geophysical research letters*, *14*(11), 1142–1145.

Holton, J., & Hakim, G. (2013). *An introduction to dynamic meteorology. waltham, ma*. Academic Press.

Houze, R. A., Hobbs, P. V., Biswas, K. R., & Davis, W. M. (1976). Mesoscale rainbands in extratropical cyclones. *Monthly Weather Review*, *104*(7), 868–878.

Kang, S. M., & Polvani, L. M. (2011). The interannual relationship between the latitude of the eddy-driven jet and the edge of the hadley cell. *Journal of Climate*, *24*(2), 563–568.

Koch, P., Wernli, H., & Davies, H. C. (2006). An event-based jet-stream climatology and typology. *International Journal of Climatology: A Journal of the Royal Meteorological Society*, *26*(3), 283–301.

Kong, W., & Chiang, J. C. (2020). Interaction of the westerlies with the tibetan plateau in determining the mei-yu termination. *Journal of Climate*, *33*(1), 339–363.

Krishnan, R., & Sugi, M. (2001). Baiu rainfall variability and associated monsoon teleconnections. *Journal of the Meteorological Society of Japan. Ser. II*, *79*(3), 851–860.

Lau, K., Kim, M., & Kim, K. (2006). Asian summer monsoon anomalies induced by aerosol direct forcing: The role of the tibetan plateau. *Climate dynamics*, *26*(7-8), 855–864.

Lee, S., & Kim, H.-k. (2003). The dynamical relationship between subtropical and eddy-driven jets. *Journal of the atmospheric sciences*, *60*(12), 1490–1503.

Li, X., & Ting, M. (2017). Understanding the asian summer monsoon response to greenhouse warming: The relative roles of direct radiative forcing and sea surface temperature change. *Climate Dynamics*, *49*(7-8), 2863–2880.

Liang, P., & He, J. (2008). Review for climate change of meiyu over the yangtze-huaihe basins. *Plateau Meteorol*, *27*, 1–15.

Liang, X.-Z., & Wang, W.-C. (1998). Associations between china monsoon rainfall and tropospheric jets. *Quarterly Journal of the Royal Meteorological Society*, *124*(552), 2597–2623.

Molnar, P., Boos, W. R., & Battisti, D. S. (2010). Orographic controls on climate and paleoclimate of asia: Thermal and mechanical roles for the tibetan plateau. *Annual Review of Earth and Planetary Sciences*, *38*.

Namias, J. (1950). The index cycle and its role in the general circulation. *Journal of Meteorology*, *7*(2), 130–139.

Namias, J., & Clapp, P. F. (1949). Confluence theory of the high tropospheric jet stream. *Journal of Meteorology*, *6*(5), 330–336.

Ninomiya, K. (2009). Characteristics of precipitation in the meiyu-baiu season in the cmip3 20th century climate simulations. *Journal of the Meteorological Society of Japan. Ser. II*, *87*(4), 829–843.

Niziol, T. A., Snyder, W. R., & Waldstreicher, J. S. (1995). Winter weather forecasting throughout the eastern united states. part iv: Lake effect snow. *Weather and Forecasting*, *10*(1), 61–77.

Peixoto, J. P., & Oort, A. H. (1992). *Physics of climate*. New York, NY (United States); American Institute of Physics.

Rikus, L. (2018). A simple climatology of westerly jet streams in global reanalysis datasets part 1: Mid-latitude upper tropospheric jets. *Climate dynamics*, *50*(7-8), 2285–2310.

Roe, G. H. (2005). Orographic precipitation. *Annu. Rev. Earth Planet. Sci.*, *33*, 645–671.

Röthlisberger, M., Pfahl, S., & Martius, O. (2016). Regional-scale jet waviness modulates the occurrence of midlatitude weather extremes. *Geophysical Research Letters*, *43*(20), 10–989.

Sampe, T., & Xie, S.-P. (2010). Large-scale dynamics of the meiyu-baiu rainband: Environmental forcing by the westerly jet. *Journal of Climate*, *23*(1), 113–134.

Schiemann, R., Lüthi, D., & Schär, C. (2009). Seasonality and interannual variability of the westerly jet in the tibetan plateau region. *Journal of Climate*, *22*(11), 2940–2957.

Tao, S.-Y. (1987). A review of recent research on the east asian summer monsoon in china. *Monsoon meteorology*, 60–92.

Vallis, G. K. (2017). *Atmospheric and oceanic fluid dynamics*. Cambridge University Press.

Wang, B. (2002). Rainy season of the asian–pacific summer monsoon. *Journal of Climate*, *15*(4), 386–398.

Wang, B., & Li, T. (2004). East asian monsoon-enso interactions, In *East asian monsoon*. World Scientific.

Wang, W., Zhou, W., Li, X., Wang, X., & Wang, D. (2016). Synoptic-scale characteristics and atmospheric controls of summer heat waves in china. *Climate dynamics*, *46*(9-10), 2923–2941.

White, R., Battisti, D., & Roe, G. (2017). Mongolian mountains matter most: Impacts of the latitude and height of asian orography on pacific wintertime atmospheric circulation. *Journal of Climate*, *30*(11), 4065–4082.

Woollings, T., Hannachi, A., & Hoskins, B. (2010). Variability of the north atlantic eddy-driven jet stream. *Quarterly Journal of the Royal Meteorological Society*, *136*(649), 856–868.

Xu, H., He, J., & Zhou, B. (2001). The features of atmospheric circulation during meiyu onset and possible mechanisms for westward extension (northward shift) of pacific subtropical high. *Quart. J. Appl. Meteor*, *12*, 150–158.

Yeh, D., Tao, S., & Li, M. (1959). The abrupt change of circulation over the northern hemisphere during june and october. *The Atmosphere and the Sea in Motion*, 249–267.

Yoshizaki, M., Kato, T., Tanaka, Y., Takayama, H., Shoji, Y., Seko, H., Arao, K., Manabe, K., Et al. (2000). Analytical and numerical study of the

26 june 1998 orographic rainband observed in western kyushu, japan. *Journal of the Meteorological Society of Japan. Ser. II*, *78*(6), 835–856.

Zhou, Y., Gao, S., & Shen, S. S. (2004). A diagnostic study of formation and structures of the meiyu front system over east asia. *Journal of the Meteorological Society of Japan. Ser. II*, *82*(6), 1565–1576.

Zhu, X., Wu, Z., & He, J. (2008). Anomalous meiyu onset averaged over the yangtze river valley. *Theoretical and applied climatology*, *94*(1-2), 81–95.